Universitat Politècnica de Catalunya

Temporal Correlations and Dynamical Transitions in Semiconductor Lasers with Optical Feedback.

A thesis submitted by

Carlos Alberto Quintero Quiroz

in fulfillment of the requirements for the degree of
Doctor in Computational and Applied Physics

Supervisors: Cristina Masoller
Maria Carme Torrent

Departament de Física
Terrassa, 2017

Abstract

Optical excitable systems that mimic neuronal behavior have potential to be building-blocks of novel, ultra-fast, neuron-inspired photonic information processing systems. In particular, semiconductor lasers with optical feedback (SLOF), can emit optical spikes with temporal correlations resembling those present in neuronal spike. SLOF can also generate a rich variety of dynamical behaviors, and thus, are ideal testbeds for studying dynamical transitions and testing novel analysis tools. In order to advance in the development of neuron-inspired laser processors it is important to understand how SLOF represent (or encode), in the sequence of spikes, an external input. It is also important to understand how the different dynamic regimes develop, and how they are affected by external perturbations.

Hence, the aim of this Thesis is the study of temporal correlations and dynamical transitions in the dynamics of an SLOF. To do this, we perform experiments, model simulations, and use a symbolic method to analyze the obtained intensity time-series.

First, we investigate how the spiking laser output encodes a weak periodic input that is implemented via direct modulation of the laser pump current. Experimental sequences of optical spikes were recorded and analyzed by using the ordinal symbolic methodology that identifies and characterizes serial correlations in data sets. When changing the frequency and amplitude of the modulation, transitions among different locking regimes are detected in the form of changes in the statistics of the ordinal patterns. A good qualitative agreement is also found with simulations of the Lang and Kobayashi model.

Second, we identify the onset of different dynamical regimes that occur as the laser pump current increases. We apply three analysis tools that allow quantifying various aspects of the dynamical regime transitions. The first method is based on the analysis of the standard deviation of the intensity time-series, recorded with different oscilloscope sampling rates. The second method relies on the analysis of the number of spikes as a function of the threshold used to define the spikes. The third method is based on the ordinal analysis of the inter-spike-intervals. These tools allow us to quantitatively detect the onset of two different dynamical regimes, know as low-frequency fluctuations (LFF), and coherence collapse (CC).

We also analyze the transition from a noise-dominated regime to a more deterministic (less stochastic) dynamics. For this study, in addition to the experimental laser system (an SLOF), we used as numerical examples the logistic map and the Rössler chaotic system. We find that, when the noise is strong, the permuta-

tion entropy (computed from the probabilities of the ordinal patterns) increases faster than linearly. By comparing the results of these three systems, we discuss the possibility of determining, from time series analysis, whether the underlying dynamics is dominated by noise or by deterministic processes.

The results reported in this Thesis are relevant in a number of ways. The methodologies developed allow detecting parameter regions of noisy locking to an external weak periodic input and may be useful to investigate other forced excitable systems. In addition, the methods developed to detect the onset of different regimes can be valuable for analyzing regime transitions in many real world systems. Finally, the methodology for determining, for observed data, whether the underlying dynamic is mainly driven by noise or by deterministic effects can also be used in multidisciplinary applications (finances, geosciences, social systems, etc.).

Resumen

Los sistemas ópticos excitables capaces de imitar el comportamiento neuronal, pueden contribuir al desarrollo de nuevos sistemas fotónicos de procesamiento de información ultra-rápidos, inspirados en el procesamiento neuronal de información. En particular, los láseres semiconductores con retroalimentación óptica (LCRO), pueden emitir pulsos ópticos con correlaciones temporales similares a las que presentan las series disparos neuronales. Un LCRO puede generar una gran variedad de comportamientos dinámicos, por lo tanto, es ideal para estudiar transiciones dinámicas y probar nuevas herramientas de análisis de datos. Para avanzar en el desarrollo de procesadores basados en láseres de semiconductor que emulen neuronas, es importante entender como estos láseres codifican un estimulo externo en la secuencia de pulsos de intensidad emitidos; como se desarrollan los diferentes regímenes dinámicos y como se ven afectados por perturbaciones externas.

El objetivo de esta Tesis es el estudio de las correlaciones temporales y de las transiciones dinámicas en un LCRO. Para ello se ha realizado experimentos y simulaciones, y se han analizado los datos obtenidos empleando una técnica de analisis simbólico.

En primer lugar, investigamos como los pulsos emitidos por el láser codifican una señal de entrada periódica débil, suministrada a través de modulación directa de la corriente de inyección del láser.

Se han registrado secuencia experimentales de pulsos opticos y se han analizado usando el analisis simbólico ordinal. Dicho método, las identifica y caracteriza a través de de un conjunto de datos. Las variaciones en frencuencia y amplitud de modulación de la señal introducida producen transiciones entre diferentes regímenes del láser, que se detectan mediante cambios en la estadística del análisis simbólico. Los resultados obtenidos de las simulaciones usando el modelo de Lang-Kobayashi, concuerdan cualitativamente con las observaciones experimentales.

En segundo lugar, hemos aplicado tres herramientas de análisis que permiten cuantificar diversos aspectos de las transiciones de régimen dinámico. De tal modo, hemos identificado el inicio de diferentes regímenes que se producen al aumentar la corriente de inyección del láser. El primer método se basa en el análisis de la desviación estándar de las series temporales de la intensidad, registradas con diferentes frecuencias de muestreo del osciloscopio; el segundo método, se basa en el análisis del número de pulsos que cruzan un determinado un umbral, en función del umbral utilizado. El tercer método, consiste en el análisis ordinal de los

distintos intervalos temporales entre pulsos. Estas herramientas detectan cuantitativamente el inicio de dos regímenes dinámicos, conocidos como fluctuaciones de baja frecuencia (LFF) y colapso de coherencia (CC).

También hemos analizado la transición de un régimen dominado por ruido hacia una dinámica más determinista. Para este estudio, además del sistema experimental (un LCRO), hemos utilizado como ejemplos numéricos el mapa logístico y el sistema de Rössler. Encontramos que, cuando el nivel de ruido es alto, la entropía de permutación (calculada a partir de las probabilidades de patrones ordinales) aumenta mas rápido que linealmente y discutimos la posibilidad de determinar, a partir del análisis de series temporales, si la dinámica subyacente está dominada por ruido o por un proceso determinísta.

Los resultados presentados en esta Tesis son relevantes en varios aspectos. Las metodologías desarrolladas, pueden ser útiles para investigar otros sistemas excitables porque permiten detectar regiones de "loking" producidos por una perturbación externa periódica y débil. Además, los métodos desarrollados, pueden detectar cualitativamente el inicio de diferentes regímenes dinámicos y pueden ser valiosos para analizar transiciones entre regímenes en otros sistemas. Por último, la metodología propuesta para determinar en los datos observados, si la dinámica subyacente es principalmente dominada por el ruido o por efectos deterministas, puede también tener aplicaciones multidisiplinarias.

Agradecimientos

Esta tesis no la habría podido realizar sin la colaboración de muchas personas que me brindaron su ayuda. Siempre resulta difícil agradecer a todos aquellos que de una u otra manera me han acompañado a lo largo de este viaje, porque bien nunca alcanza el tiempo, o la memoria para nombrar o dar con justicia todos los créditos y méritos a quienes se los merecen. Por tanto, quiero agradecerles a todos ellos lo que han hecho por mí, para que este trabajo saliera adelante de la mejor manera posible.

Debo agradecer de manera sincera a la Dra. Cristina Masoller y la Dra. Maria del Carmen Torrent, por aceptarme para realizar este trabajo bajo su dirección. Su apoyo y confianza en mi trabajo y su capacidad para guiar mis ideas han sido un aporte invaluable, no solamente en el desarrollo de esta tesis, sino también en mi formación como investigador. Las ideas propias, siempre enmarcadas en su orientación y rigurosidad, han sido la clave del buen trabajo que hemos realizado juntos.

A mi esposa María, que durante estos años de carrera ha sabido apoyarme para continuar y nunca renunciar; gracias por su amor incondicional y por su ayuda en esta tesis.

Le doy gracias a mis padres, Marco y Esthela, por apoyarme en todo momento, por los valores que me han inculcado, y por haberme dado la oportunidad de tener una excelente educación en el transcurso de mi vida. Sobre todo, por ser un excelente ejemplo de vida a seguir. A mis hermanos, Marco y Gabriela por estar a mi lado, siempre ayudándome a afrontar los retos que se me han presentado a lo largo de la vida.

A mis compañeros del Grupo de Dinámica Nolineal, Optica Nolineal y Lasers; Shubham, Andrés, Lina, Dani, Maciek, Taciano, John, Bingxia, Yu Chieh, Auro, Sandro, Houssam, Lara, Jose María, Jordi, Dario, Waqas, Simone, Giulio, Ignacio, Pablo, María y Donatus quienes, más que compañeros, son grandes amigos. A los profesores Ramón Vilaseca, Kestas Staliunas, José Trull, Ramon Herrero, Toni Pons, Crina Cojocaru, Muriel Botey, Josep Lluís Font y Carles Serrat a quienes le agradezco infinitamente su ayuda. También muchas gracias a Montse Gea, Jaume y Cristina Fernández por su paciencia y ayuda.

Son muchas más las personas que han formado parte de mi vida profesional a las que me encantaría agradecerles su amistad, consejos, apoyo, ánimo y compañía en los momentos más difíciles de mi vida. Algunas están aquí conmigo y otras en mis recuerdos y en mi corazón. Sin importar en donde estén, quiero darles a todos las gracias.

Contents

Part I

Introduction

Dynamics of semiconductor lasers.

CHAPTER 1

Lasers (Light Amplification by Stimulated Emission of Radiation) were initially comfortably placed in the realms of science fiction; however, nowadays their applications are present in all aspects of daily life from telecommunications to biomedicine. In this Chapter we first describe general features of semiconductor lasers and then focus in the dynamics of SLOF. We describe the low-frequency fluctuations (LFF) and coherence colapse (CC) regimes that will be further investigated in Chapters 3 and 4. The Lang and Kobayashi model (LK model) is also presented.

1.1 Historical Background.

The theories developed for understanding the quantum nature of radiation and matter, in the first half of the twentieth century, established the basis to describe the interaction between them. For instance, in 1900 Max Planck deduced the relationship between energy and frequency of the radiation [1]. His ideas marked a turning point in physics and motivated the work of forthcoming physicists such as Albert Einstein, who published in 1905 his work on the photoelectric effect [2]. In a latter work (1917), Einstein suggested the process that makes a laser possible, called stimulated emission [3]. He predicted that, besides absorbing and emitting light spontaneously, electrons could be stimulated to emit light at a particular wavelength. However, it would take nearly 40 years, before scientists were able to demonstrate Einstein's prediction, leading lasers to become the powerful and omnipresent tools they are today.

Theodore H. Maiman, a researcher at Hughes Research Laboratories in Malibu, California, built the first ruby laser [4, 5] using a Fabry-Perot resonator and photographic flashbulbs as the laser's pump source. Since then, a huge variety of different types of lasers followed [6, 7].

Particularly in the year 1962, three groups from General Electric Company (GE), International Business Machines Corp. (IBM) and Lincoln Laboratory in the Massachusetts Institute of Technology (MIT), simultaneously developed a Gallium-Arsenide (GaAs) laser, a semiconductor device that converts electrical energy directly into infrared light [8–10]. In the same year Nick Holonyak Jr., a scientist from the laboratory GE in Syracuse, New York, published his work using Gallium-Arsenide-Phosphide (GaAsP) developing the laser diode in "visible red" light [11]. A compact and efficient source of coherent light, today semiconductor lasers (also known as laser diodes) are used not only for optical communications,

but also, in a wide range of consumer products (CD players, laser printers, scanners, etc.; semiconductor lasers can also be fabricated in arrays (1D and 2D) that generate large output powers).

1.2 Physics of lasers.

The simplest description of a laser is a device that takes electromagnetic radiation (light) and amplifies it. The source of this radiation are particles in an "active" medium (for example atoms when their electrons jump through their possible energy levels). Typically, electrons are at the ground level, and if we inject just the right amount of energy, this can displace an electron to a higher energy level. This phenomenon is called *absorption*, and in this new state, the atom is excited, although this excited state is unstable. Then, the atom returns to the ground state by emitting the absorbed energy as a photon. This process of radiation is known as *spontaneous emission*: the atom generates light (emitting radiation) spontaneously.

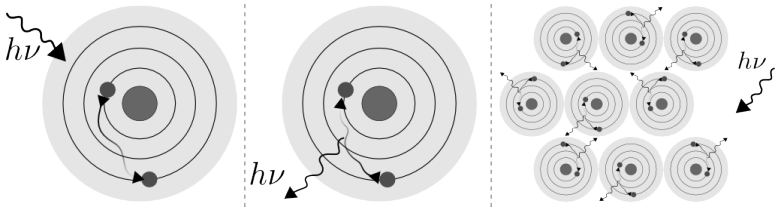

Figure 1.1: Schematic representation of the laser's operation principles. (Left) Absorption: inject energy into an atom and it can shift an electron from its ground state to an excited state. (Middle) Spontaneous emission: an excited electron will drop back to the ground state, emitting a photon. (Right) Stimulated emission: a photon triggers the emission of identical photons.

However, the atoms do not usually emit spontaneously, since typically they have more electrons in their ground states that in the excited states. If we want to keep the production of photons, we have to pump energy to the atoms to hold the electrons in their excited states. In this way, the "population" of excited electrons is greater than the "population" of electrons in the ground state and this situation is known as *population inversion*. In this situation, a photon with the right amount of energy ($\Delta E = h\nu$)[1], will make one of the excited electrons return to the ground state by emitting an identical photon. This process is called *stimulated emission*. Now these two photons can excite other atoms to emit more photons, and coherent[2] light is generated. A schematic representation of these three process is shown in Fig. 1.1. If the material is placed in a cavity with mirrors, the photons will go back and forth inside the cavity, amplifying the process. Then, making one of the mirrors slightly transparent, a beam of laser light is obtained.

Since there are many different types of atoms that can be excited in a variety of ways, many different types of lasers can be developed [7, 12]. Currently, the most common types of lasers which use different types of active medium are solid state, gas, fiber, and semiconductors lasers [13].

[1] Where h is Planck's constant and ν the photon's frequency.

[2] This means the same features for all photons, i.e. the wavelength, phase, polarization, and propagation direction.

1.2.1 Physics of semiconductor lasers.

The simplest semiconductor laser consists of a p-n junction device known as homo-junction, which essentially is a semiconductor wafer made from slices of a material with different doping, as the one shown in Fig. 1.2. In the p-region, the doping takes away electrons from the material and leaves behind "holes" where electrons should be, and in the n-region the doping adds some extra electrons.

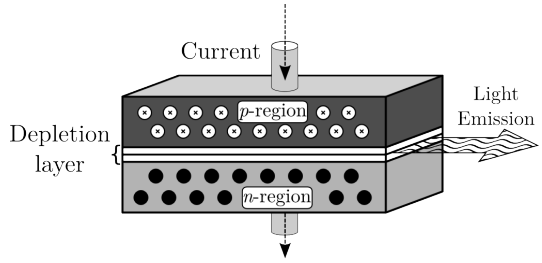

Figure 1.2: Schematic representation of the simplest semiconductor laser, a p-n junction.

In a small region near of the junction, some of the additional electrons in the n-region will go through the junction and recombine with the holes in the p-region. This region becomes a barrier between n-region and p-region and is called *depletion layer*.

By applying an external voltage, the p-n junction allows the flow of the electrical current in one direction (known as forward-biased operation). Under this operation mode, the electrons and the holes recombine and release energy in the form of photons. In a semiconductor laser, these photons interact with the incoming flux of electrons, producing more photons as it occurs in other types of lasers. The first generation of semiconductor lasers were homo-junctions. Nowadays, semiconductor lasers are fabricated with more advanced techniques that allows for a much better confinement of electrons, holes, and photons (using, for example, multiple quantum wells formed by different types of semiconductor materials as the active region), known as hetero-junctions.

The type of laser presented in Fig. 1.2 is also known as an edge-emitting laser (EEL) because light propagates in a direction along the junction. For semiconductor lasers, there are three main types of cavities: the Fabry-Pérot (FP) resonant cavity consists of two cleaved end facets; the distributed Bragg reflector (DBR) with Bragg reflectors[3] as end mirrors; and the distributed feedback (DFB) with a periodic structure in the active region. The cavity defines the modes ("frequencies") that the laser can emit. Lasers with FP cavity typically emit multiple longitudinal modes within the gain bandwidth with a mode spacing determined by the cavity length and, certain modes, within the gain bandwidth of the active medium, are more enhanced than others. The DFB and DBR can emit in a single mode with a frequency directly related to the periodicity of the structure. Figure 1.3 shows a representation of how the output modes are selected in an EEL. The black line in Fig. 1.3 displays the modes of the cavity, a set of this modes are selected by the optical gain (red curve) and then, by using the Bragg reflectivity (green curve), a

[3] It is a structure formed by multiple layers of alternating materials with varying refractive index, or by periodic variation of some characteristic (such as thickness) of a dielectric waveguide [12].

single mode can be selected.

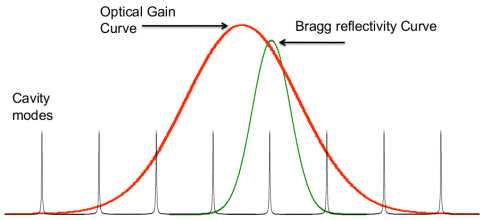

Figure 1.3: Representation of how the output modes are selected in an edge-emitting laser. Adapted from [14].

Another type of semiconductor laser is known as vertical cavity surface-emitting laser (VCSEL, but these lasers are not studied in this Thesis). The main difference between VCSELs and EELs is that in VCSELs the light propagates in the direction perpendicular to the active region.

1.3 Emission characteristics of semiconductor lasers.

This Section describes some important characteristics of the semiconductor lasers, such as: the dependence of the emitted light with the pump current, the relaxation oscillation, and the optical spectrum.

1.3.1 Light-current dependence.

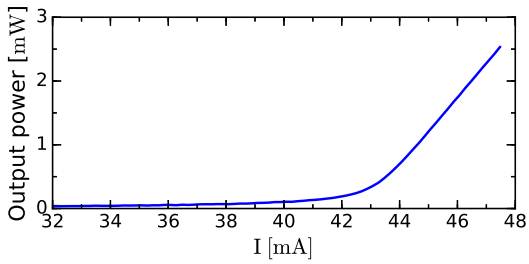

Figure 1.4: Output power as a function of the pump current (I [mA]). The laser used is a 658 nm AlGaInP semiconductor laser (Hitachi HL6501MG). For currents below the threshold current (I_{Th}), spontaneous emission dominate the output power, for currents higher than the threshold, the stimulated emission dominates, and the laser starts to lase. Above the threshold, the output power grows linearly with the injected current (for very high currents the behavior is nonlinear, not shown).

As it was explained in the previous Section, a semiconductor laser converts electrical energy into optical output. Therefore it is crucial to characterize the amount of light that is emitted by a semiconductor laser at a given injected current. This characterization usually is represented by the curve of the output power of the laser vs. the pump current (also called as light vs. current characteristic, or L-I curve). This curve is also employed to determine the efficiency of the laser as well as the threshold current (current at which starts lasing). An L-I curve for a 658 nm AlGaInP semiconductor laser (Hitachi HL6501MG) at 18.5ºC is shown in Fig. 1.4. Here, when the pump current is increased, in the beginning, the laser shows spontaneous emission and the output power grows very slowly (in the Figure it appears almost like a flat line). At a certain value of the pump current (i.e., I_{Th}), the laser starts to emit stimulated light, and the output power increases linearly

with the pump current.

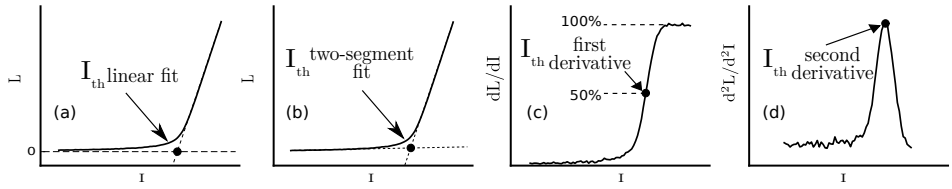

Figure 1.5: Different methods to define the threshold current: (a) the linear fit, (b) the two-segment fit, (c) the first derivative technique, and (d) the second-derivative technique.

There are various ways to define the threshold current which are presented in Fig. 1.5. The linear fit method (Fig. 1.5a) uses a linear fit of the high current portion of the L-I curve and defines the threshold as the point where the linear fit intercepts the X-axis corresponding to the zero optical power. The two-segment fit method (Fig. 1.5b) uses two linear fits (the low and the high portions of the L-I curve) and defines the threshold as the point where they intersect. In the first derivative method, the value of the threshold is defined as the one-half the maximum of the rising edge of the dL/dI curve (Fig. 1.5c). Finally, in the second derivative method (Fig. 1.5d), the threshold is the point at which the d^2L/d^2I curve has a maximum. Any of the four methods described can be used, and the first derivative method is the one employed in this Thesis.

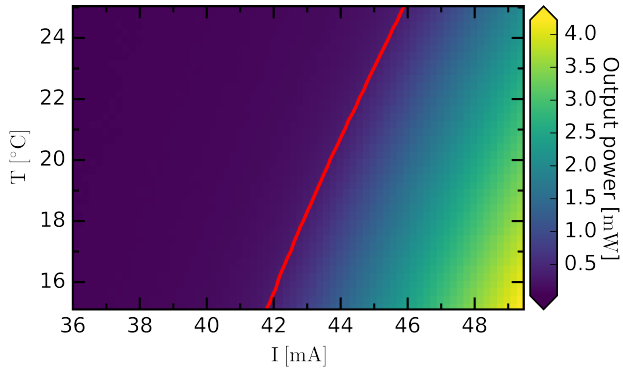

Figure 1.6: Variation of the threshold current for different operating temperatures in an AlGaInP Fabry-Perot semiconductor laser (Hitachi HL6501MG). The solid red line indicates the threshold current for distinct values of the temperature.

In semiconductor lasers the light emission does not only depends on the pump current but also on the temperature. As the temperature increases the laser's gain spectrum moves, and also, changes in temperature affect the refractive index of the active medium that produces a shift in the cavity modes. Due to theses two effects, more current is required before the laser starts to lase [12]. In Fig. 1.6 a color-code representation of the L-I curve for different values of the temperature is shown. The solid red line shows how the threshold current varies with the temperature.

1.3.2 Relaxation Oscillations.

In semiconductor lasers, transient oscillations known as relaxation oscillations occur during the turn-on due to the nonlinear coupling between photons and carriers (i.e., pairs of electrons and holes). A simple way to describe them is by con-

sidering a situation in which the pump current abruptly increases as in a step-like function. In this situation, the carrier density will grow rapidly and a pulse of light is emitted. Due to the light emission, the carrier population decreases rapidly, and in consequence the output power will drop till the carriers recover. This interplay produces the relaxation oscillations between the optical field and the carriers.

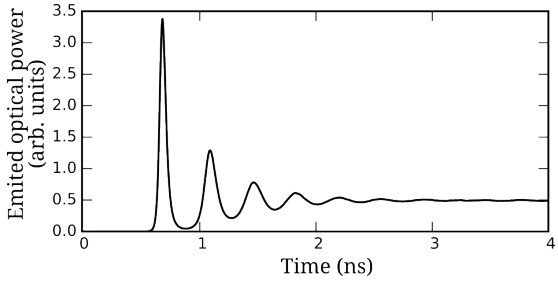

Figure 1.7: Emitted output power of a laser subject to a step-like pump current. Simulations of the rate equations presented in Section 1.4 with parameters: $\tau_p = 1.67$ ps, $\tau_N = 1$ ns, $\mu = 1.5$, $\beta_{sp} = 10^{-4}$.

In other words, relaxation oscillations occur in a semiconductor laser because carriers can not instantaneously follow the photons. The relaxation oscillation frequency takes values of the order of a few GHz, and depends on the pump current, and the life time of the photons, and of the the carriers [13]. Figure 1.7 presents the simulated output power of a laser, when is subject to a step-like pump injection. The model used to simulate the laser intensity is describe in Section 1.4.

1.3.3 Optical spectrum.

Edge-emitting lasers (EELs), which are the lasers studied in this Thesis are in general multimode, although depending on the cavity design, the pump current, and the temperature of operation, quasi-single mode emission can be obtained.

Figure 1.8 displays the optical spectrum of one of the lasers used in this Thesis. We show two spectra when the current is just above and when it is well above threshold. For low pump currents the emission is multimode (left panel), but as the pump current is increased, one mode dominates the emission. As it can be appreciated in the right panel (well above threshold) the emission is almost monomode.

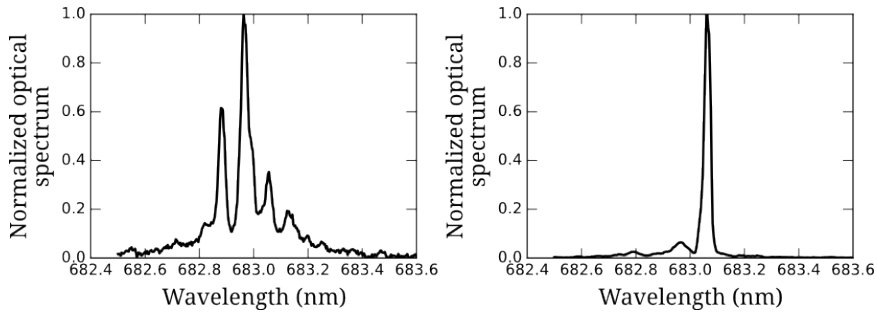

Figure 1.8: Optical spectrum for pump current just above (left) and well above (right) the threshold. The spectrum is normalized to the maximum value and the laser is a Hitachi HL6501MG.

1.4 Semiconductor laser model.

Lasers can be described by employing three physical variables: the polarization of the material, the carrier population, and the optical field. Haken [15] showed that lasers are nonlinear systems and can display chaotic behavior on their output power, because of the physical quantities mentioned above, correspond to three coupled nonlinear degrees of freedom. The relation between the relaxation times of the three variables is directly related to the possible dynamics presented by the laser [6].

Arecchi et al. [16] investigated the role of the relaxation times of the three variables and categorized lasers in three classes: A, B, and C. Class-A lasers can be characterized only by the optical field; Class-B lasers can be modeled by taking into account the optical field and the carrier population. Finally, Class-C lasers are described by the full set of variables, and consequently, they can exhibit chaotic behavior.

Semiconductor lasers are class-B lasers; they can be modeled by two coupled rate equations that described how the slowly varying complex field amplitude, E, and the carrier density, N evolve. The model equations (in adimensional form [13]) are:

$$\begin{aligned} \frac{dE}{dt} &= \frac{1}{2\tau_p}(1+\alpha)(G-1)E + \sqrt{2\beta_{sp}}\,\xi \\ \frac{dN}{dt} &= \frac{1}{\tau_N}\left(\mu - N - G|E|^2\right) \end{aligned} \tag{1.1}$$

where τ_p and τ_N are the photon and carrier lifetimes respectively. The optical gain is $G = N/(1+\varepsilon|E|^2)$ here ε is a phenomenological coefficient that controls the gain saturation, due to spatial inhomogeneities or thermal effects. μ is the normalized pump current parameter, where $\mu = 1$ is the lasing threshold. β_{sp} is the coefficient of spontaneous emissions and ξ is a white Gaussian noise that represents spontaneous emission. The linewidth enhancement factor, α [17], quantifies how the refractive index of the semiconductor material changes with the carrier density:

$$\alpha = \frac{\mathrm{d}n_r/\mathrm{dN}}{\mathrm{d}n_i/\mathrm{dN}} \tag{1.2}$$

where n_r and n_i are the real and the imaginary part of the refractive index. In conventional EELs, α has typical values of 3–5 and is a relevant parameter in the dynamics of the laser.

1.5 Optical feedback.

The optical feedback results from the reflection of the laser light, by a mirror in front of the output facet as schematically represented in Fig. 1.9 (i.e. a laser with an external cavity). The feedback configuration has three main parameters: the length of the external cavity L_{ext} (which give a feedback delay time $\tau = \frac{2L_{ext}}{c}$, where c is the speed of light), the feedback strength, and the phase of the feedback light.

Induced by the feedback, the laser presents a wide variety of dynamical behaviors [18]. An important consequence of optical feedback is the reduction of the

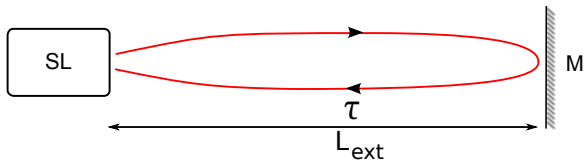

Figure 1.9: Sketch of the experimental setup of a semiconductor laser subjects to an optical feedback. L_{ext} is the length of the external laser cavity, τ is the time of flight of a photon around the external cavity, and M is the outside mirror.

threshold current of the laser. The threshold decreases because, when the light reenters the laser cavity and interacts coherently with the intra-cavity field, it reduces the cavity losses. The stronger the feedback, the larger the threshold reduction, as can be seen in Fig. 1.10. The feedback strength can be quantified through the reduction of the threshold current, as

$$\eta_{\%} = \frac{I_{Th} - I_{Th}^{f}}{I_{Th}} \tag{1.3}$$

where $\eta_{\%}$ is the percentage reduction, I_{Th} is the solitary laser threshold current and I_{Th}^{f} is the threshold current of the laser with optical feedback. The threshold reduction is a clear indicator of coherent feedback, if the feedback is incoherent (because, for example, $2L_{ext}$ es longer that the coherent length, or the polarization of the re-injected light is orthogonal to the intra-cavity field) the feedback does not produce any threshold reduction.

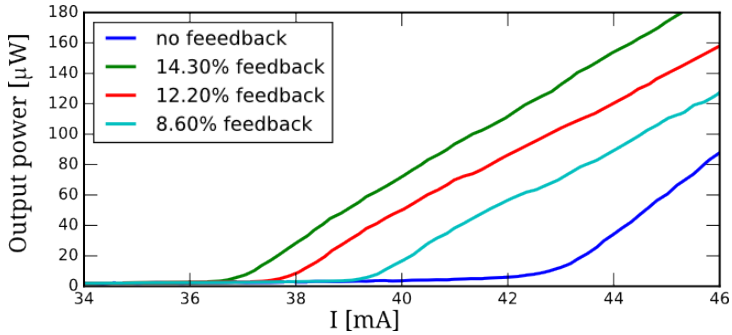

Figure 1.10: Experimental L-I curves displaying the effect of optical feedback in the lasing threshold of a semiconductor laser with different amounts of feedback for a Hitachi HL6501MG laser. The thresholds are estimated employing the method presented in Fig. 1.5c. The inset indicates the percentage of threshold reduction.

1.5.1 The Lang-Kobayashi model.

In 1980, Lang and Kobayashi proposed a model to describe the effects of weak to moderate optical feedback on single-mode diode lasers [19]. In the Lang-Kobayashi (LK) model, the light feedback to the semiconductor cavity is represented by a time delayed term added to the optical field rate equation (1.1):

$$\begin{aligned} \frac{dE}{dt} &= \frac{1}{2\tau_p}(1+\alpha)(G-1)E + \eta E(t-\tau)e^{-i\omega_0\tau} + \sqrt{2\beta_{sp}}\,\xi \\ \frac{dN}{dt} &= \frac{1}{\tau_N}\left(\mu - N - G|E|^2\right) \end{aligned} \tag{1.4}$$

where η is the feedback strength, τ is the feedback delay time, ω_0 is the solitary laser frequency, and $\omega_0\tau$ is the feedback phase. The numerical results presented in this Thesis (Chapters 3, 4 and 5) have been obtained with the model parameters, unless otherwise stated, listed in Table 1.1.

Parameter		Value
Photons lifetime	(τ_p)	1.67 ps
Carriers lifetime	(τ_N)	1 ns
Feedback delay time	(τ)	5 ns
Pump current	(μ)	1.01
Coefficient of spontaneous emissions	(β_{sp})	10^{-4}
Linewidth enhancement factor	(α)	4
Feedback strength	(η)	10 ns^{-1}
Coefficient of nonlinear gain	(ε)	10^{-3}

Table 1.1: Parameters used in the simulations, unless otherwise stated.

In order to study the laser dynamics under sinusoidal current modulation, the pump current parameter is varied as:

$$\mu = \mu_0 + A_{\text{mod}} \sin(2\pi f_{\text{mod}} t), \tag{1.5}$$

where μ_0 is the DC current, A_{mod} is the modulation amplitude and f_{mod} is the modulation frequency.

The steady state solutions of the LK model are related to constructive and destructive interferences between the intra-cavity field and the feedback field. The steady solutions are known as *external cavity modes* (ECMs) and we referred as *modes* for the constructive interference and *antimodes* for the destructive interference.

The LK model makes substantial simplifications:

- Assumes single mode emission, while feedback often induces multi-mode emission.
- Assumes low or moderate feedback intensity and thus neglects multiple round-trips of light in the external cavity.
- Neglects spatial and thermal effects.

Due to all these simplifications, only a qualitative accordance with empirical measurements could be expected, but surprisingly, the LK model describes different dynamics of a semiconductor laser. To name a few: low-frequency fluctuations (LFF), coherence collapse (CC) and coexistence of LFF and stable emission. These dynamical regimes are described in the following Subsection.

1.5.2 Dynamical regimes induced by optical feedback.

Semiconductor lasers with optical feedback (SLOF) have been the object of intense experimental and numerical investigation in the last three decades [20–58]. In this Thesis we study the dynamics induced by moderate amount of feedback (threshold reduction of the order of $5 \sim 15\%$). SLOFs are time-delay systems and (as we will discuss in Chapter 2) this type of systems are infinite dimensional, therefore they can show chaotic behavior. The chaotic output generated by SLOFs

has a wide range of applications (sensors, ultra-fast random number generation, information processing, etc) [59–67].

The diagram of Tkach and Chraplyvy [68] (Fig. 1.11) has been the reference for describing and classifying feedback effects in semiconductor laser. This diagram points out five types of regimes induced by optical feedback. These regimes rely on three factors: the feedback power ratio, the external cavity length, and the phase of the incoming power. Each regime determines how a semiconductor laser operates

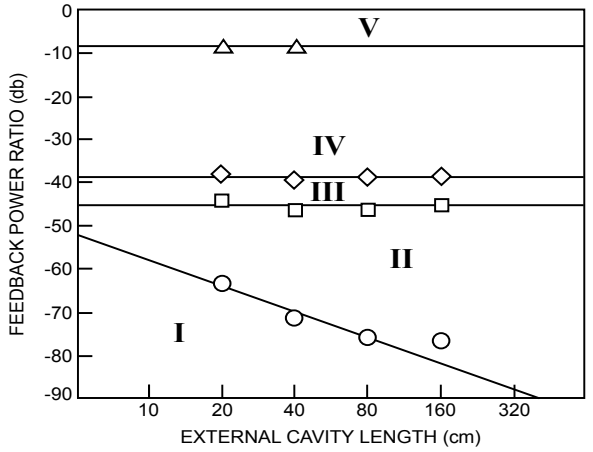

Figure 1.11: Regimes according to the description of Tkach and Chraplyvy for an SLOF varying the feedback strength, and the external cavity length. Adapted from [68].

under external optical feedback. **Regime I**: the laser linewidth is broadened or narrowed, depending on the distance to the feedback reflector, which determines the phase of the optical feedback. **Regime II**: mode hopping among external cavity modes. **Regime III**: stable single mode operation with linewidth reduction, in this regime the mode hopping is suppressed and the laser oscillates with a narrow linewidth. **Regime IV**: unstable operation with coherence collapse, the relaxation oscillations become undamped and the linewidth of the laser is highly broadened. **Regime V**: stable operation with significant linewidth reduction, the internal and external cavities turn into a composite cavity and the laser emits on a single mode with a narrow linewidth.

The operational conditions studied in this Thesis correspond to moderate feedback (regime IV), and long cavity[4]. With this operational conditions, the dynamical regimes of an SLOF as the pump current is increased are: noise stable emission, low-frequency fluctuations (LFFs) and coherence collapse (CC) [20, 69, 70]. The LFFs and CC regimes have been known for decades and their dynamical origin and statistical properties have been intensively studied. However, to the best of our knowledge, the transition points from noisy emission to LFFs, and from LFFs to CC, occurring as the pump current increases, have not yet been quantified.

Very close to the threshold the laser intensity display noisy fluctuations,as shown in the Fig. 1.12a. As the pump current increases the laser enters the LFF regime. A typical intensity time trace is shown in Fig. 1.12b. In this regime, the intensity exhibits abrupt dropouts that seems to occur at random times (the

[4]This case is when τ is much larger than the period of the relaxation oscillations, in our case $\tau \approx 5$ns

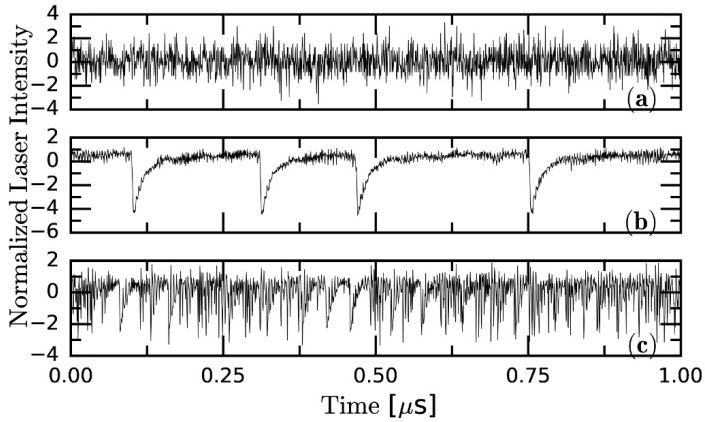

Figure 1.12: Typical intensity time-series, normalized to zero mean and unit variance: (a) noisy fluctuations, (b) dropouts in the LFF regime and (c) fast fluctuations in the CC regime. The laser pump current, normalized to the threshold current of the solitary laser, are I/I_{Th} = 0.95, 1.02 and 1.20, respectively. The horizontal axis is the same in the three panels. The intensities were detected with a 1 GHz digital oscilloscope (Agilent Infiniium DSO9104A). The properties of these regimes are discussed in Chapter 4.

time intervals are of the order of hundredths of nanoseconds between consecutive drops). The drops are in fact the envelope of much faster optical pulses (picoseconds) [71], hence this regime is known as low-frequency fluctuations (LFFs). Because, in the LFF regime, the inverted time-series resembles the spikes of a biological neurons, on this Thesis the intensity dropouts will also be referenced as *optical spikes*. As the pump current continues increasing the LFF dropouts gradually become more frequent and more irregular as the laser enters in the so-called CC regime.

In the CC regime (a typical intensity time trace is shown in Fig. 1.12c). The spectral linewidth is increased several GHz, depending on the type of laser. The widening of the linewidth is an outcome of chaotic emission [23, 72, 73], and different routes to chaos have been identified [22, 73].

In 1998, Heil et al. [70] presented a diagram showing the stable emission, LFF and CC regions, when the pump current I and the η_f feedback strength are varied, as shown in Fig 1.13. Here we see how the different regimes occur as the pump current is increased. Also, intermediates states of coexistence also occur. Although these regimes seem to be very well delimited, in this work the authors delimited them in a qualitative way, because these transitions are smooth. In Chapter 4 we present a methodology to quantitatively differentiate these regimes.

The LFF regime was first detected in 1977 by Risch and Voumard [74]. Following this work, several theoretical and empirical studies had tried to clarify the underlying physical mechanism that trigger or induce the LFF dropouts. Henry and Kazarinov [21] explained the LFF phenomena using a bistable model, where spontaneous emission noise made the system escape from a stable state. Later, in 1988, a noise-driven multimode traveling wave model was introduced by Mørk et al. [75]. They noted that if the noise was omitted in the model, LFFs were still observed, which suggested that the phenomenon was deterministic. Sacher et al. [76] confirmed this hypothesis and also classified the LFFs as a "time inverted type-II intermittency."

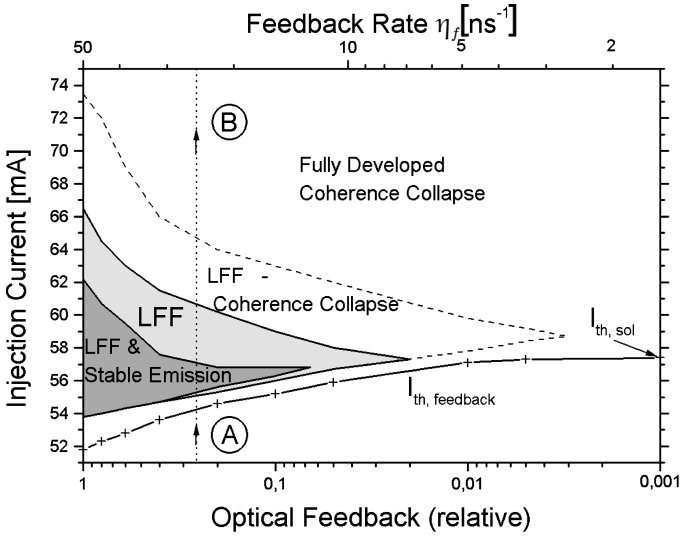

Figure 1.13: From Heil et al. [70], diagram of the different dynamical regimes in the feedback strength - pump current parameter space.

A few years later, an alternative interpretation of the LFF phenomenon, based on the analysis of the LK model [19], was introduced by Sano [24]. Sano showed that the intensity dropouts were related to the crisis between chaotic attractors and the anti-modes, which are unstable saddle-type solutions. The dropouts are followed by an intensity recovery associated with a chaotic itinerancy with a bias towards one of the stable external cavity modes, which is known as the maximum gain mode (MGM). Before the system reaches the MGM, it is dragged through different modes of the external cavity.

Since these early works, a lot of research has focused in the underlying mechanisms responsible for triggering the LFF dropouts. The presence of noise [26, 45, 46, 77] and multimode competition [30, 32] have been proposed to be important for triggering LFF dropouts.

1.5.3 Excitability of LFF dynamics.

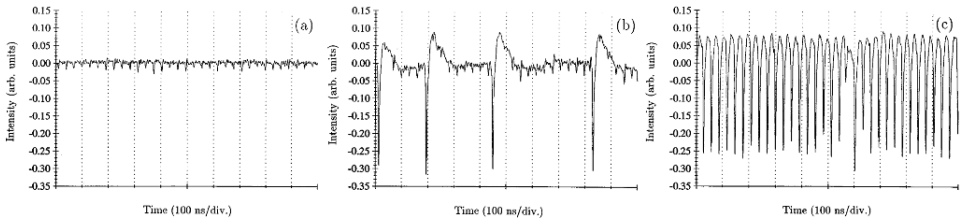

Figure 1.14: From Giudici et al. [29], output intensity of the laser for small amplitude perturbations (width: 60 ps; period: 30 ns) added into the pumping current. Three different amplitude of the pulse were used [2.6 mA; 3 mA; 10 mA], displayed in the panels (a),(b), and (c) respectively.

It is possible to induce LFFs in an SLOF by perturbing the pump current, when it is close to the laser threshold. This has been studied experimentally [29] (see Fig. 1.14) and numerically [77–79]. Giudici et al. [29] and Sukow and Gauthier [38] showed that externals inputs with amplitudes below a certain critical value pro-

duce small and linear reactions but perturbations higher than the critical value, generates a nonlinear reaction that leads to an LFF. Heil et al. [33] and Mulet and Mirasso [78] found that after a large perturbation, the system gradually recovers to its equilibrium state and is not able to react to another perturbation during a given time. These observations, the nonlinear reactions generated by perturbations above certain critical value (Fig. 1.15b), and the inability to react during a gradual recovery (Fig. 1.15c), are the definition of an excitable system [80, 81]. Another important motivation of the studies preformed in this Thesis is that optical excitable systems, that mimic neuronal behavior, have potential to be building-blocks of novel, ultra-fast, photonic information processing systems inspired by the way biological neurons process external inputs [82–93].

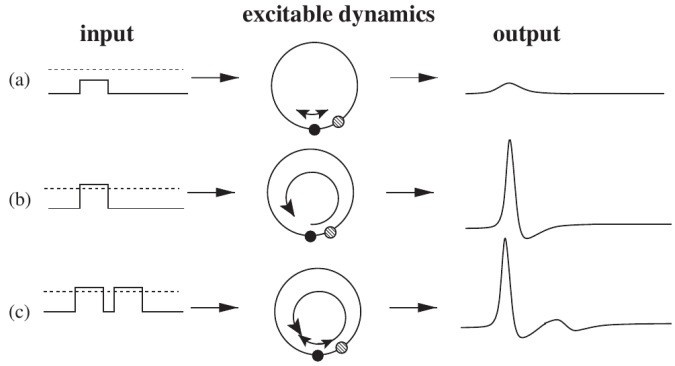

Figure 1.15: From Lindner et al. [80], features of excitability: different kinds of inputs (left column) cause different kinds of responses (right column) of the excitable dynamics (middle column). The dashed line represents the system threshold.

1.5.4 Current modulation and optical feedback.

In this Section we discuss the behavior when the laser with feedback in the LFF regime is also subject to a sinusoidal modulation in the pump current.

The dynamics induced by the interplay of feedback and modulation is relevant because semiconductor lasers are widely employed in telecommunications, where the information can be encoded by direct current modulation. It is also of very interesting because of the various dynamical regimes that can occur due to the interplay of nonlinearity, noise, periodic forcing and delayed feedback. The LFF dynamics has been investigated in detail when the laser current is modulated [29, 38, 39, 94–97]. It has been shown that the LFFs can be entrained and even suppressed by current modulation [98]. In addition, because the laser intensity in the LFF regime emulates the spiking behavior of neurons, this system allows to understand how a spiking system encodes a weak external periodic signal into a sequence of spikes.

The dynamics induced by increasing the modulation amplitude is shown in Fig. 1.16, adapted from [99]. This figure presents the intensity time series of a 650 nm laser (Hitachi HL6714G) (panels a,d,g,j), the probability distribution functions (PDF) of the inter-dropout intervals ΔT_i (panels b,e,h,k), and the return diagrams, ΔT_i vs ΔT_{i+1} (panels c,f,i,l), using four different modulation amplitudes [99]. When the modulation amplitude is increased, the inter-dropout intervals

transform into smaller multiples of the modulation period. The return diagrams show a grouped structure, like "islands", that correspond to the peaks in PDFs, similar “islands” were observed in [29, 38]. The symmetry in the return diagrams suggests that probability of ΔT_{i+1} being greater or less than ΔT_i is the same; however, Aragoneses et al. [99] demonstrated that the modulation induces correlations in the ΔT_i sequence, using a symbolic data analysis methodology that is used in this Thesis and will be presented in the following Chapter.

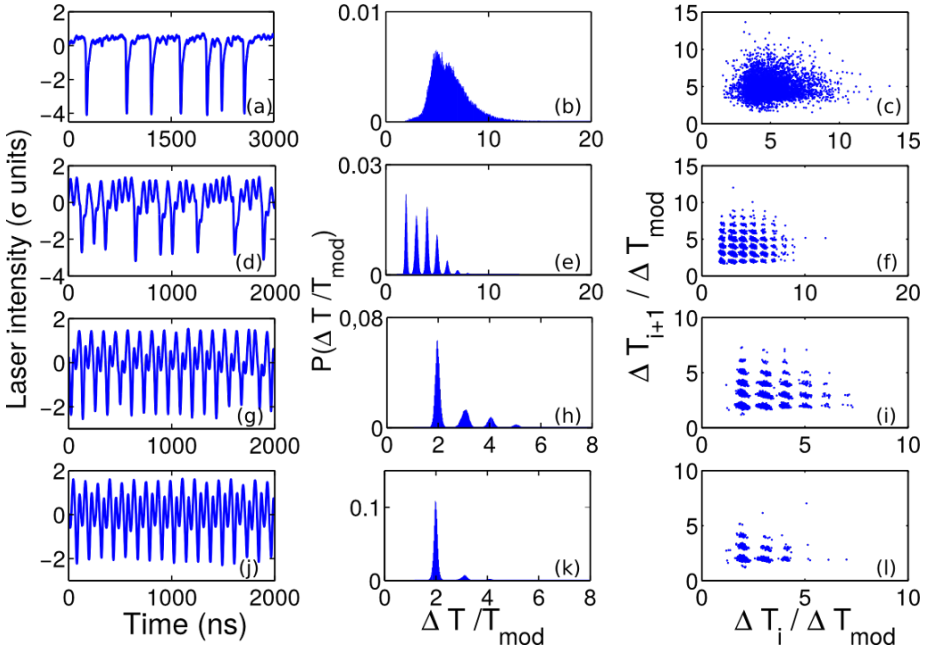

Figure 1.16: Effect of direct current modulation in an SLOF in the LFF regime. Time traces of the laser intensity (a,d,g,j), probability distribution functions (PDFs) of the inter-dropout intervals ΔT_i (b,e,h,k), and return maps (ΔT_i vs ΔT_{i+1}) (c,f,i,l) in units of the modulation period (T_{mod}) for increasing modulation amplitude: from top to bottom, no modulation, 1.2%, 1.6%, and 2% of the pump current. Adapted from [99].

Nonlinear Dynamical Systems and Symbolic Time-series Analysis.

CHAPTER 2

In this chapter, we review main concepts of non-linear dynamical systems and symbolic analysis of time series. We present two well-known examples of nonlinear systems (the logistic map and the Rössler system) which are later used in Chapter 5, to study the effects of noise on the permutation entropy and block entropy, which are also presented in this Chapter.

2.1 Nonlinear Dynamical Systems

Nonlinear systems are everywhere in nature. One of the earliest studies focusing on nonlinear systems is attributed to Henri Poincaré in 1899 [100]. While studying celestial mechanics, he realized that a slight change in the initial position of a body could lead to dramatic differences in the following states of the system. However, Poincaré's findings went unnoticed for a long time; it took almost 70 years when the meteorologist Lorenz [101] in 1963, while studying the evolution of a simple model of the atmosphere, rediscovered this sensitive on the initial conditions, thanks to the development of computers. Nevertheless, as well as Poincaré's work, Lorenz's article (whose importance is now widely recognized) was not appreciated until many years after its publication.

Nowadays, a nonlinear system whose evolution is unpredictable but depends on a relatively small number of variables is known as a chaotic dynamic system, while if it depends on a large number of variables is known as a complex dynamical system. The expansion of theoretical knowledge, the existence of high-speed computers and the development of highly refined experimental techniques, have shown that this phenomenon is abundant in nature and has applicability in many branches of science. For example, many biological systems including neurons are described by nonlinear equations. We now understand that most natural and artificial phenomena (human-made) are complex due to the ubiquity of the nonlinearity. Next, we give a brief description of two types of dynamic systems studied in this Thesis.

2.1.1 Types of dynamical Systems

If iterative functions can describe a system, we say that it is a discrete dynamical system in time. A classical example of how chaotic behaviors can be exhibited by simple mathematical systems, is the Logistic Map [102]. An iterative unidimensional map was introduced in 1976 by the biologist May, as a time-discrete analog

of a model for populations dynamics it is described by the following equation:

$$x_{n+1} = r x_n (1 - x_n), \tag{2.1}$$

where x_n is a number between zero and one that represents the ratio of existing population to the maximum possible population and $r \in (0, 4]$ is a parameter that represents the growth rate.

If the evolution of a dynamical system is described by differential equations, we have a continuous-time dynamical system. An example of chaotic behavior, which is studied in this Thesis (in Chapter 5), is the Rössler system. It was introduced in 1976 by Otto Rössler [103] as a simplified version of the Lorenz system. The equations of the Rössler system are

$$\begin{aligned} \frac{\mathrm{d}x}{\mathrm{d}t} &= -y - z \\ \frac{\mathrm{d}y}{\mathrm{d}t} &= x + ay \\ \frac{\mathrm{d}z}{\mathrm{d}t} &= b + z(x - c), \end{aligned} \tag{2.2}$$

where (x, y, z) are the three variables that evolve in the continuous time t and (a, b, c) are three parameters.

The first two equations only contain linear terms, which create oscillations if they are not coupled to the third one. However, the equation for the variable z includes the nonlinear term that allows the system to evolve to chaotic behavior. An example of the chaotic trajectory in the phase space for the parameters that we use in Chapter 5 is presented in Fig. 2.1.

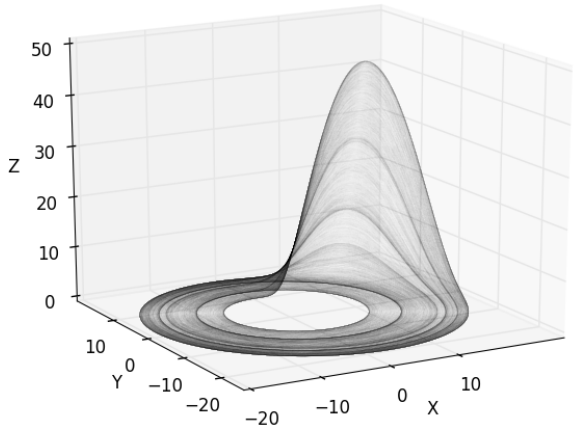

Figure 2.1: Attractor of the Rössler system. The values of the parameters $\{a, b, c\}$ used are $\{0.1, 0.1, 18.0\}$ respectively.

Time-delay Systems.

Depending on the time scales, the velocity of propagation of the information may be relevant to the dynamics. A simple example is when the equations governing the evolution of the system depend on the past state of some variables

$$\frac{\mathrm{d}\mathbf{x}}{\mathrm{d}t} = F(t, \mathbf{x}(t), \mathbf{x}(t - \tau), \beta), \tag{2.3}$$

where τ is the delay, $\mathbf{x}$ are the system states and β are system parameters. This type of equations are also known as Delay Differential Equations (DDEs), and one of the properties of this kind of system is that even with only one variable describing the state of the system, it can generate a chaotic dynamic. This is because DDEs are infinite dimensional because the initial conditions must be given as a function, i.e. an infinite set of values. In the case of equation (2.3), the function that must be provided is the value of $x(t)$ in the time interval $-\tau \leq t \leq 0$. Many processes include this delay effect phenomena in their inner dynamics; different examples can be found in the literature related to biology, chemistry and physics. One particular example and the primary interest of this Thesis is the semiconductor laser with optical feedback, where the time delay is due to the finite velocity of light and it is equal to the flight time of light in the external cavity.

2.2 Symbolic Time-series Analysis

A typical starting point for the study of many natural systems is based on a set of measurements or repeated observations of some system variables. The underlying equations or even the mechanisms that rule the dynamics are often unknown, and we want to obtain information about them from the set of observables that capture dynamic phenomena. This set of measurements, obtained at discrete sampling time, are given by a data set $X \equiv \{x_1, \cdots, x_i, \cdots, x_N\}$, where N is the number of observations.

These time series often seem irregular, very fluctuating, difficult to predict, and some of this behavior might be due to noise (in the system or to the measurement process). However, the concept of chaos has changed our way of understanding and analyzing these observed data $X(t)$ (time series), because we now know that deterministic nonlinearity can lead to behaviors that seem impossible to predict or that resemble noise. These time series, obtained from chaotic systems, occupy an intermediate place between predictable (regular or almost periodic) signals and completely stochastic signals (noise).

Nowadays, it is known that often, complex behaviors in nature can be understood as the interplay of deterministic nonlinearity, stochasticity, and high dimensionality. Then, a relevant question is: the underlying dynamics of a system is (mainly) deterministic or stochastic? Answering this question is important for a proper physical description of the system.

Distinguishing noise from deterministic dynamics is a challenging problem that has attracted a lot of attention [51, 52, 104–109]. In this context, a useful approach is based on Symbolic Time Series Analysis.

The idea behind this methodology is to transform a time-series, $X = \{x_1, x_2 \ldots x_N\}$, into a sequence of symbols, $s(t)$. There are many ways to do this [110], and in this Thesis we are going to focus on two methods: the block patterns and the Ordinal patterns.

2.2.1 Block patterns

Within this method, a time-series is discretized by dividing the phase space into Q regions, and associating a symbol to each region [111]. Then, one needs to choose a *dimension* D for defining vectors made up of consecutive symbols. For

example, let us consider the time-series obtained from the logistic map, as shown in Fig. 2.2a, but taking only a portion of this (Fig. 2.2b)

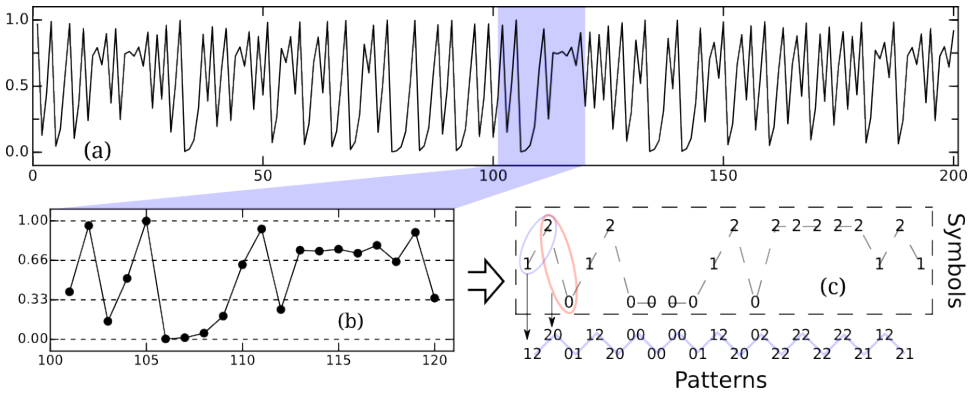

Figure 2.2: Illustration of block patterns symbolic encoding. Time series of the logistic map when the system parameter $r = 4$ and the initial condition $x_0 = 0.003$ is used. The dashed lines in (b) represent the phase space partition $\{[0, 0.33), [0.33, 0.66), [0.66, 1]\}$. Data inside each partition are represented by the symbols $[0, 1, 2]$ respectively. The original time series is represented by the symbol sequence, and finally block patterns of length $D = 2$ are constructed.

$$X = \{0.40, 0.96, 0.15, 0.51, 0.99, 0.00, 0.01, 0.05, 0.19, 0.62, \\ 0.93, 0.25, 0.75, 0.74, 0.76, 0.72, 0.79, 0.65, 0.90, 0.34\}. \tag{2.4}$$

We divide the phase space into three regions $[0, 0.33)$, $[0.33, 0.66)$ and $[0.66, 1]$, associating to them the symbols 0, 1 and 2 respectively. With $D = 2$, the blocks associated to the time-series are:

$$\{12, 20, 01, 12, 20, 00, 00, 00, 01, 12, 20, 02, 22, 22, 22, 22, 21, 12, 21\}, \tag{2.5}$$

as illustrated en Fig. 2.2.

The main drawback of this approach is that it is not obvious how to perform phase-space partition, and the statistical properties of the symbolic sequence crucially depend on the partition chosen.

2.2.2 Ordinal symbolic analysis

Bandt and Pompe introduced the ordinal symbolic analysis [112], as another approach for investigating time-series. This method is based on the order relationship between successive values instead of the values themselves. Applications to the analysis of real world time-series are provided by Amigó [113] and review by Zanin et al. [108].

To construct the ordinal patterns (OP), in the same way as in the block patterns (BP), one needs to choose the *dimension* D for defining vectors made up of consecutive entries of the time-series. The ordinal patterns (of D entries of the time-series) are defined, according to the ranking (from the largest to the smallest value). The total number of ordinal patterns of length D, is equal to the number of permutations, $D!$. Figure 2.3 displays all the possible patterns for $D = 3$ and $D = 4$. If we retrieve the previous example, the time-series of the logistic map, and we calculate the OPs with $D = 3$:

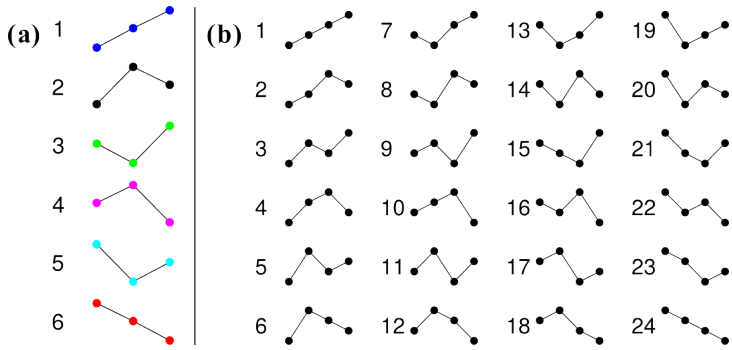

Figure 2.3: Ordinal patterns for (a) $D = 3$ and (b) $D = 4$. For both cases, the $D!$ possible patterns for are shown. This can be easily extended for larger values of n where the possible patterns will rapidly increase. Figure adapted from [114].

- $\{0.40, 0.96, 0.15\} \rightarrow 0.15 < 0.40 < 0.96 \underset{\text{pattern}}{\Longrightarrow} 120,$
- $\{0.96, 0.15, 0.51\} \rightarrow 0.15 < 0.51 < 0.96 \underset{\text{pattern}}{\Longrightarrow} 201,$
- $\{0.15, 0.51, 0.99\} \rightarrow 0.15 < 0.51 < 0.99 \underset{\text{pattern}}{\Longrightarrow} 012,$

as shown in Fig. 2.4a, Fig. 2.4b, Fig. 2.4c respectively. The sequence of patterns for the time series is

$$\begin{aligned}\{&120, 201, 012, 120, 201, 012, 012, 012, 012,\\ &120, 201, 021, 102, 120, 102, 120, 102, 120\},\end{aligned} \tag{2.6}$$

as displayed in Fig. 2.4d.

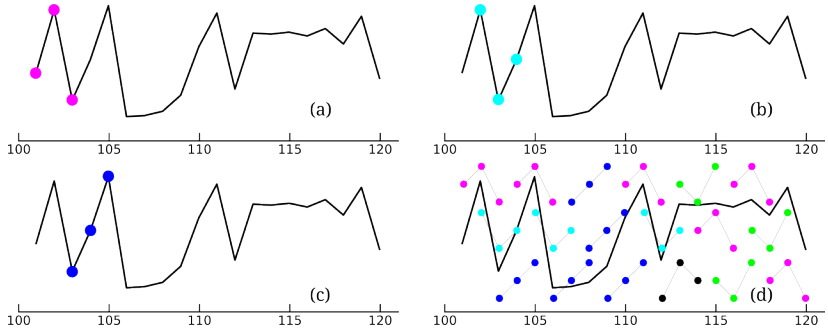

Figure 2.4: An example of ordinal patterns, for a time series generated from the Logistic map (solid black line) using $D = 3$. Panels (a),(b), and (c) display the patterns related to the first three vectors made up of consecutive entries of the time series. Panel (d) shows the sequence of patterns for this time series.

By calculating the probabilities of occurrence of the different patterns, more and less frequent patterns can be found; also information about the existence of missing, or forbidden patterns can be obtained [115–117], as an example, in the logistic map the pattern 210 is forbidden. A main advantage of the ordinal approach is that it does not require to predefine a partition of the phase-space.

Another interpretation used to understand the symbolic analysis of time series is to see symbols as letters of a language, patterns as their words. Therefore, calculating the probabilities for each pattern (word) will give us information about the

"language" associated to the dynamics of the time series under study. In addition to the probabilities of each word, another quantity that can give additional information is the transition probability matrix (TP) from each pattern to each other.

In this Thesis, the TPs are normalized such that all possible transitions from one pattern sum one; e.g. for $D = 2$,

$$\begin{aligned} &\mathrm{TP}_{01\to 01} + \mathrm{TP}_{01\to 10} = 1, \quad \text{and,} \\ &\mathrm{TP}_{10\to 01} + \mathrm{TP}_{10\to 10} = 1. \end{aligned} \tag{2.7}$$

2.2.3 Entropy

The entropy as defined by Shannon is a standard way to characterize the probabilities of the different patterns [118]. The entropy measures the disorder or lack of information in a system, and is defined, in its discrete form as:

$$H_D = -\sum_{i}^{M} p_i \ln p_i, \tag{2.8}$$

where (in the case of symbolic analysis) p_i is the frequency of occurrence of the pattern i_{th} in the time series and M is the number of possible patterns. The estimation of the entropy based in the ordinal patterns probabilities is know as *Permutation entropy* (PE) [112] and in the case of the block patterns, it is know as *Block entropy* (BE) [119, 120] (for PE, $M = D!$, while for BE, $M = Q^D$). With the development of complex systems theory, other definitions for entropy have been proposed in the literature [121], however, here we only consider the standard definition of entropy as proposed originally by Shannon.

Given this growing interest, it is relevant to understand the relation between the PE and other complexity measures. In particular, a well-established way to characterize the production of information of a dynamical system is the Kolmogorov-Sinai entropy h_{ks}, see e.g. [119, 120]. The Kolmogorov-Sinai entropy is obtained as the rate of growth of the BE, for $D \to \infty$ and in the limit of a very refined partition.

Similarly to h_{ks}, one can introduce a *permutation entropy rate* as the rate of growth for $D \to \infty$ of the PE. The PE rate and h_{ks} are not only conceptually related: for piecewise monotone interval maps on the real line, they were shown to be equal [122]. This result has been later extended to a broad class of dynamics [123, 124]. This equivalence is non-trivial considering, for example, that the number of total possible ordinal patterns grows with D as $D!$, while the number of blocks grows as Q^D. The two quantities can be equal only thanks to the large number of forbidden or missing ordinal patterns, strongly limiting the growth of the PE as D is increased.

These mathematical results clarify that, under general hypotheses, PE and BE share the same asymptotic behavior. However, due to difficulties in reaching the asymptotic regime, this equivalence can be of little use in many practical cases. For example, it has been noted [122] that the rate of convergence of the PE to the Kolmogorov-Sinai entropy is extremely slow even for one-dimensional maps, while on the contrary, BE converge very quickly, see e.g. [119].

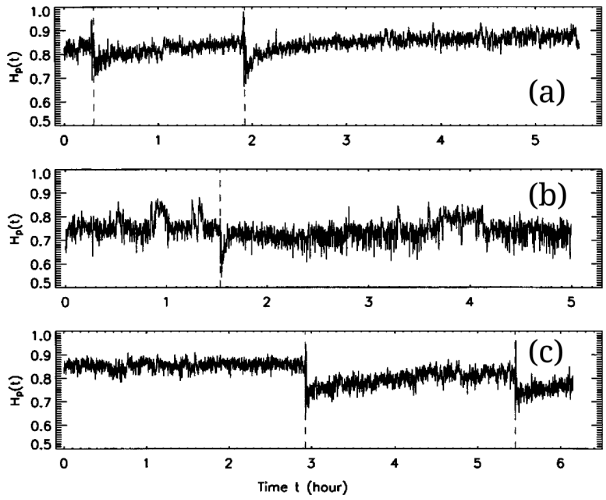

Figure 2.5: Variations of the permutation entropy with time for EEG signals of three different patients [125].

Comparing the two analyses becomes even more problematic for high-dimensional and/or noisy dynamics, such as typical experimental time-series. Consider for example the extreme case of a time series dominated by noise, in which all symbols are equally probable and temporal correlations are absent. In this case, the BE of length D is equal to $D\ln(Q)$, while the PE with patterns of length D is equal to $\ln(D!) \sim D\ln D$. This means that the BE is linear in D, with a slope $\ln(Q)$, explicitly dependent on the chosen partition, which diverges only in the limit of a very refined partition, $Q \to \infty$. In contrast, the PE grows more than linearly, so that their asymptotic slope is infinite. In both cases, the result is an infinite entropy rate. However, to discover it, in the first case one needs to construct a very refined partition. In the second case, one needs to reach large values of D to appreciate that the slope increases logarithmically. Both these tasks can be very difficult when analyzing a finite time series due to statistical limitations. In Chapter 5 we discuss the possibility of determining, by exploiting this property, whether the underlying dynamics of a system is dominated by noise or by a deterministic process.

2.2.4 Applications of the symbolic analysis

Ordinal patterns and permutation entropy have been widely used in many fields since it was proposed in 2002, from neuroscience to economics, and even in climatology [108, 126].

OPs have been employed to distinguish noise from chaos [52, 105–107], to detect noise-induced order [127], time-delay signature of chaos [128], serial correlations [47] and dependencies between two or more time series [129–135], among many other examples. Applications to experimental time series analysis include classification and discrimination of dynamical states in normal and epileptic EEG's [125, 136–139] and detection of heart rate variability under different physiological and pathological conditions [114, 140, 141].

In 2004, Cao et al. [125] have shown that permutation entropy can be effectively used to quantitatively detect dynamical changes. They analyzed EEG signals and

noticed that slightly after the seizure, the PE has a sharp drop, followed by a gradual increase, see Fig. 2.5. This indicates that the dynamics of the brain becomes more regular right after the seizure, then its irregularity increases as it approaches the normal state.

The dynamics of semiconductor lasers in the LFF regime has also been studied by using the ordinal analysis in [47–49, 53, 54]. They unveiled spike correlations, because the probabilities of OPs (constructed from consecutive inter-spike intervals) were not consistent with the uniform distribution, as seen in Fig. 2.6. In

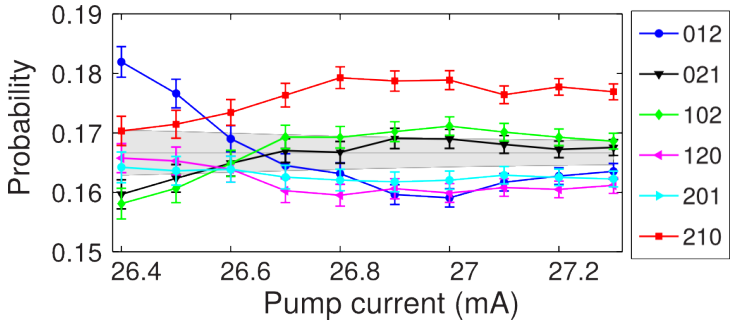

Figure 2.6: Probabilities of the six patterns vs. the laser pump current. A crossover in the hierarchical organization of the words occurs at about 26.6 mA. At lower current values, the word '012' (blue) is the most probable one, while at higher currents values, the word '210' (red) is the most probable one. Figure adapted from [53].

these works they also considered the influence of direct current modulation and identified clear changes in the dynamics as the modulation amplitude increases, as shown in Fig. 2.7.

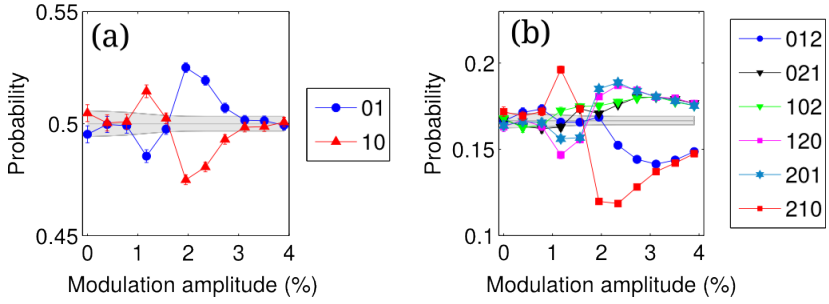

Figure 2.7: Probabilities for the patterns of $D = 2$ (a) and $D = 3$ (b) versus the modulation amplitude for the experimental data. The gray region indicates probability values consistent with 95% confidence level with a uniform distribution. Figure adapted from [99].

These works have left some open questions, for example: how correlations in the spiking laser output depend on frequency and amplitude of the modulation? Is it possible to identify the onset of different dynamical regimes? Is it possible to distinguish quantitatively different feedback-induced regimes? Hence, the following Chapters 3, 4 and 5 of this Thesis present the results obtained from the studies of time series from experimental and numerical SLOF using the method of ordinal analysis, which were carried out motivated by these questions.

Part II

Results

Chapter 3

Influence of the modulation frequency on the symbolic dynamics of the laser with optical feedback

3.1 Introduction

In this Chapter we study experimentally and numerically the dynamics of a semiconductor laser with optical feedback in the LFF regime, under different conditions of external forcing. This forcing was given to the system through the pump current, which is sinusoidally modulated, with a modulation frequency that varies over a comprehensive range encompassing the average LFF frequency without modulation. We also consider different external cavity lengths and DC current, as these two experimental parameters allow to vary the natural (unforced) frequency of the LFF dropouts. We investigate the variation of the mean inter-spike-intervals (ISI) and the ISI distribution with the modulation frequency. We also use ordinal analysis presented in Section 2.2.2, to analyze the recorded intensity dynamics.

Ordinal analysis applied to the sequence of ISI allows us to uncover the regions of noisy locking in which the frequency of the modulated LFF dropouts are govern by the modulation frequency. We also performed simulations using the Lang-Kobayashi model introduced in Subsection 1.5.1 and show that the simulations are in good qualitative agreement with experimental observations.

The experiments presented in this chapter were performed in collaboration with Dr. Taciano Sorrentino, a former PhD student of the group. The program for automated data acquisition was developed by the author and the model simulations were performed by Sorrentino. The results presented in this Chapter have been summarized in [142, 143].

3.2 Experimental Setup

The experimental setup is depicted in Fig. 3.1 and uses a 650nm AlGaInP semiconductor laser (SONY SLD1137VS) with optical feedback. The feedback was given through a mirror placed 70 cm apart from the laser cavity, with a round trip of ~5 ns. We also consider other cavity lengths that give delay times of 2.5 ns, 7.5 ns, and 10 ns, unless otherwise explicitly stated the results are presented for τ =5 ns. The laser has a solitary threshold current of I_{th} = 28.4 mA. The temperature and current of the laser were stabilized using a combi controller Thorlabs ITC501 with an accuracy of 0.01 C and 0.01 mA, respectively. The current used during the experiment was I = 29.3 mA and the temperature was set at T = 17 C. The setup was adjusted so that the threshold reduction due to feedback was about 7%.

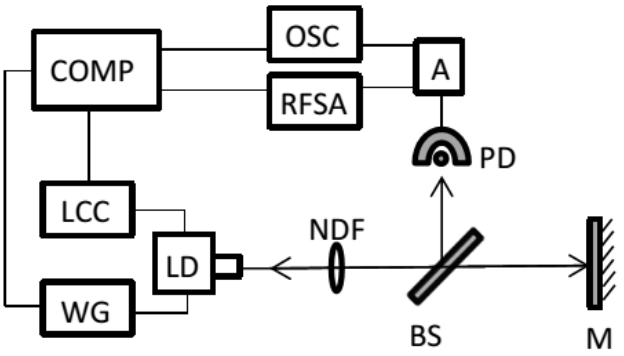

Figure 3.1: Schematics of the experimental setup. LD: laser diode; NDF: neutral density filter; BS: beam-splitter; M: mirror; PD: photo-detector; A: fast amplifier; OSC: digital storage oscilloscope; RFSA: radio frequency spectrum analyzer; COMP: computer; LCC: laser combi controller; WG: waveform generator.

The signal was captured using a photodetector (Thorlabs DET210) connected to a FEMTO HSA-Y-2-40 amplifier and registered with a 1 GHz digital oscilloscope (Agilent Infiniium DSO9104A) with 0.2 ns of sampling.

3.3 Datasets

The experiment was controlled by a LabVIEW program that acquires the intensity time series and detects the spikes. An optical spike is detected each time the intensity decreases below a preselected threshold (in the following, referred to as *detection threshold*). Because the depth of the spikes on the pump current, to be able to use a criterion to define a spike that holds for all pump currents, each intensity time series is normalized to unit variance. To avoid detecting as events the fluctuations that occur during the recovery process (after a spike), a second threshold is used: the intensity has to grow above the mean value (which is zero due to the amplifier used in the setup) before another event can be detected. In order to acquire a large number of spikes, the LabVIEW program runs until 60000 spikes are detected. Then, the program changes the modulation frequency and/or amplitude, and/or the DC value of the pump current.

3.4 Results

3.4.1 Varying the modulation frequency.

Figure 3.2 displays the measured intensity time series and the ISIs distribution for six values of the modulation frequency, f_{mod}, when the modulation amplitude is 1.2% of I_{DC}. For each frequency 30 modulation cycles are shown. The ISI distribution is computed with bins centered at integer multiples of T_{mod} (with the exception of the first bin, centered in 0). The modulation frequencies displayed are chosen to highlight different behaviors: either $n:1$ locking predominates (revealed by a high peak in the ISI distribution at nT_{mod}), or there is a transition from $n:1$ to $n+1:1$ locking, revealed by the peaks at nT_{mod} and $(n+1)T_{mod}$ having nearly the same heights.

For $f_{mod} = 7$ MHz (first row) the ISI distribution peaks at T_{mod}. The time series reveals that the ISIs are in fact heterogeneous, as in this case the bin centered in

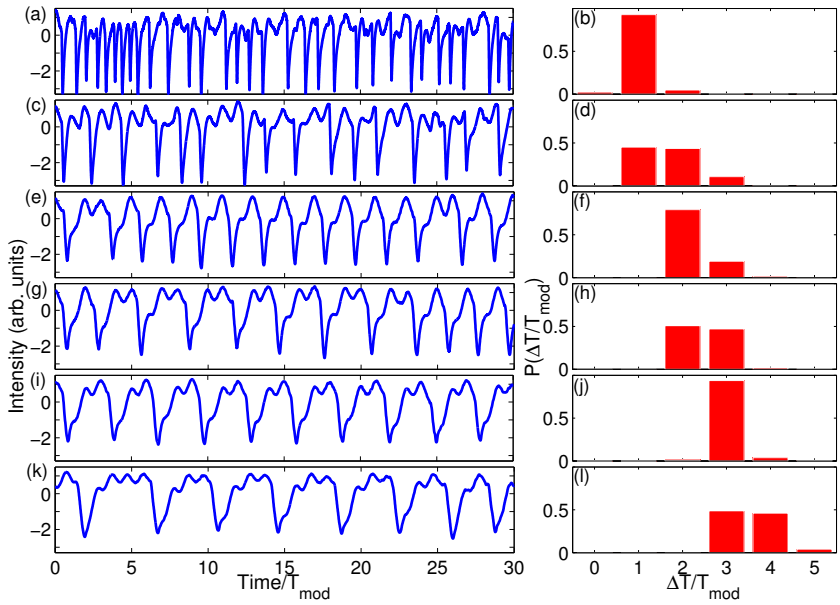

Figure 3.2: Influence of the modulation frequency in the intensity dynamic. Experimental time series of LFF intensity spikes (left column) and the corresponding ISIs (ISI) distribution (right column). The modulation amplitude is 1.2% of I_{DC} and the modulation frequency is 7 MHz (a-b); 14 MHz (c-d); 26 MHz (e-f); 31 MHz (g-h); 39 MHz (i-j); 49 MHz (k-l). In the left panels only 30 modulation cycles are shown, but the ISI distributions in the right panels are computed from 60000 ISIs.

T_{mod} is about 143 ns wide. As the modulation frequency increases, the peak in the ISI distribution shifts to higher multiples of T_{mod} and the ISIs become more homogeneous. At 26 MHz (third row) phase locking 2:1 occurs with 3:1 intermittency. In the time series, one can notice that, after a dropout occurs in a modulation cycle, the next cycle takes place during the intensity recovery time, and the consecutive spike is separated in time by $2T_{mod}$. A similar observation holds for higher frequencies, now other modulation cycles being clearly visible in the intensity oscillations between consecutive spikes. For 39 MHz (fifth row) the 3:1 pattern is dominant, and for 49 MHz (sixth row) we can see intermittent switching between 3:1 and 4:1. As the frequency increases and the modulation become faster, the ISIs become larger multiples of T_{mod} as the dropouts are spaced by an increasing number of cycles.

Figure 3.3a displays the variation of the mean ISI, $< \Delta T >$, with the forcing frequency for four modulation amplitudes (indicated as percentages of I_{DC}). A decreasing trend can be observed, interrupted by "plateaus" where $< \Delta T >$ oscillates (at about 30 MHz) and remains nearly constant (at about 45 MHz) for the two lower amplitudes, or continues to decrease for the higher amplitudes.

The origin of this behavior can be identified in Fig. 3.3b, where the ratio $< \Delta T > /T_{mod}$ is plotted vs. the modulation frequency for the same four modulation amplitudes. After an initial almost linear increase, two plateaus occur at $< \Delta T > /T_{mod} \sim 2$ and $< \Delta T > /T_{mod} \sim 3$. For strong modulation amplitude the plateaus are clear, while for weak modulation, only signatures of the plateaus are seen.

To further investigate the changes in the ISI distribution induced by the varia-

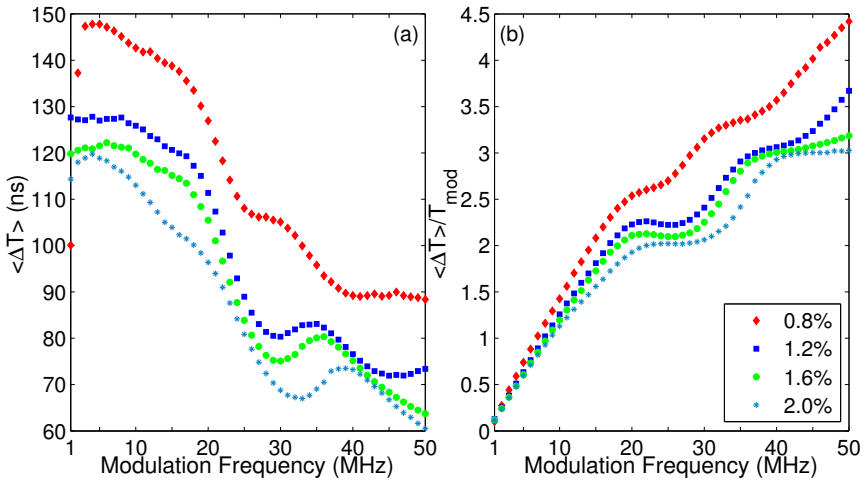

Figure 3.3: Influence of the modulation frequency in the mean ISI. (a) Mean ISI as a function of the modulation frequency for several modulation amplitudes. (b) Ratio between the mean ISI and the modulation period, $< \Delta T > /T_{mod}$, versus modulation frequency for several modulation amplitudes.

tion of the modulation frequency, the probabilities of the first 5 bins [i.e., p_n with $n = 0 \ldots 4$, p_n being the probability of an ISI interval being in the bin $(nT_{mod} - T_{mod}/2, nT_{mod} + T_{mod}/2)$] are plotted vs. f_{mod}. Figure 3.4 displays the results for the modulation amplitude of 1.2% I_{DC}. A smooth variation of the probabilities is observed over the entire frequency range. For clarity we indicate with vertical arrows the six frequencies corresponding to the panels in Fig. 3.2. It can be observed that p_1 displays a maximum (close to $p_1 = 1$) at 7 MHz, p_2, at 26 MHz and p_3, at 39 MHz, while $p_1 \sim p_2$ at 14 MHz, $p_2 \sim p_3$ at 31 MHz and $p_3 \sim p_4$ at 49 MHz.

Figure 3.5 displays the results of ordinal analysis applied to the ISI sequences, for the modulation amplitude 1.2% I_{DC}. We present results for $D = 2$ and $D = 3$. For $D = 2$ [Fig. 3.5a] we plot simultaneously three probabilities: the probability of one OP ['01', as the probability of '10' is 1-P('01')] and the probabilities of

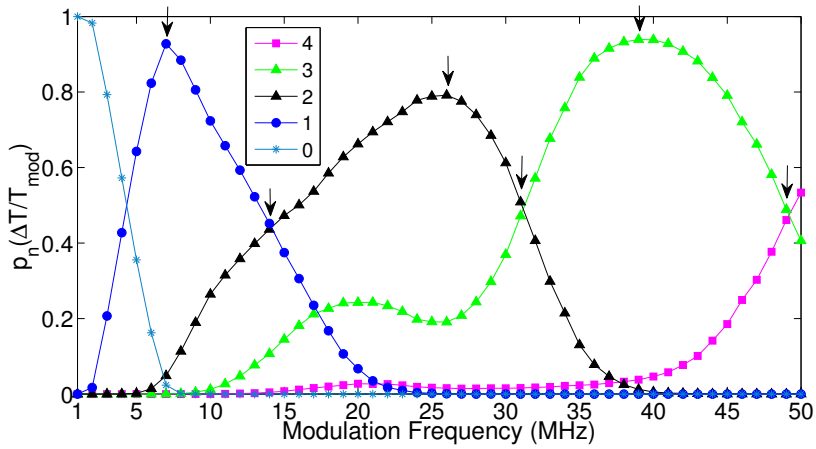

Figure 3.4: Probability, p_n, that an ISI value is within the interval $nT_{mod} - T_{mod}/2, nT_{mod} + T_{mod}/2$. n values in the legend. The first five probabilities for the modulation amplitude of 1.2% I_{DC}.

two transitions (from one OP to the same OP, as the other two TPs can also be readily calculated from the normalization conditions: $TP_{01\to01}+TP_{01\to10} = 1$ and $TP_{10\to01}+TP_{10\to10} = 1$). For $D = 3$ [Fig. 3.5b] we plot simultaneously the probabilities of the 6 OPs.

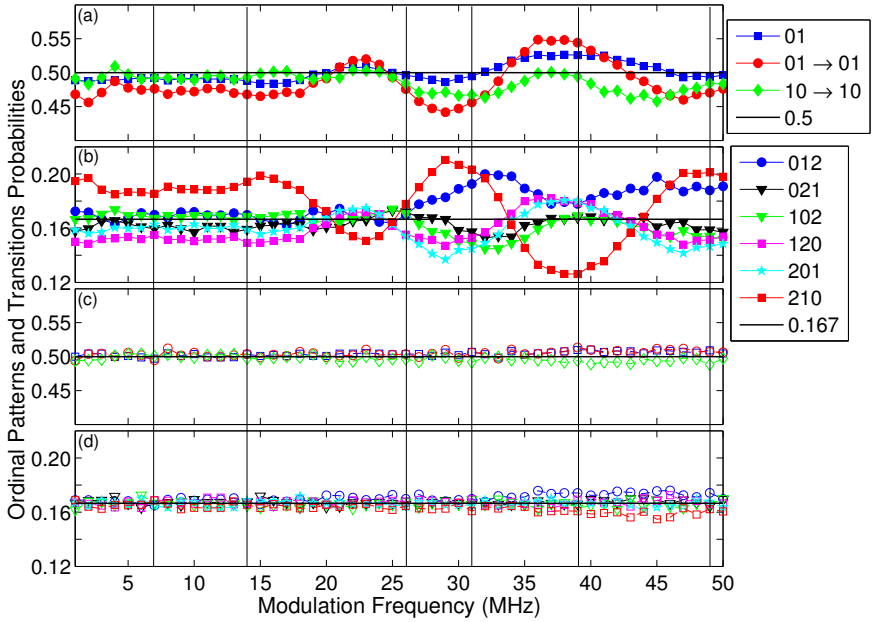

Figure 3.5: Ordinal analysis of the influence of the modulation frequency. (a) Probabilities of $D = 2$ ordinal patterns and the transition probabilities. (b) $D = 3$ OPs probabilities. (c), (d) Same as (a),(b) but when the OPs and TPs are computed from surrogate (shuffled) ISI sequences.

We can see smooth changes in these probabilities as the modulation frequency varies. The same type of smooth variation that was observed in the p_n probabilities (Fig. 3.4), is seen here, clearer in the $TP_{01\to01}$ and in the OP '210' probability (red curves). These probabilities are the ones that depart more from equiprobability and are anti-correlated.

To demonstrate that these changes are indeed significant, Figs. 3.5(c,d) display the same probabilities, but calculated after the ISIs series have been shuffled (surrogate data). We can see that in these panels all the OPs and TPs are practically equiprobable, as expected, as no correlations exist in the surrogate data.

Comparing Fig. 3.4 with panels (a,b) in Fig. 3.5, we see that at 7 MHz (when p_1 is maximum) and at 14 MHz (when $p_1 \sim p_2$) nothing remarkable occurs in the symbols' statistics. However, for higher modulation frequencies, changes in the ISI distributions manifest also in changes in the statistics of the OP probabilities and transitions between OPs: the maximum of p_2 and p_3 (occurring at 26 MHz and at 39 MHz respectively) are located just after the local maxima (minima) of the $TP_{01\to01}$ (OP '210' probability), and the "equilibrium" situations ($p_2 \sim p_3$ at 31 MHz and $p_3 \sim p_4$ and 49 MHz) occur just after the local minima (maxima) of $TP_{01\to01}$ (OP '210' probability).

To demonstrate that the above observations are robust, in Fig. 3.6 we plot the

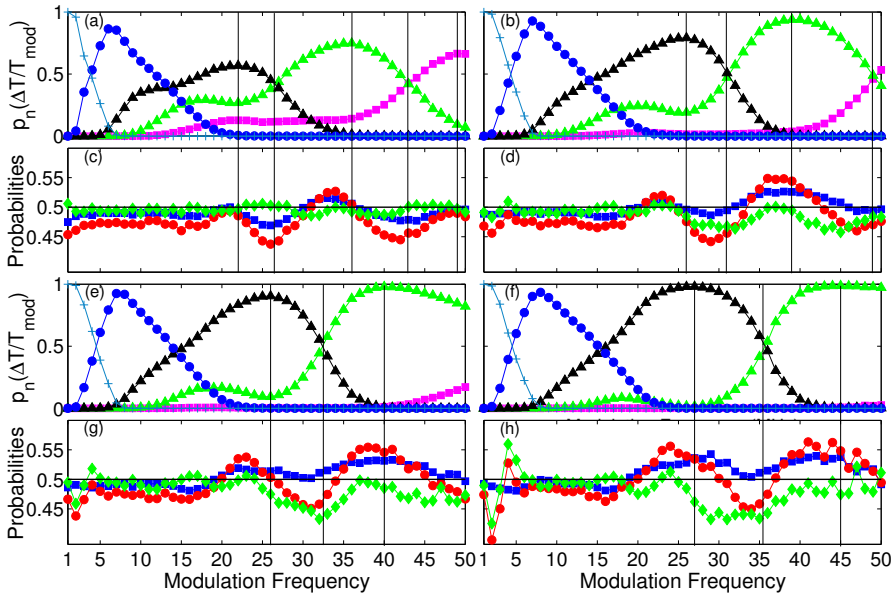

Figure 3.6: Histograms probabilities and OPs and transition probabilities for $D = 2$ versus modulation frequency for four different modulation amplitudes. 0.8% of I_{DC} (a,c); 1.2% (b,d); 1.6% (e,g); 2.0% (f,h). Legends as in Figs. 3.4 and 3.5(a).

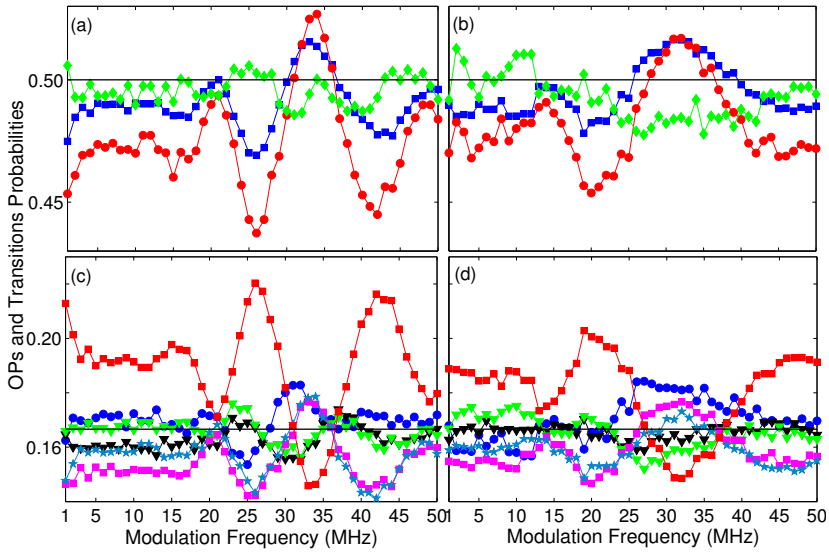

Figure 3.7: Ordinal analysis: comparison of experimental and numerical ISI data. First row: OP and transition probabilities for $D = 2$. (a) Experimental, (b) Numerical. Second row: OP probabilities for $D = 3$. (c) Experimental, (d) Numerical. Modulation amplitude of: 0.8% I_{DC} for experiments and 0.8% μ_0 for simulations. Legends as in Fig. 3.5.

probabilities $p_0 \dots p_4$, as well as the OPs and TPs, for $D = 2$, for weaker and for stronger modulation amplitudes. For the different amplitudes, above 20 MHz, the maxima and minima of the $TP_{01\to01}$ curve precede the maxima and the "equilibria" of the p_n probabilities. For strong amplitude we can see that, as p_4 (pink curve) vanishes (and therefore the "equilibrium point" between p_3 and p_4 also disappears), the local maximum and minimum in the transition probability curve also disappear. One remarkable feature is the structure that appears in the TPs in the low frequencies (< 5 MHz) with the increasing amplitude. This structure does not appear to be linked with changes in the ISI distribution, at least for the wide bins (centered at nT_{mod}) used in this analysis. We also did the experiment with different external cavity lengths corresponding to feedback delays of 2.5 ns, 7.5 ns and 10 ns. Qualitative similar behavior was observed, with similar structures also appearing in the lower frequencies for delays of 2.5 ns and 7.5 ns.

3.4.2 Experiments-model comparison

Figure 3.7 shows a comparison between experimental and numerical OP and transition probabilities for the lower experimental modulation amplitude. The simulations were preformed using the LK model described in Subsection 1.5.1 with parameters, unless otherwise stated, given in Table 1.1. The modulation amplitude is 0.8% I_{DC} for the experimental data, panels a and c in Fig. 3.7. In the simulations, panels b and d in Fig. 3.7, the modulation amplitude parameter is $a = 0.004$, corresponding to 0.8% of μ_0, the DC current parameter. For the numerical data, the effect of the modulation amplitude is less pronounced (the probabilities vary less with the frequency than in the experimental data) but present the same general trends. As discussed in Subsection 1.5.1, the model is quite simple (it takes into account only one reflection in the external cavity and neglects multimode emission, spatial and thermal effects) and thus, only a qualitative agreement could be expected. Nevertheless it is remarkable that no re-scaling or major changes in the parameters of the model are needed to reproduce the general behavior of the probabilities. More detailed numerical investigations are needed to understand this.

3.4.3 Varying the feedback time delay and DC pump value.

The effects of varying the time delay and the pump current are shown in Fig. 3.8. These two parameters affects the natural spike rate of the laser (without modulation). In these experiments the modulation amplitude is kept constant at $A_{mod} = 1.6\%$ of I_{th}. In panel 3.8a the mean ISI for three external cavities, corresponding to time delays of 2.5, 5 and 7.5 ns, are plotted against the modulation frequency. The curves for 5 and 7.5 ns present a plateau for low frequencies, followed by a rapid decrease in the mean ISIs as the modulation frequency increases, and a local minimum and maximum, after which the mean ISI varies little for 7.5 ns, and continue to decrease for 5 ns. The local minimum and maximum occur for higher frequencies in the curve for 5 ns and are absent in the curve for 2.5 ns, where the mean ISI decrease almost monotonically. When varying the current, Fig. 3.8b, the variations of the spike rate are more gradual. In panel 3.8b the curves for low I_{DC} resemble the curves for $\tau = 5$, 7.5 ns in Fig. 3.8a. As the current in-

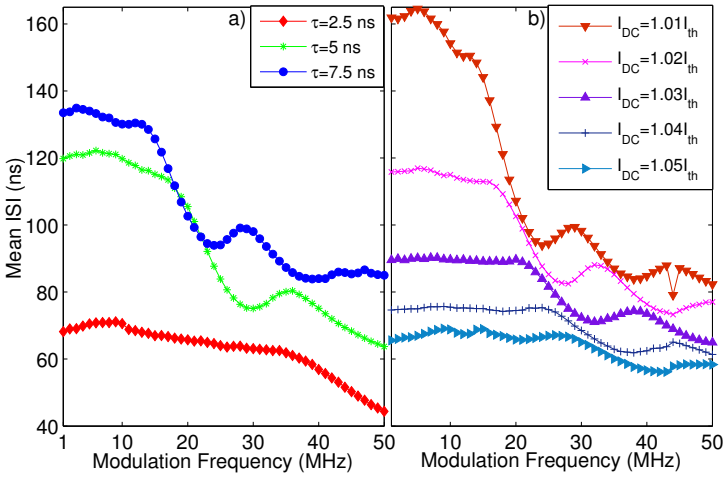

Figure 3.8: Experimental results: influence of the delay time and the DC pump current value in the mean ISI. a) Experimental mean ISI as function of the modulation frequency for three different time delays: 2.5 and 7.5 ns with $I_{DC} = 1.03I_{th}$ and 5 ns with $I_{DC} = 1.024I_{th}$, threshold reduction of 7.1%. b) Experimental mean ISI as function of the modulation frequency for five different DC currents, $\tau = 5$ ns, $A_{mod} = 1.6\%$ of I_{th}.

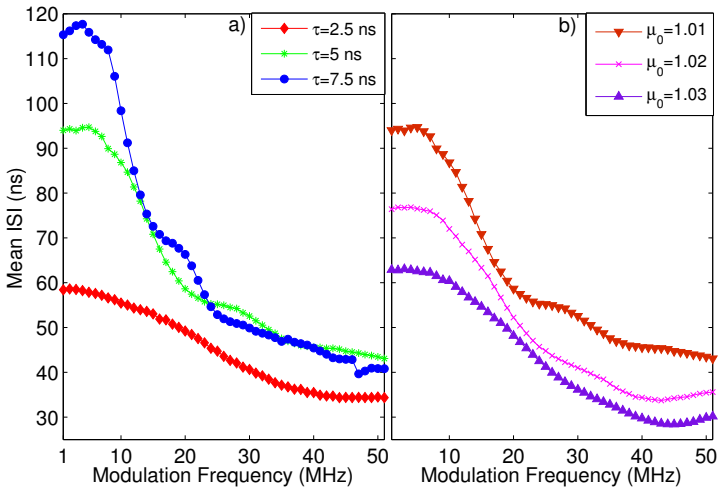

Figure 3.9: Numerical results: influence of the delay time and the DC pump current value in the mean ISI. a) Mean ISI from simulations as function of the modulation frequency for three different time delays, $\mu_0 = 1.01$. b) Mean ISI from simulations as function of the modulation frequency for three different DC current parameters, μ_0, $\tau = 5$ ns, $A_{mod} = 1.6\%$.

creases, the plateau in the low-frequency region increases and local minimum and maximum move to higher frequencies, while the curves become flattened.

Figure 3.9 presents the results of simulations. The mean ISI vs. modulation frequency for different τ and μ_0 is displayed. The numerical curves resemble the experimental ones, the plateau for low frequency and the following rapid decrease can be seen. The main difference is the oscillations that occur at intermediate and high frequencies, much stronger in the experimental curves. We can see a small oscillation in the curves for $\tau = 5, 7.5$ ns in panel 3.9a and the curve for $\mu_0 = 1.01$ in panel 3.9b.

From Figs. 3.8 and 3.9 we can see that when the parameters are such that the natural spike rate (without modulation) is slow (i.e., for long delay or low I_{DC}) then, the modulation frequency affects more strongly the mean ISI, that tents to decrease with increasing modulation frequency. In other words, when the interval spike rate is slow, a faster modulation produces faster spikes. On the contrary, when the interval spike rate is already fast (for short delay or large I_{DC}), the modulation frequency has a smaller effect on the spike rate and does not result in faster spikes. These results can be interpreted as due to the excitable nature of the LFF spikes and the refractory time, after each spike time during which, another spike is not possible.

Although ordinal symbolic analysis does not take into account the exact duration of the ISIs, it can capture subtle changes in time correlations among consecutive laser spikes. As the underlying correlations affect the probabilities of the ordinal patterns (OPs): if no correlations are present in the spike sequence, all OPs are equally probable; as there are $D!$ possible OPs of dimension D, their expected probability is $1/D!$. Thus, if there are OPs whose probability is significantly different from $1/D!$, they unveil the existence of serial correlations in the timing of the laser spikes. The analysis of the significance of the OP probabilities is done in Chapter 4, here we use a simple approach and compare with the probabilities computed from surrogate (shuffled) data.

Figure 3.10 displays the results of the analysis of the experimental data: the probability of the pattern '210' is plotted for three delays and two modulation amplitudes. By analyzing the probability of this pattern, we investigate the existence of time correlations among 4 consecutive spikes. We chose this pattern because its probability is the one that differs the most from the 1/6 value expected if no correlations are present in the spike sequence (i.e., if all the patterns are equally probable). To demonstrate that the probability of this pattern indeed unveils the presence of spike correlations, in Fig. 3.10 we also plot in empty symbols the probability of '210' computed from surrogate data, obtained by shuffling ISIs.

In panel a) of Fig. 3.10, there is an oscillation in the probability for intermediate frequencies. Observation of the changes in this oscillation pattern along the two columns (different amplitudes) and the three lines (different time delays), leads to the following conclusions: i) the increase of the modulation amplitude increases the differences between maxima and minima and moves the oscillation pattern to higher frequencies; ii) the decrease in the time delay reduces the differences between maxima and minima and moves the oscillation pattern to higher frequencies, in such a way that for 2.5 ns delay we can see only the first local minimum of

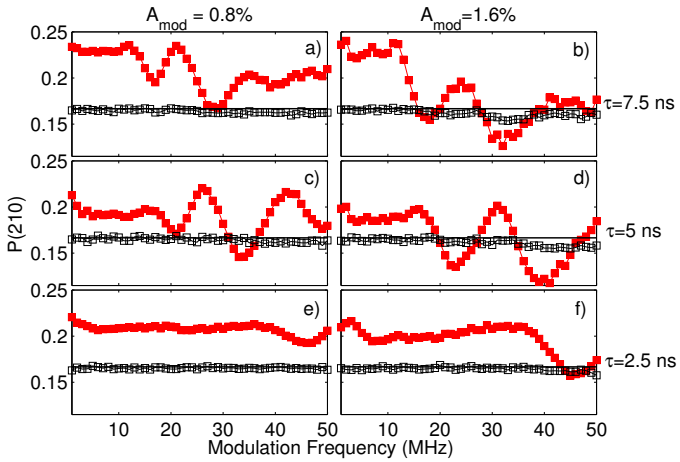

Figure 3.10: Influence of the feedback delay time: ordinal analysis of experimental ISI data. The '210' probability is plotted against modulation frequency, for two modulation amplitudes and three time delays. a-b: $\tau = 7.5$ ns, $I_{DC} = 1.03I_{th}$. c-d: $\tau = 5$ ns, $I_{DC} = 1.024I_{th}$, threshold reduction: 7.1%. e-f: $\tau = 2.5$ ns, $I_{DC} = 1.03I_{th}$. a,c,e: $A_{mod} = 0.8\%$ of I_{th}. b,e,f: $A_{mod} = 1.6\%$ of I_{th}. Full symbols: original data. Empty symbols: surrogate data.

the oscillation pattern.

In Fig. 3.11 we present the analysis of simulated data: the probability of '210' for original and surrogate data. A good agreement with the experimental results of Fig. 3.10 is observed.

A similar behavior is observed when the DC value of the injection current changes. In Fig. 3.12 we plot, for experimental ISIs, the probability of the '210' pattern for five different DC currents for the same modulation amplitudes and time delays as in Fig. 3.10. The variation of the oscillation pattern in the '210' probability when I_{DC} increases is the same as in Fig. 3.10 when τ decreases, as in both cases the intrinsic (without modulation) spike rate increases. For the higher amplitude (1.6%, second column) maxima and minima are more pronounced, and they occur at higher modulation frequencies. For increasing injection current (from top to

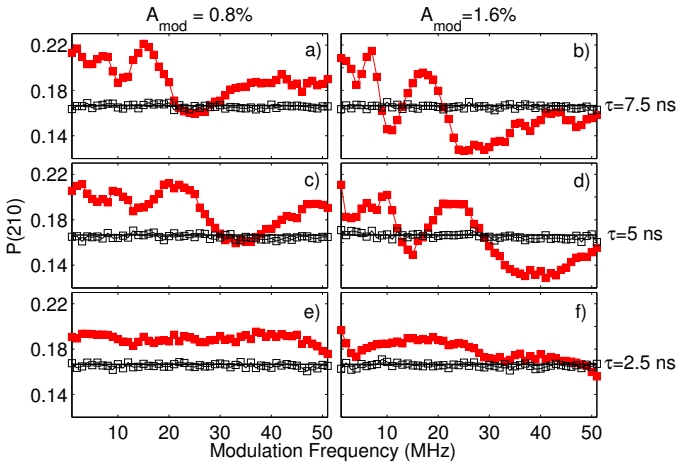

Figure 3.11: As Fig. 3.10 but the analysis is performed over simulated ISI data. a-b: $\tau = 7.5$ ns. c-d: $\tau = 5$ ns. e-f: $\tau = 2.5$ ns. a,c,e: $A_{mod} = 0.8\%$ of μ_0. b,e,f: $A_{mod} = 1.6\%$ of μ_0.

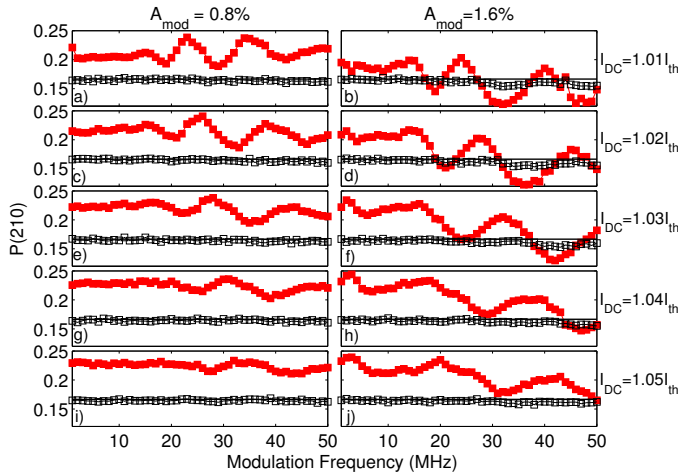

Figure 3.12: Influence of the DC value of the pump current in the ordinal probabilities computed for experimental ISI data. The '210' probability is plotted against modulation frequency, for two modulation amplitudes and five I_{DC}. τ = 5 ns. a-b: $I_{DC} = 1.01I_{th}$. c-d: $I_{DC} = 1.02I_{th}$. e-f: $I_{DC} = 1.03I_{th}$. g-h: $I_{DC} = 1.04I_{th}$. i-j: $I_{DC} = 1.05I_{th}$. a,c,e,g,i: A_{mod} = 0.8% of I_{th}. b,d,f,h,j: A_{mod} = 1.6% of I_{th}. Full symbols: original data. Empty symbols: surrogate data.

bottom) the probability curve becomes more flat, as the oscillation pattern moves to higher frequencies. These observations are also seen in simulated ISIs, Fig. 3.13, where the probabilities for the pattern '210' are plotted, for the same values of μ_0 as in Fig. 3.9b.

From the results shown in Figs. 3.12 and 3.13 we can see that, as the dynamics of the laser becomes faster and the spike rate increases (increasing the I_{DC}), the correlations among 4 consecutive spikes fades away, independently of the modulation frequencies.

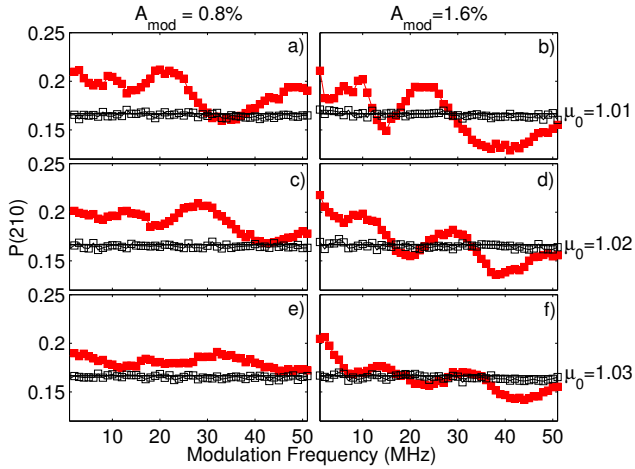

Figure 3.13: As Fig. 3.12 but the ordinal analysis is performed over simulated ISI data. a-b: μ_0 = 1.01. c-d: μ_0 = 1.02. e-f: μ_0 = 1.03. a,c,e: A_{mod} = 0.8%. b,d,f: A_{mod} = 1.6%.

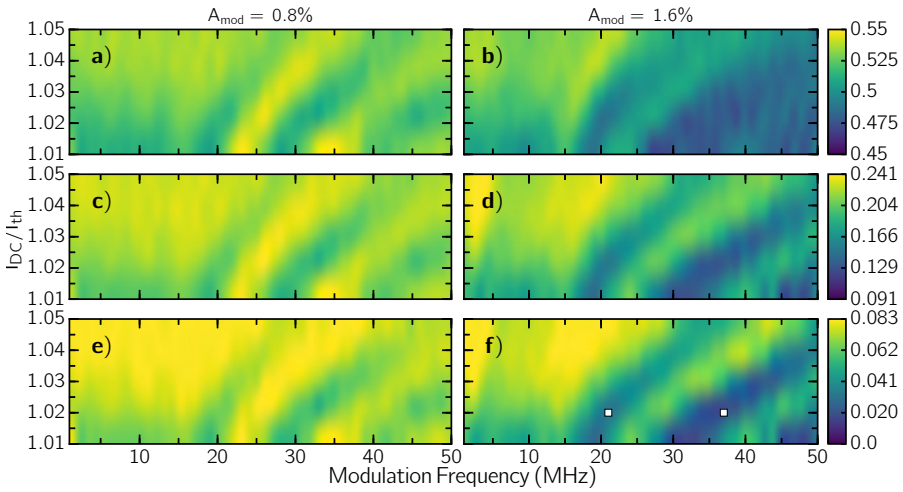

Figure 3.14: Symbolic analysis of experimental ISI data varying I_{DC} and modulation current. In the color scale the probability of '10' OP in a,b; '210' OP in c,d; and '3210' OP in e,f. In the left column the amplitude of modulation was about A_{mod} = 0.8% of I_{th}; and in the right column A_{mod} = 1.6% of I_{th}. The color scale was selected such as the equiprobable value is located at the center of the scale.

3.4.4 Noisy locking regions

Noisy locking display to simultaneously the influence of I_{DC} (that affects the natural ISIs frequency) and the forcing frequency. In Fig. 3.14, in color scale, are represented the probabilities of the '10' (top row), the '210' (middle row) and the '3210' (bottom row) patterns, for experimental data. In this Figure, the same general behavior is found for '10', 210' and '3210': as the injection current increases the maxima and minima move to higher frequencies, these can be seen in the color patterns moving to the right, and in the top, the differences between maxima and minima diminish.

From the results shown above, we observe that the correlation among several consecutive spikes are diminished when the dynamic of the laser becomes faster. Well defined regions of (I_{DC},f_{mod}) are seen, where the probabilities are close to the

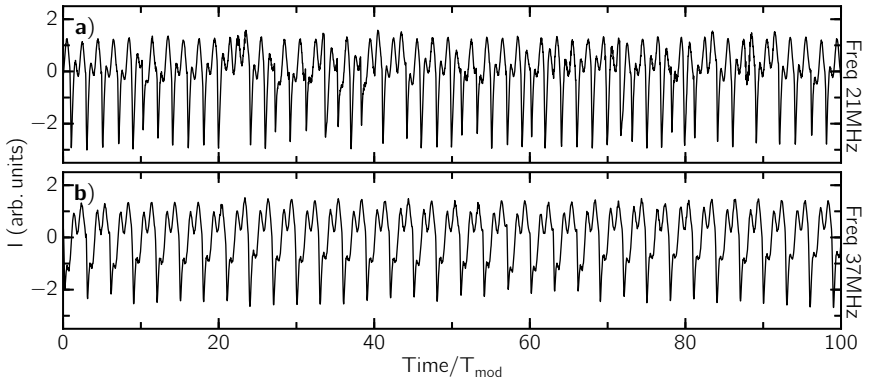

Figure 3.15: Experimental time series of LFF intensity spikes, for the set of parameters marked on the panel f) of Fig. 3.14. The modulation amplitude is 1.6% of I_{th} the modulation frequency is 21MHz and the $I_{DC} = 1.02 I_{th}$ a); 37MHz and $I_{DC} = 1.02 I_{th}$ b). In the panels only 100 modulation cycles are shown.

$1/D!$ value, expected for equally probable OPs. An inspection of the time series in these regions, Fig.3.15 presents the experimental intensity time series for the parameters marked in panel f) of Fig.3.14, for the same amplitude of modulation 1.6% of I_{th} and using different I_{DC} and modulation frequencies; $I_{DC} = 1.02\,I_{th}$ and $f_{mod} = 21$MHz in panel a) and $I_{DC} = 1.02\,I_{th}$ and $f_{mod} = 37$MHz in b). It is noted the presence of different noisy locking of the spike rate due to the modulation frequency, panel a uncovers noisy locking of type 2:1, and 3:1 in b). This results allow us to conclude that the method of the ordinal patterns allows to detect these locking regimes in the dynamics of modulated LFFs.

3.5 Summary

In this chapter, we have investigated how the spiking laser output represents a weak periodic input that was implemented by direct modulation of the laser pump current. We focused on understanding the influence of the modulation frequency and amplitude, of the feedback delay time and of the DC value of the pump current in the ISI sequences. We analyzed the datasets using the ordinal symbolic methodology. We have identified changes in the statistics of the ordinal patterns, which were related to specific changes in the ISI distribution. In addition, the analysis of the probabilities of the ordinal patterns allowed to detect different noisy locking regimes. A good qualitative agreement was also found between the LK model simulations and observations.

Chapter 4

Characterization of the regimes of semiconductor lasers with optical feedback

4.1 Introduction

In this Chapter, we use three diagnostic tools to analyze how noisy fluctuations (close to threshold) gradually transform into well-defined dropouts (LFF regime, at higher pump currents), which then merge into fast and irregular fluctuations (CC regime, at even higher pump currents). As can be seen in the video [144], in spite of the fact that the dynamical regimes are profoundly different, the transitions are gradual and an objective identification of the transition points is not possible by a simple inspection of the time series. The diagnostic tools proposed here allow us to delimit the coexistence region, where the dropouts alternate with stable noisy emission [70, 145, 146] and find a region of pump currents where occasionally, extremely depth dropouts occur. We demonstrate the robustness of our results by presenting a second set of experiments and interpret our findings concerning simulations of the LK model.

The experiments presented in this chapter were performed in collaboration with Dr. Jordi Tiana-Alsina a researcher of the group and Jordi Romà a former undergraduate student of the group, and the simulations with the Lang-Kobayashi model were carried out by the author. The results presented in this Chapter have been summarized in [147].

4.2 Experimental setup

The experimental setup is the same as the one used in the Chapter 3, with the difference that we used a different laser, a 658 nm AlGaInP semiconductor laser (Hitachi HL6501MG, threshold current $I_{th,sol} = 43.14$ mA) and used different sampling frequencies of the oscilloscope. A LabVIEW program was used to control the experiment. For each set of pump current and sampling frequency, 10 time series with 10^7 intensity data points each, were recorded.

4.3 Intensity dynamics

Recording the intensity dynamics over long time intervals while keeping the pump current constant, allows studying the alternation of noisy fluctuations and LFFs, shown in Fig. 4.1. As discussed in Subsection 1.5.2, this coexistence was first reported in [70] and has been interpreted, in the framework of the LK model, as noise-induced escapes from a stable external cavity mode [45, 46]. The detection system uses an amplifier that removes the mean value of the signal, and thus,

the zero intensity level is equal to the mean value of the intensity waveform. To quantitatively characterize, as the pump current increases, the transitions between these dynamical regimes, we use three diagnostic tools that capture different properties of the intensity time-series.

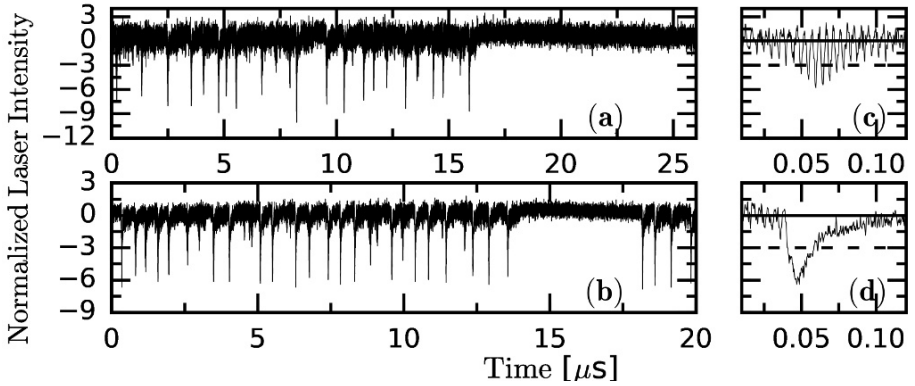

Figure 4.1: Intensity time-series (normalized to zero mean and unit variance) for I/I_{th} = 0.97 (a) and 0.98 (b). Note the different time-scale with respect to Fig. 1.12. In panel (a) the depths of the dropouts are heterogeneous, and there are dropouts below -9σ. In panel (b) the dropouts are of a similar depth, and they are less pronounced. The panels (c) and (d) display a detail of a single dropout: it is abrupt in (d), while is more gradual in (c). The horizontal dashed and solid lines in panels (c) and (d) stand for the 3σ level and the average value respectively.

4.4 Methods and Results

4.4.1 First diagnostic tool

The first method is based on the analysis of the standard deviation, σ, of intensity time-series recorded with different oscilloscope sampling rate. Figure 4.2 displays σ vs. the laser pump current, for three sampling rates. In panels (a)-(c), for each pump current, ten σ values are displayed, computed from ten time series recorded under identical conditions; in panel (d), for each set (pump current, sampling rate), the mean σ value is displayed, and in this plot we can identify five behaviors as the pump current increases:

a) Close to the lasing threshold σ is small and shows a low variability. This corresponds to stable noisy emission, shown in Fig. 1.12a.

b) For higher current, σ increases gradually and shows higher variability, capturing the development of intensity dropouts (i.e., the onset of the LFF regime). A typical intensity time trace is shown in Fig. 4.1a.

c) For slightly higher current there is a wide spread in the values of σ. This captures the coexistence between stable noisy emission and well-defined LFF dropouts [70, 145, 146]. A typical intensity time trace is shown in Fig. 4.1b.

d) For higher currents, there is an almost linear increase of σ, which captures the increase of the depth and of the frequency of the dropouts. A typical intensity time trace is shown in Fig. 1.12b. A similar linear growth was reported by Hong and Shore [42].

e) Finally, for pump currents above I/I_{th} ~1.08, σ saturates or decreases, depending on the sampling frequency. This change, previously unrecognized, cap-

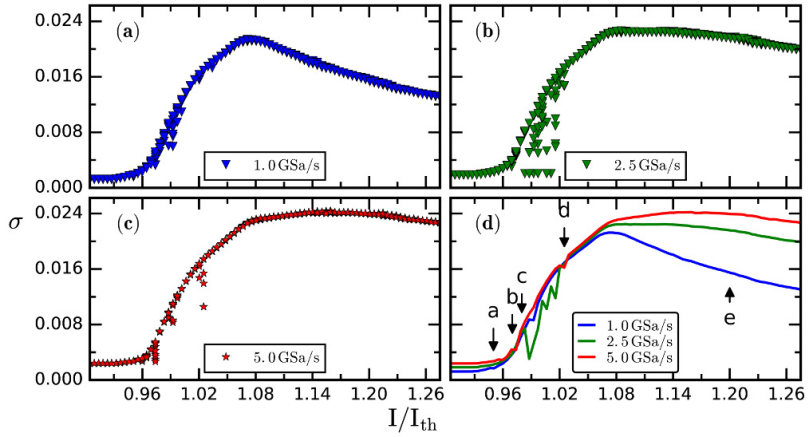

Figure 4.2: Standard deviation of the intensity time series, σ, recorded using three different sampling rates, vs. the laser pump current, normalized to the threshold value, I/I_{th}. In panels (a)-(c), for each pump current and sampling rate, ten σ values are shown; in panel (d), the average σ value is plotted vs. the normalized laser pump current, for the three sampling rates. In this panel, the arrows indicate the current values where the behaviors discussed in the text occur.

tures the fact that the dropouts become irregular and quantitatively identifies the onset of coherence collapse. A typical intensity time trace is shown in Fig. 1.12c.

4.4.2 Second diagnostic tool

The second method is based on the analysis of the number of intensity dropouts, as discussed in Chapter 3. Here we vary the detection threshold, in order to detect 'dropout-like' events, i.e. thresholds lower than -1 are used. We use a sampling frequency of 5 GSa/s because it provides a good compromise between a precise detection of the individual threshold-crossing events and detects a large number of events.

In Fig. 4.3a the number of events (averaged over ten time-series, in logarithmic scale) is plotted vs. the detection threshold, for different pump currents, which correspond to the different behaviors identified in the previous analysis of σ (the corresponding intensity probability distribution functions are shown in Appendix 4.5):

a) At low pump current [inverted triangles, the time-series was shown in Fig. 1.12a], the number of events decreases smoothly with the threshold, which is consistent with Gaussian statistics.

b) At higher pump current [circles, the time-series was shown in Fig. 4.1a], the number of events gradually decreases with the detection threshold, capturing the fact that the intensity distribution develops a tail, due to the dropouts. While there are about 10^6 events deeper than -1, few are deeper than -9 ($\sim$100).

c) At slightly higher pump current [stars, the time-series was shown in Fig. 4.1b] a plateau develops, which indicates that there is a range of thresholds for which the number of events is robust with respect to the threshold (thresholds in between -6 and -3 detect about 10^4 events). This plateau captures the fact that many dropouts are of similar depth. We note that the dropouts are less pronounced than those occurring at slightly lower pump current because no

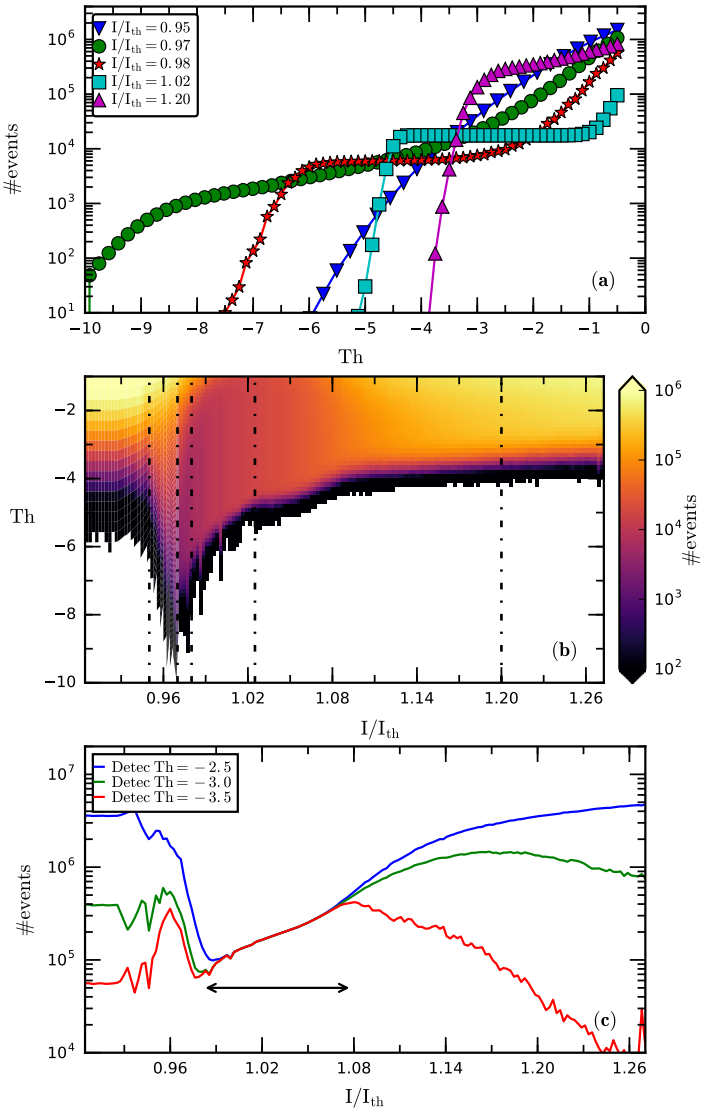

Figure 4.3: (a) Number of events (in logarithmic scale) as a function of the detection threshold (in units of σ), for different pump currents. (b) Number of events in color code (logarithmic scale) vs. the pump current and the detection threshold. The white color indicates that no events are detected. (c) Number of events in color code (logarithmic scale) vs. the pump current for three detection thresholds. The arrow indicates the boundaries of the LFF region, where the depth of the intensity dropouts is regular, and thus, the number of events is the same for the three thresholds.

event crosses the -8 threshold.

d) At higher pump current [squares, the time-series was shown in Fig. 1.12b] the plateau occurs in between -5 and -1 (thresholds in this range detect more than 10^4 events), capturing the fact that the dropouts become more frequent and less depth in units of σ.

e) For the higher pump current [triangles, the time-series was shown in Fig. 1.12c] the plateau disappears, and the number of events decreases sharply with the threshold, which indicates non-Gaussian statistics.

These findings are summarized in Fig. 4.3b that displays the number of events (in logarithmic color code) vs. the pump current and the detection threshold. The plots shown in Fig. 4.3a are obtained by moving along the dashed vertical lines in Fig. 4.3b. We note that at low pump current there are no events below -6 threshold (the white color indicates that no threshold-crossings are detected), but as the pump current increases, the detection threshold 'grows' (negatively), because dropouts gradually emerge. Then, we observe a narrow region of pump currents, $0.96 < I/I_{th} < 0.99$, where very few events (~ 100) are detected with thresholds below -8. Thus, this allows delimiting the pump current region where extremely depth dropouts occur. A further increase of the pump current results in a gradual increase of the detection threshold that captures the fact that the dropouts become less pronounced. We also note that for pump currents above $I/I_{th} \sim 1.08$, the number of events increases (note the change from dark to a lighter color). This captures the fact that the dropouts occur more often, and quantitatively identifies the onset of coherence collapse, in good agreement with the analysis of σ. The transitions can also be observed when plotting the number of events vs. the pump current, for different detection thresholds. As shown in Fig. 4.3c, there is a well-defined region where the number of detected events is the same for the different thresholds considered. This reveals that in this region the depth of the intensity dropouts is regular, and thus, quantitatively identifies the boundaries of the LFF region. In contrast, outside this region the number of detected events varies with the threshold, capturing the fact that the depth of the intensity dropouts is irregular.

4.4.3 Third diagnostic tool

The third method is based in the *ordinal analysis*. The different dynamical regimes and transitions are characterized in terms of the probabilities of occurrence of the OPs in the ISI sequence.

The probability region consistent with the uniform distribution is estimated with a binomial test: considering a confidence level of 95%, if all the OP probabilities are within the range, $p \pm 3\sigma_p$, where $p = 1/6$ and $\sigma_p = \sqrt{p(1-p)/N}$ (with N being the length of the dataset), the OP are equally probable. In contrast, if at least one probability value is above $p+3\sigma_p$ or below $p-3\sigma_p$, the OPs are not equally probable, with 95% confidence level.

The statistical significance of the the OP probabilities, this means the confidence that probabilities values that are not consistent with the uniform distribution, is estimated with a binomial test: considering a confidence level of 95%, if all the OP probabilities are within the range, $p \pm 3\sigma_p$, where $p = 1/6$ and $\sigma_p = \sqrt{p(1-p)/N}$ (with N being the length of the dataset), the OP are equally probable; in contrast, if at least one probability value is above $p + 3\sigma_p$ or below $p - 3\sigma_p$, the OPs are not equally probable, with 95% confidence level.

To detect the events, we first consider a fixed threshold, equal to -3 because it provides a good compromise between analyzing only the dropouts that are sufficiently depth (filtering noisy fluctuations), while keeping a large number of dropouts (needed to compute OP probabilities with good accuracy), in a wide range of pump currents. As shown in Fig. 4.3b, the detection threshold varies in a nontrivial way with the pump current. With -3, more than 75000 events are

detected for all pump currents.

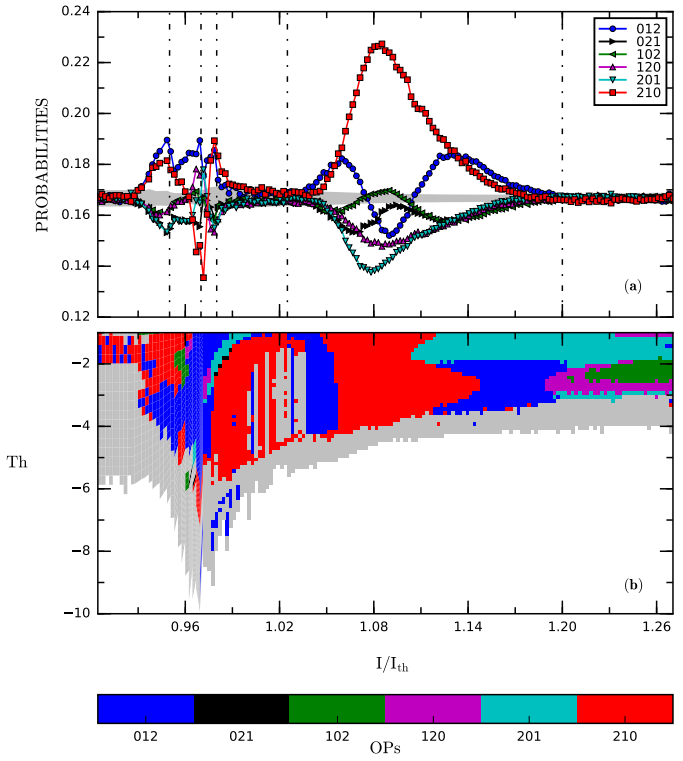

Figure 4.4: (a) Probabilities of the six $D = 3$ ordinal patterns vs. the normalized pump current, I/I_{th}. (b) Most probable OP [in the same color code as panel (a)] vs. the normalized pump current and the detection threshold. In both panel the gray regions indicates that, either the six OPs are equally probable, or the number of detected events is not enough to compute the OP probabilities with robust statistics. The white color in panel (b) indicates that no events are detected.

Figure 4.4a displays the six OP probabilities vs. the pump current. At low pump current, the OPs are equally probably, which is consistent with uncorrelated intensity fluctuations. At higher pump currents, large and abrupt variations of the OP probabilities are seen. This is the pump current region where the dropouts develop, they are heterogeneous, and few of them are very depth. The OP probabilities uncover temporal correlations which are because, in this current region, the -3 threshold detects events during the recovery process. It is worthwhile to note that the shape of the dropout waveform changes in this current region [see the panels (c) and (d) in Fig. 4.1], and the OP probabilities capture this change.

At higher pump currents the OP probabilities vary smoothly and pattern '210' becomes the most probable pattern. We note that the value of the pump current at which the probability of pattern '210' is maximum, I/I_{th}=1.08, is also the one where the onset of coherence collapse occurs, as identified by the other two diagnostic tools. For higher pump currents the OP probabilities detect additional changes in the temporal correlations among consecutive events, as pattern '012' becomes the most probable one, and then, for even higher pump currents, all pat-

terns become about equally probable (consistent with no temporal correlations among consecutive events).

Next, we analyze the influence of the detection threshold. Figure 4.4b displays, in color code, the most probable OP vs. the pump current and the detection threshold. It can be observed that there is a range of pump currents where the most probable pattern does not vary with the detection threshold ($0.96 < I/I_{th} < 1.11$). In this region, the depth of the dropouts is regular; in contrast, for other pump currents the most probable OP either varies with the detection threshold (because the depth of the dropouts is irregular), or it is not defined (because the OP probabilities are very similar).

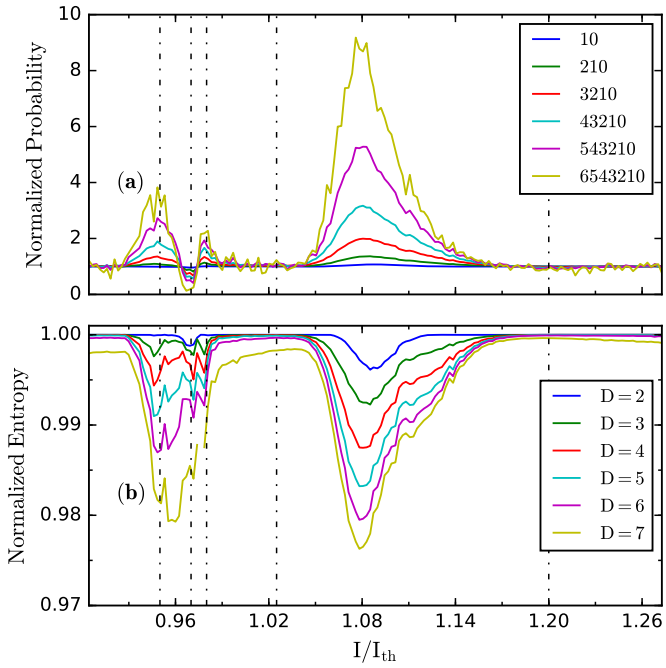

Figure 4.5: (a) Probability of the "decreasing trend" pattern of length D with $D = 2\ldots7$ (i.e., patterns 10, 210, 3210, …, 6543210) vs. the normalized pump current, I/I_{th}. For easy comparison, each probability is normalized to the value expected if the patterns are equally probable, $1/D!$. (b) Permutation entropy, normalized to its max value, computed from the probabilities of the patterns of length D (with $D = 2\ldots7$) vs. the normalized pump current. In both panels (a) and (b) regime transition points are clearly identified, which are consistent with the transition points that were detected in Fig. 4.4 with $D = 3$.

Lastly, we analyze the influence of the length of the ordinal pattern, D. Figure 4.5a displays the probability of the "decreasing trend" pattern of length D with $D = 2\ldots7$ (i.e., the probability of pattern 10, 210, 3210, …, 6543210) vs. the normalized pump current. For easy comparison, each probability is normalized to the value expected if the patterns are equally probable, $1/D!$. In this plot, the regime transition points that were identified with $D = 3$ in Fig. 4.4 are also observed for the other values of D considered. Moreover, permutation entropy, that was presented in Subsection 2.2.3, and will be analyzed in detail in the next Chapter, is another diagnostic tool that also allows to identify the regime transition points, as shown in Fig. 4.5b. The length N of the time series is 10^7 for all D values. The

influence of N will be analyzed in the next Chapter.

4.5 Complementary information

Here we include multimedia information: we present a video of the experimental dynamical transitions studied along this Chapter. We also complement the analysis by presenting the characterization of the laser output intensity using standard techniques: the light power vs. current characteristic (LI curve) and the probability density function (PDF) of the laser intensity. We also demonstrate the robustness of our findings by presenting a second set of experiments performed with a different laser, under different feedback conditions. In addition, we present simulations of the Lang-Kobayashi model, which show good qualitative agreement with the observations.

4.5.1 LI curve and intensity PDF

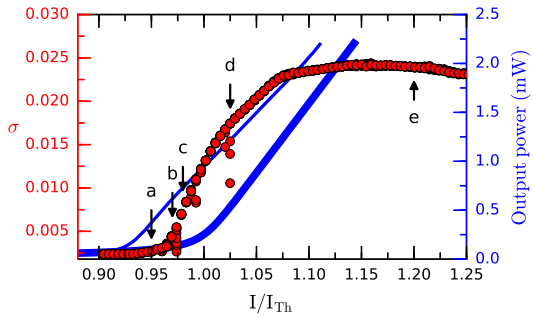

Figure 4.6: Output power (vertical right axis) and the standard deviation of the intensity fluctuations (vertical left axis) vs. the pump current, normalized to the solitary laser threshold current. The thin and thick lines represent the output power with and without optical feedback respectively. The letters indicate the values of the pump current the where different behaviors discussed in the text occur.

Figure 4.6 displays the light power vs. current characteristic (LI curve), and we indicate the pump current values where the different regimes discussed in Subsection 4.4.1 occur. For easy comparison, we also show the standard deviation of intensity fluctuations.

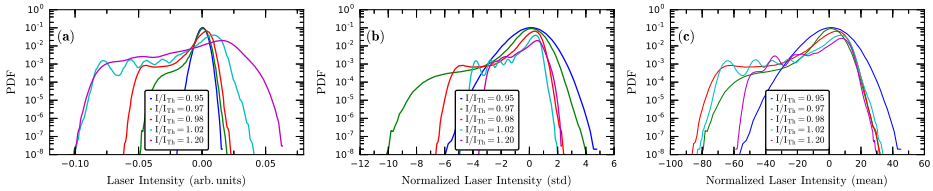

Figure 4.7: Probability density function (PDF) of the laser output intensity for five values of the normalized pump current, corresponding to the different dynamical regimes. For easy comparison, in panel (a) the intensity is displayed in arbitrary units (raw data recorded by the oscilloscope), in panel (b), it is normalized to the standard deviation, and in panel (c), to the average output power (as shown in Fig.4.6).

As discussed previously, in the LFF regime, due to intensity dropouts, the probability density function (PDF) of the intensity fluctuations, shown in Fig. 4.7, develops a tail in the left side of the distribution. In contrast, before the onset of the

LFF regime ($I/I_{th} = 0.95$), and in the CC regime ($I/I_{th} = 1.2$), the intensity PDF has a well defined cutoff. While at low current the PDF is Gaussian, in the CC regime the PDF is not Gaussian.

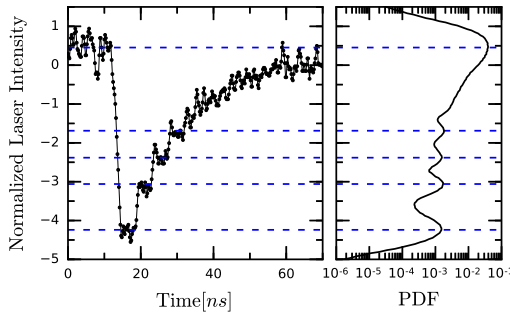

Figure 4.8: Detail of an intensity dropout when the laser pump current, normalized to the solitary threshold, is $I/I_{th} = 1.02$.

We note that for $I/I_{th} = 1.02$ the PDF displays a nontrivial structure which is due to the step-like recovery that occurs after a dropout, as shown in Fig. 4.8. These observations are in agreement and consistent with previous findings [36, 55, 57, 148, 149].

4.5.2 Second set of experimental observations

Here, we present experiments performed with a different laser and feedback conditions compared to those in the previous sections, and we find qualitatively very similar results. The laser is a 685 nm HL6750MG semiconductor laser (Opnext HL6750MG) with solitary threshold current of $I_{th} = 28.29$ mA. The feedback-induced threshold reduction and the feedback delay time are 15.42% and 5.3 ns respectively.

Figure 4.9 displays the standard deviation, σ, of the intensity time-series vs. the laser pump current, for a sampling frequency of 5 GSa/s of the oscilloscope, and a very good agreement is seen with Fig. 4.2. Figure 4.10a displays the number of events vs. the detection threshold, and here again a qualitative good agreement is found with Fig. 4.3a. It is worthwhile to note that the plateau also exists with a different detection method, as shows Fig. 4.10c: instead of normalizing the time series to standard deviation equal to one, we normalize in such way that the maximum and minimum are equal to one and zero respectively. We note that these two methods differ in the sense that with the second method any threshold value within (0,1) will detect a certain number of events, while with the first method (used in Subsection 4.4.2), the interval of detection thresholds depends on the pump current [as shown in Fig. 4.10b and Fig. 4.10b]. Nevertheless, with this alternative normalization one can also observe the existence of the plateau.

Figure 4.11 displays the six OP probabilities for $D = 3$ vs. the pump current. We note a variation very similar to that shown in Fig. 4.4a.

4.5.3 Numerical results

In the framework of the LK model, it has been shown that the LFF intensity dropouts can be either transient or sustained [145, 146], with the probability of

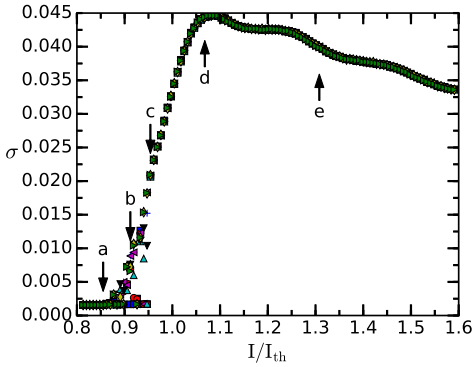

Figure 4.9: Second set of experimental results: standard deviation of intensity time series, σ, vs the normalized pump current, I/I_{th}. This plot is very similar to Fig. 4.2.

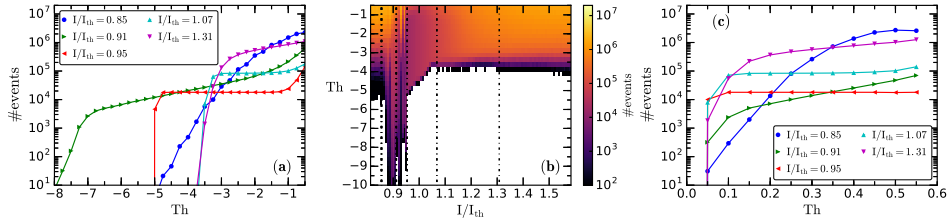

Figure 4.10: Second set of experimental results: (a) Number of events (in logarithmic scale) as a function of the detection threshold (in units of the standard deviation of the intensity fluctuations), for five values of the normalized pump current. A qualitative good agreement is seen with Fig. 4.3a. (b) Number of events in color code (logarithmic scale) vs. the pump current and the detection threshold. (c) Number of events (in logarithmic scale) as a function of the detection threshold (in this case the time series was normalize such that the maximum and minimum are equal to one and zero respectively), for five values of the normalized pump current.

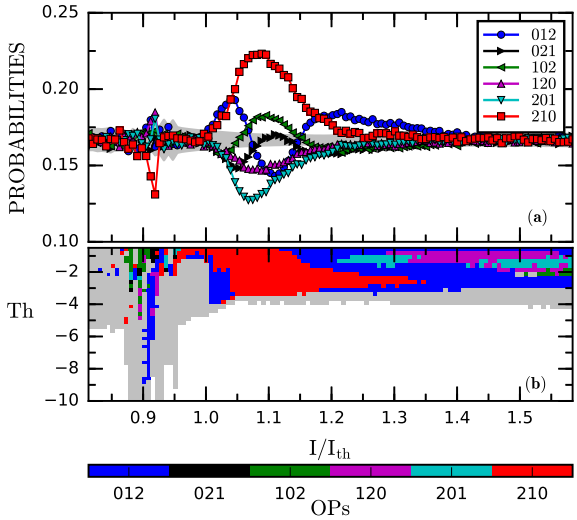

Figure 4.11: Second set of experimental results: (a) Probabilities of the six $D = 3$ ordinal patterns vs. the normalized pump current, I/I_{th}. A qualitative good agreement with Fig. 4.4a can be observed. (b) Most probable OP vs. the normalized pump current and the detection threshold.

observing sustained LFFs or stable emission depending on the relative widths of the windows where these regimes occur. For typical parameters, however, the LFF are a transient dynamics with a duration that increases with the pump current parameter [45, 46]. Typical intensity time-series are shown in Fig. 4.12.

To compare with experimental observations we need to generate a sufficiently large number of dropouts, therefore, for each value of the pump current parameter, 20 trajectories of 50 μs were generated from random initial conditions.

In Fig. 4.13 we show that, taken together, the results of the analysis of the simulated data are in very good qualitative agreement with the experimental observations: the variation of the standard deviation, Fig. 4.13a, the variation of the number of threshold-crossing, Fig. 4.13b, and the variation of the OP probabilities, Fig. 4.13c, with the pump current parameter are very similar to those encountered in the experimental data.

To conclude this comparison, Fig. 4.14 (left) displays the shape of the experimental and simulated σ curve, allowed us to determine the five values of the pump current parameter that correspond to the experimental pump currents analyzed in Subsection 4.4.1. For those values, as shown in Fig. 4.13b, the variation of the number of events is very similar to that seen in the experiments. However, it is worthwhile to note that the agreement is only qualitative: we note that the simulated dropouts are less depth than the experimental ones [in Fig. 4.13b the lowest detection threshold is -4σ]. A second discrepancy is seen in Fig. 4.14 (left), where the experimental and simulated σ curves agree qualitatively well only if the horizontal axes are shifted (i.e., $\mu = 1$ is shifted with respect to $I/I_{th} = 1$) and the vertical axes are re-scaled. The origin of these discrepancies could be the fact that in the simulations the LFFs are transient; also, the simple filtering used (a moving average in a time-window of 5 ns) might play a role. We remark that our goal here is only to demonstrate the robustness of our findings though a comparison with model simulations.

In Fig. 4.14 (right) we present the equivalent of Fig. 4.6, computed from the simulated time-series. Here again we observe a good qualitative agreement model simulations – experimental observations.

4.6 Summary

In this chapter we have applied three analysis tools to quantify various aspects of the dynamic transitions that occur as the laser pump current increases. These tools allowed us to quantitatively distinguish among stable noisy emission, coexistence between stable noisy emission and low-frequency fluctuations (LFFs), LFFs, and coherence collapse (CC). A main conclusion of our analysis is that the change in the shape of the curve of the standard deviation vs. the pump current, which is accompanied by a maximum in the probability of pattern 210, quantitatively determine the transition from LFFs to CC regime. We also found that at the onset of LFFs, rare and extremely depth dropouts occur. We have demonstrated the robustness of these observations with a second set of experiments performed with a different laser and feedback conditions, and we have also provided an interpretation of our findings in terms of simulations of the LK model.

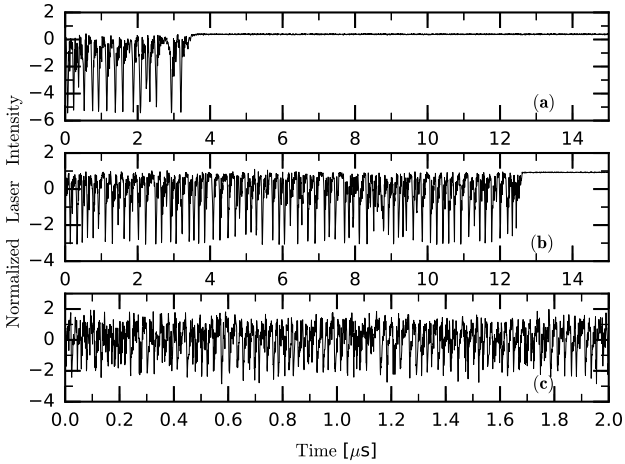

Figure 4.12: Simulated time series for three values of the pump current parameter, $\mu = 0.978$ (a), 0.982 (b) and 1.032 (c)

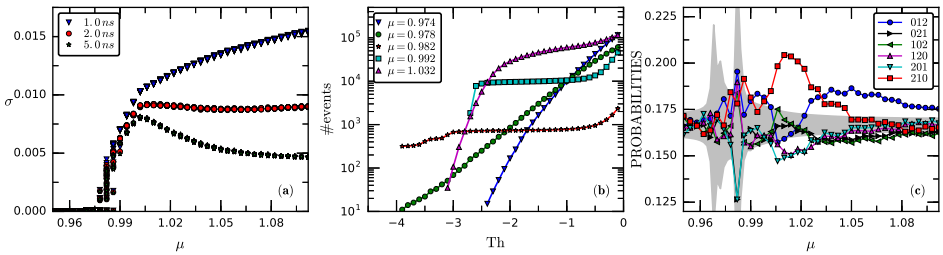

Figure 4.13: Results of numerical simulations. (a) Standard deviation of intensity time series, σ, vs the pump current parameter, μ. (b) Number of events (in logarithmic scale) as a function of the detection threshold. (c) Probabilities of the six $D = 3$ ordinal patterns vs. μ.

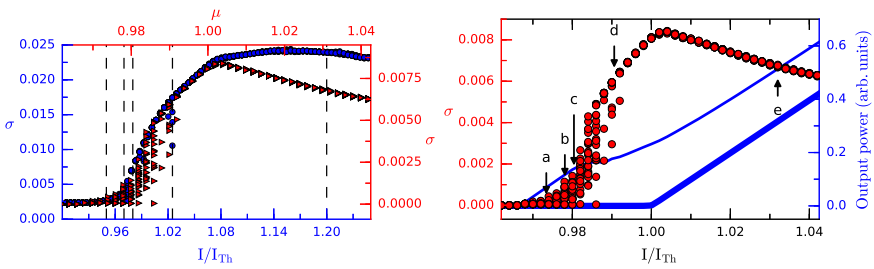

Figure 4.14: In the the left panel, the vertical left and bottom horizontal axis (in blue): standard deviation of the experimental intensity time series, σ, vs. the normalized pump current I/I_{th}; in the vertical right and upper horizontal axis (in red): standard deviation of the simulated intensity time series vs. the pump current parameter, μ. In the right panel same as Fig. 4.6 but computed from simulated data.

Effects of noise on the permutation entropy

CHAPTER 5

Because the experimental datasets analyzed in the previous Chapters are very noisy, in this Chapter we study how the presence of noise influences the ordinal method of data analysis, in particular the permutation entropy. To this aim, we first analyze time series generated from the logistic map and from the Rössler system, where we can vary the noise level in the system. Then, we analyze experimental data from the output intensity of a semiconductor laser with optical feedback. We also consider simulated data with the LK model. The datasets (experimental and numerical) are analyzed by using the two symbolic methods proposed in Section 2.2: OPs and BPs.

The simulations presented in this chapter were performed in collaboration with Dr. Simone Pigolotti, a former researcher in the group, and the experiments were carried out by the author. The results presented in this Chapter have been summarized in [150].

5.1 Datasets

5.1.1 Numerical data

We consider two dynamical systems: the one-dimensional logistic map and the three-dimensional Rössler system, presented in Subsection 2.1.1. In both cases, we study the effect of adding to the dynamical equations a Gaussian white noise, ξ_t, with $\langle \xi_t \rangle = 0$ and temporal correlation $\langle \xi_t \xi_{t'} \rangle = \delta_{t,t'}$. We also considered the case of observational noise, where the dynamic is deterministic but the noise affects the observation, obtaining very similar results (not shown).

The equation of the Logistic map with additive noise is :

$$x_{t+1} = 4x_t(1 - x_t) + \alpha \xi_t, \tag{5.1}$$

where x_t is the state of the system at iteration t and α is the noise strength. In order to constrain the variable x_t in the interval $[0,1]$, the values of ξ_t that would lead to $x_{t+1} > 1$ or $x_{t+1} < 0$ are simply discarded and redrawn. Thus, the noise ξ_t is temporally uncorrelated, but not Gaussian due to this truncation effect. To investigate the variation of the permutation entropy with the noise strength, we computed the permutation entropy, for each value of α, from time series of length $N = 1.2 \times 10^7$. We have also studied other nonlinear one-dimensional maps (Tent, Bernoulli and Quadratic) and obtained very similar results to those of the logistic map (not shown).

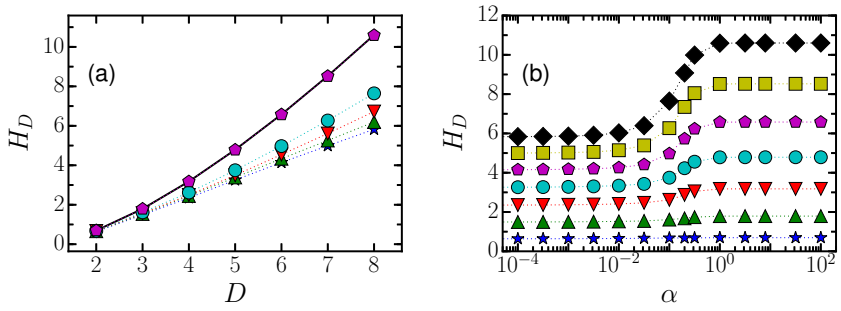

Figure 5.1: Permutation entropy (H_D) as a function of the size of the ordinal pattern (D) and the noise strength (α) for data generated from the Logistic map. (a) H_D vs D for $\alpha = 1\times10^{-4}$ (stars), $\alpha = 2\times10^{-2}$ (triangles), $\alpha = 5\times10^{-2}$ (inverted triangles), $\alpha = 0.1$ (circles), α =1 (pentagons) and $H_{max} = \ln D!$ (solid line). (b) H_D versus α for $D = 2$ (stars), $D = 3$ (triangles), $D = 4$ (inverted triangles), $D = 5$ (circles), $D = 6$ (pentagons), $D = 7$ (squares) and $D = 8$ (diamonds).

In the case of the Rössler system, the Gaussian white noise was added to the X variable as :

$$\begin{aligned} \dot{X} &= -Y - Z + \alpha\xi(t), \\ \dot{Y} &= X + aY \\ \dot{Z} &= b + Z(X - c) \end{aligned} \tag{5.2}$$

where $\{X, Y, Z\}$ are the states of the system at time t, α is the noise strength and $\{a, b, c\}$ are the parameters set at $\{0.1, 0.1, 18.0\}$, respectively.

To apply the symbolic methods (ordinal patterns or blocks) we need to discretize the dynamics. Instead of employing temporal sampling [151], we introduce a Poincaré section at $X = 0$, and analyze the time intervals between consecutive crossings of the Poincaré plane. The reason for this choice is that it is conceptually similar to how we discretize the experimental time series, as discussed in the next subsection. For each value of α, the permutation entropy is computed from time-series of $N = 1.2\times10^7$ data points.

5.1.2 Experimental data

The experimental setup is the same as in Section 3.2, without the waveform generator, and uses a 650 nm AlGaInP semiconductor laser (SONY SLD1137VS) and has a solitary threshold current of $I_{th} = 28.4$ mA. The intensity time series were acquired from the oscilloscope by a LabVIEW program that uses a threshold to detect the times when the intensity drops and calculates the time intervals between successive threshold crossings (in the following, referred to as inter-spike-intervals, ISIs). We recorded in this way time series of ore than 10^5 consecutive ISIs.

5.2 Results

5.2.1 Logistic map

Figure 5.1a displays the permutation entropy, H_D, vs the dimension of the ordinal patterns, D, computed from time series of the logistic map at different noise strengths. It can be observed that H_D increases monotonically with D, regardless

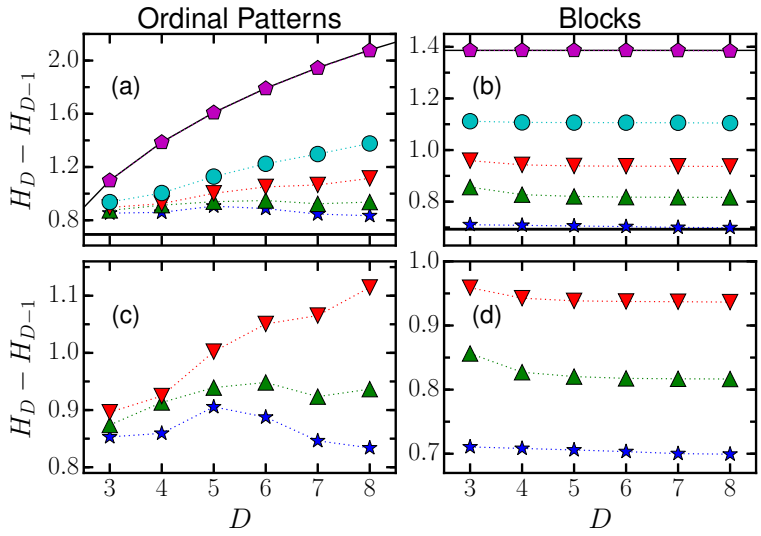

Figure 5.2: Comparison of the entropy computed from ordinal patterns, and the entropy computed from the blocks, for the Logistic map. The difference $H_D - H_{D-1}$ is plotted vs. the dimension of the ordinal patterns (a,c) and of the blocks (b,d) for various values of noise strength [the noise strengths are as in Fig. 5.1a]. In panels (a) and (b) the solid lines indicate the asymptotic values for low noise (thick) and high noise (thin). Panel (c) and (d) display a detail of (a) and (b).

of the noise strength. As the noise increases, H_D approaches its maximum value, corresponding to equally probable ordinal patterns, $H_{max} = \ln D!$ (solid black line). Note that at $\alpha = 1$ (pentagons) the values of H_D is already very close to H_{max}. Figure 5.1b displays H_D as a function of the noise strength α. A clear transition from low-noise to high-noise can be observed, for a value of the noise strength approximately independent of D. The difference between the values of the entropies at low and high noise becomes more pronounced as D increases.

To further investigate this transition, Fig. 5.2a displays the difference $H_D - H_{D-1}$ as a function of D, for various values of noise strength. As before, we indicate with a thin black line the noise-dominated limit in which all patterns are equiprobable, $H_D - H_{D-1} = (\ln D! - \ln(D-1)!)$. In the opposite limit of almost-deterministic, as D grows, the expected value of $H_D - H_{D-1}$ is the Kolmogorov-Sinai entropy [122], which for a one-dimensional chaotic map is equal to the Lyapunov exponent λ. In the case of logistic map for a parameter set at four one has $\lambda = \ln 2$, indicated by the thick black line. As shown in detail in Fig. 5.2c, we identify three possibilities:

- a almost-deterministic regime in which $H_D - H_{D-1}$ decreases for large D,
- a noise-dominated regime in which $H_D - H_{D-1}$ increases for large D,
- an intermediate regime in which $H_D - H_{D-1}$ remains nearly constant with D.

In principle, this qualitative feature of the permutation entropy can be applied to experimental time series to assess whether the dynamic is dominated by noise or by the deterministic dynamics.

We remind that this distinction can not be done for the block entropy, as in this case $H_D - H_{D-1}$ is necessarily a decreasing function of D (see e.g.[118, 152]).

This fundamental difference between permutation entropy and block entropy can be appreciated by comparing the left and right panels of Fig. 5.2.

5.2.2 Rössler system

For the analysis of time series of the Rössler system, we considered the Poincaré plane $X = 0$, shown in Fig. 5.3a, and analyzed the sequence of time intervals between consecutive crossings. Figure 5.3b shows the difference $H_D - H_{D-1}$ vs D, for different values of α. The solid line indicates the expected value if all ordinal patterns were equally probable, $H_D - H_{D-1} = \ln D! - \ln(D-1)!$. Because of the high level of stochasticity, we calculate the confidence interval that is consistent with the null hypoThesis of equally probable ordinal patterns: in Fig. 5.3b the gray region represents the expected value $\pm 3\sigma$, where σ is the standard deviation calculated for a hundred surrogated (shuffle) time-series.

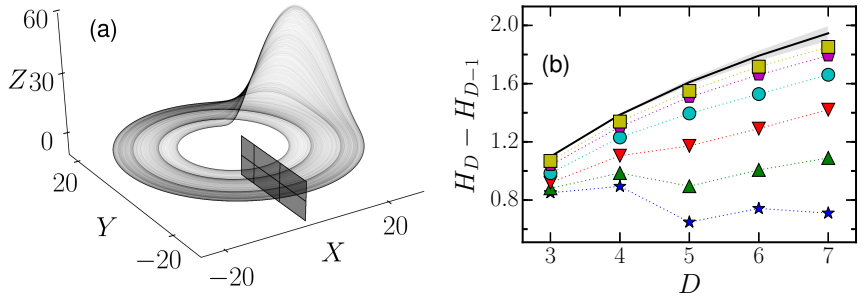

Figure 5.3: (a) Rössler attractor and Poincaré section in $X = 0$. (b) Permutation entropy difference, $H_D - H_{D-1}$, vs the dimension of the ordinal patterns, D, for noise strength $\alpha = [0$ (star), 0.8 (triangle), 1.6 (inverted triangle), 2.4 (circle), 3.2 (pentagon), 4 (square)]. The gray region indicates the values of $H_D - H_{D-1}$ that are consistent with equally probable ordinal patterns (see text for details). For the smallest value of alpha, $H_D - H_{D-1}$ shows a non-monotonic behavior, while for higher values of the noise strength, $H_D - H_{D-1}$ grows monotonically with D.

Before testing the method in experimental data, we want to investigate how the choice of the Poincaré section influences the results. We consider a Poincaré section in the plane $Z = \beta$, as shown in Fig. 5.4a, and varying β in the range $[0.05 - 26.7]$, for a fixed value of $\alpha = 0$. In this case, to discretize the time series, we analyze the time values when the trajectory intersects the Poincaré section and Z grows.

Figure 5.4b displays the difference $H_D - H_{D-1}$ vs. D, for different values of β. We can see that the difference $H_D - H_{D-1}$ increases with β. This is due to the fact that, as β is increased, consecutive values in the time-series become increasingly uncorrelated, similarly to when increasing the noise strength. On the contrary, for the minimum value of β, the variation of $H_D - H_{D-1}$ with D is resemblant to the behavior under almost-deterministic observed in Fig. 5.3b.

5.2.3 Laser dynamics: experimental data and LK model data

Next, we analyze experimental data from the laser output intensity, displayed in Fig. 5.5a. To discretized the data we consider, we used the same method as in Section 3.3. Figure 5.5b displays the difference $H_D - H_{D-1}$ vs. D, for different thresholds. Note that $H_D - H_{D-1}$ varies with the threshold in a similar way as in Fig. 5.4b: as the threshold decreases, correlations between consecutive dropouts

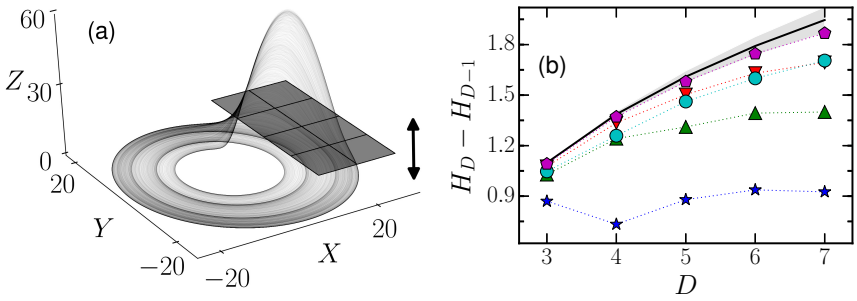

Figure 5.4: (a) Rössler attractor and Poincaré section placed in $z = \beta$. (b) Permutation entropy difference, $H_D - H_{D-1}$, vs the dimension of the ordinal patterns, D, for $\beta = 0.05$ (stars), $\beta = 6.7$ (triangles), $\beta = 13.4$ (inverted triangles), $\beta = 20.0$(circles), $\beta = 26.7$ (pentagons). The behavior is qualitatively similar to the one observed in Fig. 5.3b.

are lost.

For all the thresholds, $H_D - H_{D-1}$ grows monotonically with D. The reason is that the empirical time series is very noisy and the "almost-deterministic" regime is not seen, not even for the highest threshold. Nevertheless, the values of $H_D - H_{D-1}$ lie outside the gray region that indicates values consistent with equally probable ordinal patterns. This reveals that the sequence of intensity dropouts are not completely uncorrelated, and thus, this method can determine regularities also in very noisy data.

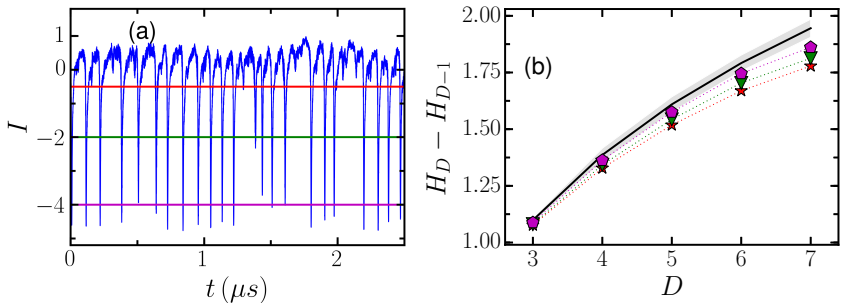

Figure 5.5: (a) Experimentally recorded time-series for the output intensity of a semiconductor laser, which operates in the low-frequency fluctuations (LFFs) regime, induced by self time-delayed optical feedback. The horizontal lines indicate the thresholds used to detect the dropout times. (b) Permutation entropy difference, $H_D - H_{D-1}$, vs the dimension of the ordinal patterns, for different thresholds: −0.5 (stars), −2 (inverted triangles) and −4 (pentagons).

The time-delayed Lang-Kobayashi model (Section 1.5.1) is used to compare time-series generated by this model with the experimental ones. The parameters are as in [143]. We use the same threshold value as with the experimental time series. We calculated data sets of more than 10^6 consecutive time intervals. Results are in Figure 5.6. One can observe a very good agreement with the experimental results.

5.2.4 Influence of the length of the time series

Finally, we consider the issue of the length of the time series. If the time series is too short, the statistics to compute the probabilities of patterns is insufficient, and the entropy is underestimated. Figure 5.7 displays the estimated value of the

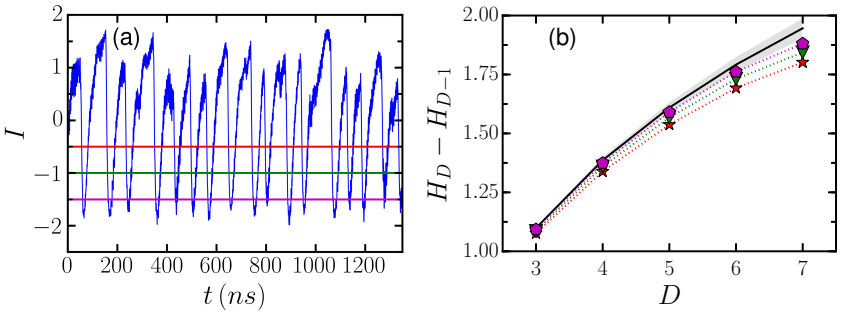

Figure 5.6: As in Fig. 5.5 but the data are generated from simulations of the LK model, with parameters as in Table 1.1.

permutation entropy vs. the length of the time series, for different dimensions of the ordinal patterns. Notice that the data requirements increases with D. As the number of possible patterns of length D is equal to $D!$, we analyzed time series of length $N = 300\ D_{\max}$ for the simulations, where $D_{\max}$ is the maximum dimension considered $D = 8$; and for the experiment $N = 10\ D_{\max}$ with $D = 7$. The vertical dotted line marks the length corresponding to this criterion and demonstrates that the permutation entropy is computed with sufficient statistics.

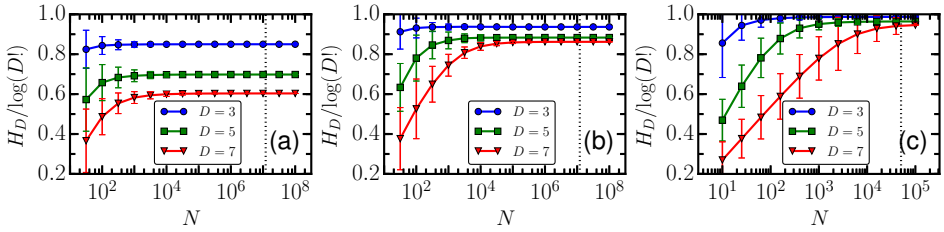

Figure 5.7: Dependence of the normalized permutation entropy, $H_D/\log D!$, on the length, N, of the time-series. In panels (a),(b) the data was generated with the logistic map and different noise levels (0.01, 0.2); in panel (c) the data is the inter-spike-intervals, recorded experimentally (the data set is the same as that in Fig. 5.5 with threshold −0.5). The solid lines represent the permutation entropy computed for the different dimensions (D); the vertical dotted line indicates the length used in previous figures.

5.3 Summary

In this chapter we have studied the effect of noise in the permutation entropy and we have compared with the effect of noise in the block entropy. We have analyzed simulated data (generated with the Logistic map and the Rossler chaotic system) and empirical data (the inter-spike intervals in the experimental output intensity of a laser in the LFF regime). In the simulated data, when increasing the noise strength, a transition between a almost-deterministic regime and a noise-dominated regime was clearly observed. The noise value at which this transition occurs is nearly independent of the size of the ordinal pattern. This transition was not detected with the block entropy. In the experimental time series the "almost-deterministic" regime was not observed, due to the fact that the data is very noisy; however, the analysis allowed to detect regularities of the underlying dynamics, and simulations of the LK model were found to be in good agreement with the empirical data.

Summary, conclusions, and future work

CHAPTER 6

In this Thesis, we have presented experimental and numerical studies of the nonlinear dynamics of a semiconductor laser with optical feedback. We have investigated the role of the modulation frequency in the LFFs dynamics, we have characterized the noise LFF-CC transition, and we haved analyzed the influence of the noise in the ordinal method of time-series analysis, that was used to analyze the lasers data.

6.1 Summary and conclusions

We can summarize the results presented in this Thesis as follow:

- In Chapter 3 we have experimentally investigated the spiking output of a semiconductor laser with optical feedback in the LFF regime, under weak current modulation. In this regime, the laser behaves as a weakly forced excitable system. With increasing modulation frequency, the ISIs become larger multiples of the modulation period. We found that the mean ISI does not decrease monotonically as the modulation frequency increases, but displays smooth oscillations and plateau-like behavior due to noisy locking. By using a ordinal analysis, we identified subtle changes in the correlations present in the ISI sequence (revealed by variations in the probabilities of the ordinal patterns and transitions), that complement the information extracted from the ISI distribution. The smooth variations in the symbolic probabilities were shown to be related to changes in the ISI distribution. For increasing modulation amplitude we observed that the locking regions migrate to higher frequencies, became wider and the locking became more clearer. We have also shown that simulations of the Lang and Kobayashi model are in good qualitative agreement with the experimental results.

- In Chapter 3 we have also studied how the external cavity length (i.e., the feedback delay time, τ) and the DC value of the injection current, I_{DC}, affect the mean (ISI) and the spike correlations. When the laser spike rate, without modulation, is slow (which occurs for large τ or for low I_{DC}), increasing the modulation frequency results in considerably faster spikes; on the contrary, if the spike rate is fast (for short τ or for high I_{DC}), the modulation frequency has only a small effect on the spike rate, and fast modulation is unable to produce much faster spikes.

We have also studied how τ and I_{DC} affect the probabilities of the OPs that represent increasingly close spikes: '3210', '210' and '10'. We used a clearly visible oscillation in the OPs' probability, when it is plotted against the modulation frequency. We found an equivalent effect when decreasing τ or when increasing I_{DC}, as the oscillation moves to higher modulation frequency and the differences between maxima and minima fade out. As the intrinsic spiking dynamics becomes faster, the effects of the current modulation become less pronounced. Once again, simulations of the Lang and Kobayashi model were found to be in a good qualitative agreement with the experimental observations.

- In Chapter 4 we have used three analysis tools to identify and characterize transitions between different dynamical regimes, as the laser pump current increases. These tools capture different properties of these regimes and *quantitatively* distinguish among stable noisy emission, coexistence between stable noisy emission and low-frequency fluctuations (LFFs), LFFs, and coherence collapse (CC).

  A main conclusion of our analysis is that the change in the shape of the curve of the standard deviation vs. the pump current (shown in Fig. 4.2), which is accompanied by a maximum in the probability of pattern '210' (shown in Fig. 4.4 and occurring at the same value of the laser pump current), quantitatively determine the transition from LFFs to CC regime. We also found that, at the onset of LFFs, rare and extremely depth dropouts occur. These analysis tools also provided objective measures for delimiting the borders of the pump current region where stable emission and the LFF regime coexist.

- In Chapter 5 we have studied the influence of noise in the permutation entropy, considering both, simulated data and experimental data. In the simulated data, when increasing the noise strength, a transition between an almost-deterministic regime and a noise-dominated regime was clearly detected. The noise value at which this transition occurs is roughly independent of the size D of the ordinal pattern.

  In the almost-deterministic regime, the permutation entropy grows almost linearly or sub-linearly with D. This behavior is qualitatively similar to that of the block entropy. However, to observe a quantitative equivalence, it is often needed to analyze extremely long time series, which can be computationally unfeasible even for relatively simple dynamical systems. In the noise-dominated regime, the growth is faster than linear, i.e. the differences $H_D - H_{D-1}$ increase with D. In principle, while this fact can be used to determine whether a dynamical system is in a noise-dominated or in a determinism-dominated regime, care must be taken in interpreting the results, because time series generated by purely deterministic systems can lead to OPs which look effectively noisy, as we demonstrated in the example of the Rössler system. This fact reflects the well-known difficulties of distinguishing deterministic dynamics from noise.

6.2 Perspectives for future work

From the results obtained in this Thesis, there are several open questions that deserve to be addressed

- The feedback strength is an important parameter for the dynamics of the system and it would be interesting a study of the effects of this parameter on the spike correlations, i.e, its influence in the probabilities of the ordinal patterns.
- In this Thesis, for the external perturbations given to the SLOF we have only used a sinusoidal modulation. An interesting extension of this work would be to change the type of perturbation by one which is, for example, aperiodic pulse. This research is being carried out by Dr. J. Tiana-Alsina and M. Masoliver using a sequence of spikes generated from a neuron model.
- In Chapter 5 we focused on the study of the effect of Gaussian white (uncorrelated) noise. It would be interesting in a future study to consider a time-correlated noise.
- It will be interesting to apply methods to detect dynamical transitions occurring for increasing feedback strength (from regime I to regime V in the diagram of Fig. 1.11), i.e., moving along a horizontal line in the Fig. 1.13.
- In the analysis carried out in Chapter 3, a fixed threshold was used to define the spikes, however, in Chapter 4, we have seen that the threshold can significantly affect the number of spikes in lower current region, where the spikes are of irregular depth. Therefore, it would be interesting to analyze the role of the threshold used to define the spikes and how it affects the detection of the noisy locking regimes.
- It will be interesting to extend the analysis of the influence of noise in the PE to other definitions of entropy (e.g Tsallis entropy [121]).
- In the study of dynamical transitions (noise-LFFs-CC), the intensity time series were recorded while keeping the pump current constant. It would be interesting to explore the possible existence of a hysteresis by recording the intensity dynamics, while simultaneously increasing and decreasing the pump current, e.g., by using a triangular signal applied through the wave form generator.
- It would also be interesting to study how the transition points depend on the feedback delay time, and if similar transitions can be detected in the dynamics of coupled lasers.

Bibliography

[1] M. Planck, "Zur Theorie des Gesetzes der Energieverteilung im Normalspektrum", *Deutschen Physikalischen Gesellschaft* **2**, 237 (1900).

[2] A. Einstein, "Über einen die Erzeugung und Verwandlung des Lichtes betreffenden heuristischen Gesichtspunkt", *Annalen der Physik* **322**, 132 (1905).

[3] A. Einstein, "Zur quantentheorie der strahlung", *Physikalische Zeitschrift* **18**, 121 (1917).

[4] T. H. Maiman, "Stimulated Optical Radiation in Ruby", *Nature* **187**, 493 (1960).

[5] T. H. Maiman, "Optical and Microwave-Optical Experiments in Ruby", *Physical Review Letters* **4**, 564 (1960).

[6] C. Weiss and R. Vilaseca. *Dynamics of lasers*. Nonlinear systems. VCH, 1991.

[7] W. T. Silfvast. *Laser fundamentals*. Cambridge University Press, 2004.

[8] R. N. Hall, G. E. Fenner, J. D. Kingsley, T. J. Soltys, and R. O. Carlson, "Coherent Light Emission From GaAs Junctions", *Physical Review Letters* **9**, 366 (1962).

[9] M. I. Nathan, W. P. Dumke, G. Burns, F. H. Dill Jr., and G. Lasher, "Stimulated emission of radiation from GaAs p-n junctions", *Applied Physics Letters* **1**, 62 (1962).

[10] T. M. Quist, R. H. Rediker, R. J. Keyes, W. E. Krag, B. Lax, A. L. McWhorter, and H. J. Zeigler, "Semiconductor maser of GaAs", *Applied Physics Letters* **1**, 91 (1962).

[11] N. Holonyak Jr. and S. F. Bevacqua, "Coherent (visible) light emission from Ga (As1-xPx) junctions", *Applied Physics Letters* **1**, 82 (1962).

[12] J.-M. Liu. *Photonic devices*. Cambridge University Press, 2009.

[13] J. Ohtsubo. *Semiconductor lasers: stability, instability and chaos*. Vol. 111. Springer, 2012.

[14] J. Tiana-Alsina. "Stochasticity, Complexity and Synchronization in Semiconductor Lasers". PhD thesis. Terrassa, Spain: Universitat Politècnica de Catalunya, 2011.

[15] H. Haken, "Analogy between higher instabilities in fluids and lasers", *Physics Letters A* **53**, 77 (1975).

[16] F. Arecchi, G. Lippi, G. Puccioni, and J. Tredicce, "Deterministic chaos in laser with injected signal", *Optics Communications* **51**, 308 (1984).

[17] C. Henry, "Theory of the linewidth of semiconductor lasers", *IEEE Journal of Quantum Electronics* **18**, 259 (1982).

[18] D. M. Kane and K. A. Shore. *Unlocking dynamical diversity: optical feedback effects on semiconductor lasers*. John Wiley & Sons, 2005.

[19] R. Lang and K. Kobayashi, "External optical feedback effects on semiconductor injection laser properties", *IEEE Journal of Quantum Electronics* **16**, 347 (1980).

[20] D. Lenstra, B. Verbeek, and A. D. Boef, "Coherence collapse in single-mode semiconductor lasers due to optical feedback", *IEEE Journal of Quantum Electronics* **21**, 674 (1985).

[21] C. Henry and R. Kazarinov, "Instability of semiconductor lasers due to optical feedback from distant reflectors", *IEEE Journal of Quantum Electronics* **22**, 294 (1986).

[22] J. Sacher, W. Elsäßer, and E. O. Göbel, "Intermittency in the coherence collapse of a semiconductor laser with external feedback", *Physical Review Letters* **63**, 2224 (1989).

[23] J. Mørk, B. Tromborg, and J. Mark, "Chaos in semiconductor lasers with optical feedback: theory and experiment", *IEEE Journal of Quantum Electronics* **28**, 93 (1992).

[24] T. Sano, "Antimode dynamics and chaotic itinerancy in the coherence collapse of semiconductor lasers with optical feedback", *Physical Review A* **50**, 2719 (1994).

[25] A. M. Levine, G. H. M. van Tartwijk, D. Lenstra, and T. Erneux, "Diode lasers with optical feedback: Stability of the maximum gain mode", *Physical Review A* **52**, R3436 (1995).

[26] A. Hohl, H. J. C. van der Linden, and R. Roy, "Determinism and stochasticity of power-dropout events insemiconductor lasers with optical feedback", *Optics Letters* **20**, 2396 (1995).

[27] D. W. Sukow, J. R. Gardner, and D. J. Gauthier, "Statistics of power-dropout events in semiconductor lasers with time-delayed optical feedback", *Physical Review A* **56**, R3370 (1997).

[28] G. Huyet, S. Hegarty, M. Giudici, B. de Bruyn, and J. G. McInerney, "Statistical properties of the dynamics of semiconductor lasers with optical feedback", *Europhysics Letters* **40**, 619 (1997).

[29] M. Giudici, C. Green, G. Giacomelli, U. Nespolo, and J. R. Tredicce, "Andronov bifurcation and excitability in semiconductor lasers with optical feedback", *Physical Review E* **55**, 6414 (1997).

[30] G. Vaschenko, M. Giudici, J. J. Rocca, C. S. Menoni, J. R. Tredicce, and S. Balle, "Temporal Dynamics of Semiconductor Lasers with Optical Feedback", *Physical Review Letters* **81**, 5536 (1998).

[31] V. Ahlers, U. Parlitz, and W. Lauterborn, "Hyperchaotic dynamics and synchronization of external-cavity semiconductor lasers", *Physical Review E* **58**, 7208 (1998).

[32] G. Huyet, S. Balle, M. Giudici, C. Green, G. Giacomelli, and J. Tredicce, "Low frequency fluctuations and multimode operation of a semiconductor laser with optical feedback", *Optics Communications* **149**, 341 (1998).

[33] T. Heil, I. Fischer, W. Elsässer, J. Mulet, and C. R. Mirasso, "Statistical properties of low-frequency fluctuations during single-mode operation in distributed-feedback lasers: experiments and modeling", *Optics Letters* **24**, 1275 (1999).

[34] D. W. Sukow, T. Heil, I. Fischer, A. Gavrielides, A. Hohl-AbiChedid, and W. Elsäßer, "Picosecond intensity statistics of semiconductor lasers operating in the low-frequency fluctuation regime", *Physical Review A* **60**, 667 (1999).

[35] C. Masoller and N. B. Abraham, "Low-frequency fluctuations in vertical-cavity surface-emitting semiconductor lasers with optical feedback", *Physical Review A* **59**, 3021 (1999).

[36] Y. Liu, P. Davis, and Y. Takiguchi, "Recovery process of low-frequency fluctuations in laser diodes with external optical feedback", *Physical Review E* **60**, 6595 (1999).

[37] A. Hohl and A. Gavrielides, "Bifurcation Cascade in a Semiconductor Laser Subject to Optical Feedback", *Physical Review Letters* **82**, 1148 (1999).

[38] D. W. Sukow and D. J. Gauthier, "Entraining power-dropout events in an external-cavity semiconductor laser using weak modulation of the injection current", *IEEE Journal of Quantum Electronics* **36**, 175 (2000).

[39] W.-S. Lam, P. N. Guzdar, and R. Roy, "Effect of Spontaneous Emission Noise and Modulation on Semiconductor Lasers Near Threshold with Optical Feedback", *International Journal of Modern Physics B* **17**, 4123 (2003).

[40] J. F. Martinez Avila, H. L. D. de S. Cavalcante, and J. R. R. Leite, "Experimental Deterministic Coherence Resonance", *Physical Review Letters* **93**, 144101 (2004).

[41] W.-S. Lam, W. Ray, P. N. Guzdar, and R. Roy, "Measurement of Hurst Exponents for Semiconductor Laser Phase Dynamics", *Physical Review Letters* **94**, 010602 (2005).

[42] Y. Hong and K. A. Shore, "Statistical measures of the power dropout ratio in semiconductor lasers subject to optical feedback", *Optics Letters* **30**, 3332 (2005).

[43] J. M. Méndez, J. Aliaga, and G. B. Mindlin, "Limits on the excitable behavior of a semiconductor laser with optical feedback", *Physical Review E* **71**, 026231 (2005).

[44] R. Vicente, J. Dauden, P. Colet, and R. Toral, "Analysis and characterization of the hyperchaos generated by a semiconductor laser subject to a delayed feedback loop", *IEEE Journal of Quantum Electronics* **41**, 541 (2005).

[45] A. Torcini, S. Barland, G. Giacomelli, and F. Marin, "Low-frequency fluctuations in vertical cavity lasers: Experiments versus Lang-Kobayashi dynamics", *Physical Review A* **74**, 063801 (2006).

[46] J. Zamora-Munt, C. Masoller, and J. García-Ojalvo, "Transient low-frequency fluctuations in semiconductor lasers with optical feedback", *Physical Review A* **81**, 033820 (2010).

[47] J. Tiana-Alsina, M. C. Torrent, O. A. Rosso, C. Masoller, and J. Garcia-Ojalvo, "Quantifying the statistical complexity of low-frequency fluctuations in semiconductor lasers with optical feedback", *Physical Review A* **82**, 013819 (2010).

[48] M. C. Soriano, L. Zunino, O. A. Rosso, I. Fischer, and C. R. Mirasso, "Time Scales of a Chaotic Semiconductor Laser With Optical Feedback Under the Lens of a Permutation Information Analysis", *IEEE Journal of Quantum Electronics* **47**, 252 (2011).

[49] N. Rubido, J. Tiana-Alsina, M. C. Torrent, J. García-Ojalvo, and C. Masoller, "Language organization and temporal correlations in the spiking activity of an excitable laser: Experiments and model comparison", *Physical Review E* **84**, 026202 (2011).

[50] D. Brunner, X. Porte, M. C. Soriano, and I. Fischer, "Real-time frequency dynamics and high-resolution spectra of a semiconductor laser with delayed feedback", *Scientific Reports* **2**, 732 (2012).

[51] K. Hicke, X. Porte, and I. Fischer, "Characterizing the deterministic nature of individual power dropouts in semiconductor lasers subject to delayed feedback", *Physical Review E* **88**, 052904 (2013).

[52] A. Aragoneses, N. Rubido, J. Tiana-Alsina, M. C. Torrent, and C. Masoller, "Distinguishing signatures of determinism and stochasticity in spiking complex systems", *Scientific Reports* **3**, 1778 (2013).

[53] A. Aragoneses, S. Perrone, T. Sorrentino, M. C. Torrent, and C. Masoller, "Unveiling the complex organization of recurrent patterns in spiking dynamical systems", *Scientific Reports* **4**, 4696 (2014).

[54] J. P. Toomey and D. M. Kane, "Mapping the dynamic complexity of a semiconductor laser with optical feedback using permutation entropy", *Optics Express* **22**, 1713 (2014).

[55] N. Li, W. Pan, A. Locquet, V. N. Chizhevsky, and D. S. Citrin, "Statistical Properties of an External-Cavity Semiconductor Laser: Experiment and Theory", *IEEE Journal of Selected Topics in Quantum Electronics* **21**, 553 (2015).

[56] N. Oliver, T. Jüngling, and I. Fischer, "Consistency Properties of a Chaotic Semiconductor Laser Driven by Optical Feedback", **114**, 123902 (2015).

[57] D. Choi, M. J. Wishon, J. Barnoud, C. Y. Chang, Y. Bouazizi, A. Locquet, and D. S. Citrin, "Low-frequency fluctuations in an external-cavity laser leading to extreme events", *Physical Review E* **93**, 042216 (2016).

[58] L. Jumpertz, K. Schires, M. Carras, M. Sciamanna, and F. Grillot, "Chaotic light at mid-infrared wavelength", *Light: Science & Applications* **5**, e16088 (2016).

[59] A. Uchida, K. Amano, M. Inoue, K. Hirano, S. Naito, H. Someya, sao OowadaI, et al., "Fast physical random bit generation with chaotic semiconductor lasers", *Nature Photonics* **2**, 728 (2008).

[60] I. Kanter, Y. Aviad, I. Reidler, E. Cohen, and M. Rosenbluh, "An optical ultrafast random bit generator", *Nature Photonics* **4**, 58 (2010).

[61] H. G. Schuster and K. Lüdge. *Nonlinear laser dynamics: from quantum dots to cryptography*. John Wiley & Sons, 2012.

[62] S. Donati, "Developing self-mixing interferometry for instrumentation and measurements", *Laser & Photonics Reviews* **6**, 393 (2012).

[63] D. Brunner, M. C. Soriano, C. R. Mirasso, and I. Fischer, "Parallel photonic information processing at gigabyte per second data rates using transient states", *Nature Communications* **4**, 1364 (2013).

[64] M. Sciamanna and K. A. Shore, "Physics and applications of laser diode chaos", *Nature Photonics* **9**, 151 (2015).

[65] R. M. Nguimdo, G. Verschaffelt, J. Danckaert, and G. V. der Sande, "Reducing the phase sensitivity of laser-based optical reservoir computing systems", *Optics Express* **24**, 1238 (2016).

[66] J. Nakayama, K. Kanno, and A. Uchida, "Laser dynamical reservoir computing with consistency: an approach of a chaos mask signal", *Optics Express* **24**, 8679 (2016).

[67] J. Perchoux, A. Quotb, R. Atashkhooei, F. J. Azcona, E. E. Ramírez-Miquet, O. Bernal, A. Jha, et al., "Current Developments on Optical Feedback Interferometry as an All-Optical Sensor for Biomedical Applications", *Sensors* **16**, 694 (2016).

[68] R. Tkach and A. Chraplyvy, "Regimes of feedback effects in 1.5 μm distributed feedback lasers", *Journal of Lightwave Technology* **4**, 1655 (1986).

[69] P. Besnard, B. Meziane, and G. M. Stephan, "Feedback phenomena in a semiconductor laser induced by distant reflectors", *IEEE Journal of Quantum Electronics* **29**, 1271 (1993).

[70] T. Heil, I. Fischer, and W. Elsäßer, "Coexistence of low-frequency fluctuations and stable emission on a single high-gain mode in semiconductor lasers with external optical feedback", *Physical Review A* **58**, R2672 (1998).

[71] I. Fischer, G. H. M. Van Tartwijk, A. M. Levine, W. Elsäßer, E. Göbel, and D. Lenstra, "Fast Pulsing and Chaotic Itinerancy with a Drift in the Coherence Collapse of Semiconductor Lasers", *Physical Review Letters* **76**, 220 (1996).

[72] B. Tromborg, J. Osmundsen, and H. Olesen, "Stability analysis for a semiconductor laser in an external cavity", *IEEE. Journal of Quantum Electronics* **20**, 1023 (1984).

[73] J. Mørk, J. Mark, and B. Tromborg, "Route to chaos and competition between relaxation oscillations for a semiconductor laser with optical feedback", *Physical Review Letters* **65**, 1999 (1990).

[74] C. Risch and C. Voumard, "Self-pulsation in the output intensity and spectrum of GaAs-AlGaAs cw diode lasers coupled to a frequency-selective external optical cavity", *Journal of Applied Physics* **48**, 2083 (1977).

[75] J. Mørk, B. Tromborg, and P. L. Christiansen, "Bistability and low-frequency fluctuations in semiconductor lasers with optical feedback: a theoretical analysis", *IEEE Journal of Quantum Electronics* **24**, 123 (1988).

[76] J. Sacher, D. Baums, P. Panknin, W. Elsäßer, and E. O. Göbel, "Intensity instabilities of semiconductor lasers under current modulation, external light injection, and delayed feedback", *Physical Review A* **45**, 1893 (1992).

[77] M. C. Eguia, G. B. Mindlin, and M. Giudici, "Low-frequency fluctuations in semiconductor lasers with optical feedback are induced with noise", *Physical Review E* **58**, 2636 (1998).

[78] J. Mulet and C. R. Mirasso, "Numerical statistics of power dropouts based on the Lang-Kobayashi model", *Physical Review E* **59**, 5400 (1999).

[79] M. C. Eguia and G. B. Mindlin, "Semiconductor laser with optical feedback: From excitable to deterministic low-frequency fluctuations", *Physical Review E* **60**, 1551 (1999).

[80] B. Lindner, J. García-Ojalvo, A. Neiman, and L. Schimansky-Geier, "Effects of noise in excitable systems", *Physics Reports* **392**, 321 (2004).

[81] E. M. Izhikevich. *Dynamical systems in neuroscience*. MIT press, 2007.

[82] M. T. Hill, E. E. E. Frietman, H. de Waardt, G.-d. Khoe, and H. J. S. Dorren, "All fiber-optic neural network using coupled SOA based ring lasers", *IEEE Transactions on Neural Networks* **13**, 1504 (2002).

[83] A. R. S. Romariz and K. H. Wagner, "Tunable vertical-cavity surface-emitting laser with feedback to implement a pulsed neural model. 2. High-frequency effects and optical coupling", *Applied Optics* **46**, 4746 (2007).

[84] A. R. S. Romariz and K. H. Wagner, "Tunable vertical-cavity surface-emitting laser with feedback to implement a pulsed neural model. 1. Principles and experimental demonstration", *Applied Optics* **46**, 4736 (2007).

[85] A. Hurtado, I. D. Henning, and M. J. Adams, "Optical neuron using polarisation switching in a 1550nm-VCSEL", *Optics Express* **18**, 25170 (2010).

[86] W. Coomans, L. Gelens, S. Beri, J. Danckaert, and G. V. der Sande, "Solitary and coupled semiconductor ring lasers as optical spiking neurons", *Physical Review E* **84**, 036209 (2011).

[87] S. Barbay, R. Kuszelewicz, and A. M. Yacomotti, "Excitability in a semiconductor laser with saturable absorber", *Optics Letters* **36**, 4476 (2011).

[88] A. Hurtado, K. Schires, I. D. Henning, and M. J. Adams, "Investigation of vertical cavity surface emitting laser dynamics for neuromorphic photonic systems", *Applied Physics Letters* **100**, 103703 (2012).

[89] M. Turconi, B. Garbin, M. Feyereisen, M. Giudici, and S. Barland, "Control of excitable pulses in an injection-locked semiconductor laser", *Physical Review E* **88**, 022923 (2013).

[90] M. A. Nahmias, B. J. Shastri, A. N. Tait, and P. R. Prucnal, "A Leaky Integrate-and-Fire Laser Neuron for Ultrafast Cognitive Computing", *IEEE Journal of Selected Topics in Quantum Electronics* **19**, 1 (2013).

[91] F. Selmi, R. Braive, G. Beaudoin, I. Sagnes, R. Kuszelewicz, and S. Barbay, "Relative Refractory Period in an Excitable Semiconductor Laser", *Physical Review Letters* **112**, 183902 (2014).

[92] B. J. Shastri, M. A. Nahmias, A. N. Tait, B. Wu, and P. R. Prucnal, "SIMPEL: Circuit model for photonic spike processing laser neurons", *Optics Express* **23**, 8029 (2015).

[93] B. J. Shastri, M. A. Nahmias, A. N. Tait, A. W. Rodriguez, B. Wu, and P. R. Prucnal, "Spike processing with a graphene excitable laser", *Scientific Reports* **6**, 19126 (2016).

[94] D. Baums, W. Elsässer, and E. O. Göbel, "Farey tree and devil's staircase of a modulated external-cavity semiconductor laser", *Physical Review Letters* **63**, 155 (1989).

[95] J. M. Mendez, R. Laje, M. Giudici, J. Aliaga, and G. B. Mindlin, "Dynamics of periodically forced semiconductor laser with optical feedback", *Physical Review E* **63**, 066218 (2001).

[96] J. P. Toomey, D. M. Kane, M. W. Lee, and K. A. Shore, "Nonlinear dynamics of semiconductor lasers with feedback and modulation", *Optics Express* **18**, 16955 (2010).

[97] P. R. Prucnal, B. J. Shastri, T. F. de Lima, M. A. Nahmias, and A. N. Tait, "Recent progress in semiconductor excitable lasers for photonic spike processing", *Advances in Optics and Photonics* **8**, 228 (2016).

[98] Y. Liu, N. Kikuchi, and J. Ohtsubo, "Controlling dynamical behavior of a semiconductor laser with external optical feedback", *Physical Review E* **51**, R2697 (1995).

[99] A. Aragoneses, T. Sorrentino, S. Perrone, D. J. Gauthier, M. C. Torrent, and C. Masoller, "Experimental and numerical study of the symbolic dynamics of a modulated external-cavity semiconductor laser", *Optics Express* **22**, 4705 (2014).

[100] H. Poincaré and R. Magini, "Les méthodes nouvelles de la mécanique céleste", *Il Nuovo Cimento (1895-1900)* **10**, 128 (1899).

[101] E. N. Lorenz, "Deterministic Nonperiodic Flow", *Journal of the Atmospheric Sciences* **20**, 130 (1963).

[102] R. M. May, "Simple mathematical models with very complicated dynamics", *Nature* **261**, 459 (1976).

[103] O. Rössler, "An equation for continuous chaos", *Physics Letters A* **57**, 397 (1976).

[104] M. Cencini, M. Falcioni, E. Olbrich, H. Kantz, and A. Vulpiani, "Chaos or noise: Difficulties of a distinction", *Physical Review E* **62**, 427 (2000).

[105] J. M. Amigó, L. Kocarev, and J. Szczepanski, "Order patterns and chaos", *Physics Letters A* **355**, 27 (2006).

[106] O. A. Rosso, H. A. Larrondo, M. T. Martin, A. Plastino, and M. A. Fuentes, "Distinguishing Noise from Chaos", *Physical Review Letters* **99**, 154102 (2007).

[107] J. M. Amigó, S. Zambrano, and M. A. F. Sanjuán, "Combinatorial detection of determinism in noisy time series", *Europhysics Letters* **83**, 60005 (2008).

[108] M. Zanin, L. Zunino, O. A. Rosso, and D. Papo, "Permutation Entropy and Its Main Biomedical and Econophysics Applications: A Review", *Entropy* **14**, 1553 (2012).

[109] L. Zunino, M. C. Soriano, and O. A. Rosso, "Distinguishing chaotic and stochastic dynamics from time series by using a multiscale symbolic approach", *Physical Review E* **86**, 046210 (2012).

[110] C. S. Daw, C. E. A. Finney, and E. R. Tracy, "A review of symbolic analysis of experimental data", *Review of Scientific Instruments* **74**, 915 (2003).

[111] P. Shields and D. Neuhoff, "Block and sliding-block source coding", *IEEE Transactions on Information Theory* **23**, 211 (1977).

[112] C. Bandt and B. Pompe, "Permutation Entropy: A Natural Complexity Measure for Time Series", *Physical Review Letters* **88**, 174102 (2002).

[113] J. M. Amigó. *Permutation complexity in dynamical systems: ordinal patterns, permutation entropy and all that*. Springer Science & Business Media, 2010.

[114] U. Parlitz, S. Berg, S. Luther, A. Schirdewan, J. Kurths, and N. Wessel, "Classifying cardiac biosignals using ordinal pattern statistics and symbolic dynamics", *Computers in Biology and Medicine* **42**, 319 (2012).

[115] J. M. Amigó, S. Zambrano, and M. A. F. Sanjuán, "True and false forbidden patterns in deterministic and random dynamics", *Europhysics Letters* **79**, 50001 (2007).

[116] L. Zunino, M. Zanin, B. M. Tabak, D. G. Pérez, and O. A. Rosso, "Forbidden patterns, permutation entropy and stock market inefficiency", *Physica A* **388**, 2854 (2009).

[117] J. M. Amigó, R. Monetti, T. Aschenbrenner, and W. Bunk, "Transcripts: An algebraic approach to coupled time series", *Chaos* **22**, 013105 (2012).

[118] C. E. Shannon, "A mathematical theory of communication", *The Bell System Technical Journal* **27**, 379 (1948).

[119] C. Beck and F. Schögl. *Thermodynamics of chaotic systems: an introduction*. 4. Cambridge University Press, 1995.

[120] G. Boffetta, M. Cencini, M. Falcioni, and A. Vulpiani, "Predictability: a way to characterize complexity", *Physics Reports* **356**, 367 (2002).

[121] C. Tsallis, "Possible generalization of Boltzmann-Gibbs statistics", *Journal of Statistical Physics* **52**, 479 (1988).

[122] C. Bandt, G. Keller, and B. Pompe, "Entropy of interval maps via permutations", *Nonlinearity* **15**, 1595 (2002).

[123] J. M. Amigó, M. B. Kennel, and L. Kocarev, "The permutation entropy rate equals the metric entropy rate for ergodic information sources and ergodic dynamical systems", *Physica D* **210**, 77 (2005).

[124] J. M. Amigó, "The equality of Kolmogorov–Sinai entropy and metric permutation entropy generalized", *Physica D* **241**, 789 (2012).

[125] Y. Cao, W.-w. Tung, J. B. Gao, V. A. Protopopescu, and L. M. Hively, "Detecting dynamical changes in time series using the permutation entropy", *Physical Review E* **70**, 046217 (2004).

[126] J. M. Amigó, K. Keller, and J. Kurths, "Recent Progress in Symbolic Dynamics and Permutation Complexity Ten Years of Permutation Entropy", *European Physical Journal Special Topics* **222**, 241 (2013).

[127] O. A. Rosso and C. Masoller, "Detecting and quantifying stochastic and coherence resonances via information-theory complexity measurements", *Physical Review E* **79**, 040106 (2009).

[128] Y. Hong, "Experimental study of time-delay signature of chaos in mutually coupled vertical-cavity surface-emitting lasers subject to polarization optical injection", *Optics Express* **21**, 17894 (2013).

[129] A. Groth, "Visualization of coupling in time series by order recurrence plots", *Physical Review E* **72**, 046220 (2005).

[130] A. Bahraminasab, F. Ghasemi, A. Stefanovska, P. V. E. McClintock, and H. Kantz, "Direction of coupling from phases of interacting oscillators: a permutation information approach", *Physical Review Letters* **100**, 084101 (2008).

[131] M. Matilla-García and M. R. Marín, "A non-parametric independence test using permutation entropy", *Journal of Econometrics* **144**, 139 (2008).

[132] P. M. Saco, L. C. Carpi, A. Figliola, E. Serrano, and O. A. Rosso, "Entropy analysis of the dynamics of El Niño/Southern Oscillation during the Holocene", *Physica A* **389**, 5022 (2010).

[133] J. S. Cánovas, A. Guillamón, and M. del Carmen Ruíz, "Using permutations to detect dependence between time series", *Physica D* **240**, 1199 (2011).

[134] M. Matilla-García and M. R. Marín, "Spatial Symbolic Entropy: A Tool for Detecting the Order of Contiguity", *Geographical Analysis* **43**, 228 (2011).

[135] M. Barreiro, A. C. Marti, and C. Masoller, "Inferring long memory processes in the climate network via ordinal pattern analysis", *Chaos* **21**, 013101 (2011).

[136] I. Veisi, N. Pariz, and A. Karimpour, "Fast and Robust Detection of Epilepsy in Noisy EEG Signals Using Permutation Entropy", *IEEE 7th International Symposium on BioInformatics and BioEngineering*, 200 (2007).

[137] X. Li, G. Ouyang, and D. A. Richards, "Predictability analysis of absence seizures with permutation entropy", *Epilepsy Research* **77**, 70 (2007).

[138] A. A. Bruzzo, B. Gesierich, M. Santi, C. A. Tassinari, N. Birbaumer, and G. Rubboli, "Permutation entropy to detect vigilance changes and preictal states from scalp EEG in epileptic patients. A preliminary study", *Neurological Sciences* **29**, 3 (2008).

[139] N. Nicolaou and J. Georgiou, "Detection of epileptic electroencephalogram based on Permutation Entropy and Support Vector Machines", *Expert Systems with Applications* **39**, 202 (2012).

[140] B. Frank, B. Pompe, U. Schneider, and D. Hoyer, "Permutation entropy improves fetal behavioural state classification based on heart rate analysis from biomagnetic recordings in near term fetuses", *Medical and Biological Engineering and Computing* **44**, 179 (2006).

[141] S. Berg, S. Luther, S. E. Lehnart, K. Hellenkamp, R. Bauernschmitt, J. Kurths, N. Wessel, and U. Parlitz, "Comparison of features characterizing beat-to-beat time series", *International Biosignal Processing Conference* **49**, 1 (2010).

[142] T. Sorrentino, C. Quintero-Quiroz, M. C. Torrent, and C. Masoller, "Analysis of the Spike Rate and Spike Correlations in Modulated Semiconductor Lasers With Optical Feedback", *IEEE Journal of Selected Topics in Quantum Electronics* **21**, 561 (2015).

[143] T. Sorrentino, C. Quintero-Quiroz, A. Aragoneses, M. C. Torrent, and C. Masoller, "Effects of periodic forcing on the temporally correlated spikes of a semiconductor laser with feedback", *Optics Express* **23**, 5571 (2015).

[144] C. Quintero-Quiroz, J. Tiana-Alsina, J. Romá, M. C. Torrent, and C. Masoller. *Supplementary information*. Scientific Reports. 2016. URL: http://www.nature.com/article-assets/npg/srep/2016/161118/srep37510/extref/srep37510-s2.avi.

[145] R. L. Davidchack, Y.-C. Lai, A. Gavrielides, and V. Kovanis, "Dynamical origin of low frequency fluctuations in external cavity semiconductor lasers", *Physics Letters A* **267**, 350 (2000).

[146] R. L. Davidchack, Y.-C. Lai, A. Gavrielides, and V. Kovanis, "Chaotic transitions and low-frequency fluctuations in semiconductor lasers with optical feedback", *Physica D* **145**, 130 (2000).

[147] C. Quintero-Quiroz, J. Tiana-Alsina, J. Romà, M. C. Torrent, and C. Masoller, "Quantitative identification of dynamical transitions in a semiconductor laser with optical feedback", *Scientific Reports* **6**, 37510 (2016).

[148] G. Huyet, J. K. White, A. J. Kent, S. P. Hegarty, J. V. Moloney, and J. G. McInerney, "Dynamics of a semiconductor laser with optical feedback", *Physical Review A* **60**, 1534 (1999).

[149] N. Li, B. Kim, A. Locquet, D. Choi, W. Pan, and D. S. Citrin, "Statistics of the optical intensity of a chaotic external-cavity DFB laser", *Optics Letters* **39**, 5949 (2014).

[150] C. Quintero-Quiroz, S. Pigolotti, M. C. Torrent, and C. Masoller, "Numerical and experimental study of the effects of noise on the permutation entropy", *New Journal of Physics* **17**, 093002 (2015).

[151] L. D. Micco, J. G. Fernández, H. A. Larrondo, A. Plastino, and O. A. Rosso, "Sampling period, statistical complexity, and chaotic attractors", *Physica A* **391**, 2564 (2012).

[152] A. Kolmogorov, "On the Shannon theory of information transmission in the case of continuous signals", *IRE Transactions on Information Theory* **2**, 102 (1956).

Publications

- T. Sorrentino, **C. Quintero-Quiroz**, M. C. Torrent, and C. Masoller, "Analysis of the Spike Rate and Spike Correlations in Modulated Semiconductor Lasers With Optical Feedback", *IEEE Journal of Selected Topics in Quantum Electronics* **21**, 561 (2015). doi: 10.1109/JSTQE.2015.2436695

- T. Sorrentino, **C. Quintero-Quiroz**, A. Aragoneses, M. C. Torrent, and C. Masoller, "Effects of periodic forcing on the temporally correlated spikes of a semiconductor laser with feedback", *Optics Express* **23**, 5571 (2015). doi: 10.1364/OE.23.005571

- **C. Quintero-Quiroz**, S. Pigolotti, M. C. Torrent, and C. Masoller, "Numerical and experimental study of the effects of noise on the permutation entropy", *New Journal of Physics* **17**, 093002 (2015). doi: 10.1088/1367-2630/17/9/093002

- A. Aragoneses, T. Sorrentino, **C. A. Quintero**, S. Perrone, M. C. Torrent, and C. Masoller, "Effects of modulation in the complex dynamics of a semiconductor laser with feedback", *SPIE Proceedings* **9892**, 98920E (2016). doi: 10.1117/12.2228728

- **C. Quintero-Quiroz**, T. Sorrentino, M. C. Torrent, and C. Masoller, "Analysis of the effects of periodic forcing in the spike rate and spike correlation's in semiconductor lasers with optical feedback", *SPIE Proceedings* **9892**, 98921T (2016). doi: 10.1117/12.2227627

- **C. Quintero-Quiroz**, J. Tiana-Alsina, J. Romà, M. C. Torrent, and C. Masoller, "Quantitative identification of dynamical transitions in a semiconductor laser with optical feedback", *Scientific Reports* **6**, 37510 (2016). doi: 10.1038/srep37510

Additional work not related to the thesis:

- **C. Quintero-Quiroz** and M. Cosenza, "Collective behavior of chaotic oscillators with environmental coupling", *Chaos, Solitons & Fractals* **71**, 41 (2015). doi: 10.1016/j.chaos.2014.12.001

Conferences and Workshops

- NETT Workshop: Dynamics of Neural Circuits. Institute for Complex Systems, CNR, Florence, Italy. 17 to 20 of March 2014.
- NETT Mid-Term Review Meeting, Nijmegen, Netherlands. 9-11 June 2014.
- III Jornades de Complexitat, Barcelona, Spain. 19th of June 2014. **Poster Contribution**: Simbolyc dynamics of directly modulated semiconductor lasers with optical feedback.
- XXXIV Dynamics Days Europe 2014, University of Bayreuth, Germany. 8-12 September 2014. **Poster Contribution**: Experimental control of laser optical spikes via direct current modulation.
- IV Jornada complexitat, Campus Universitat Rovira i Virgili, Tarragona, Spain. May 25, 2015. **Poster Contribution**: Experimental control of laser optical spikes via direct current modulation.
- NETT Workshop: Neural Engineering in Medicine and Related Fields, INRIA Nancy, France. 2nd and 3rd of July 2015. **Poster Contribution**: Analysis of spike correlations in periodically forced semiconductor lasers with optical feedback.
- XXXV Dynamics Days Europe 2015, University of Exeter, UK. 6 -10 September 2015. **Oral Contribution**: Numerical and experimental study of the effects of noise on the permutation entropy. **Poster Contribution**: Analysis of spike correlations in periodically forced semiconductor lasers with optical feedback.
- NETT International Conference: System Level Approaches to Neural Engineering, PRBB Parc De Recerca Biomedical, Barcelona, (Spain). 21st to the 23rd of September 2015. **Poster Contribution**: Analysis of spike correlations in periodically forced semiconductor lasers with optical feedback.
- European Semiconductor Laser Workshop 2015, Universidad Carlos III, Madrid, Spain. 24th to 25th of September 2015. **Poster Contribution**: Analysis of spike correlations in periodically forced semiconductor lasers with optical feedback.
- XX Congreso de Física Estadística, Universidad de Extremadura, Badajoz, Spain. 5 - 7 de October 2015. **Poster Contribution**: Analysis of spike correlations in periodically forced semiconductor lasers with optical feedback.
- Jornada d'Investigadors Predoctorals Interdisciplinária (JIPI), Universitat de Barcelona, Spain. 2 of february of 2016. **Poster Contribution**: Analysis of spike correlations in periodically forced semiconductor lasers with optical feedback.

- SPIE Photonics Europe, SQUARE Brussels Meeting Centre, Brussels, Belgium. 3 - 7 April 2016. **Poster Contribution**: Analysis of spike correlations in periodically forced semiconductor lasers with optical feedback.

- V Jornada Complexitat, Institut Nacional d'Educació Física de Catalunya, UB Carrer l'Estadi, Barcelona, Spain. May 19, 2016. **Poster Contribution**: Analysis of spike correlations in periodically forced semiconductor lasers with optical feedback.

- International Tandem Workshop: Pattern Dynamics in Nonlinear Optical Cavities, Max Planck Institute for the physics of complex systems, Dresden, Germany. 15 to 19 of August 2016. **Oral Contribution**: Characterizing how complex optical signals emerge from noisy intensity fluctuations. **Poster Contribution**: Analysis of spike correlations in periodically forced semiconductor lasers with optical feedback.

- 25th International Conference on Artificial Neural Networks: A conference of the European Neural Network Society. Barcelona, Spainn. 6-9 September 2016. **Poster Contribution**: Analysis of spike correlations in periodically forced semiconductor lasers with optical feedback.

- IBERSINC, Tarragona, Spain 6 to 8 of October 2016. **Oral Contribution**: Characterizing how complex optical signals emerge from noisy intensity fluctuations. **Poster Contribution**: Analysis of spike correlations in periodically forced semiconductor lasers with optical feedback.

Schools and Research Stays

- School of Nonlinear Optics and Nanophotonics. IFT-UNESP, São Paulo, Brazil. November 25-December 6, 2013.
- Research Stay of two months in the Institute for Complex Systems, CNR. Florence, Italy. March-April 2015.
- Research Stay of three weeks in BitBrain, Zaragoza, Spain. July 2016.
- OSA Foundation: Siegman International School on Lasers. ICFO, Castelldefels, Spain. 24 to 29 of July 2016, **Poster Contribution**: Analysis of spike correlations in periodically forced semiconductor lasers with optical feedback.